Recent Changes in the ISBA-CTRIP Land Surface System for Use in the CNRM-CM6 Climate Model and in Global Off-Line Hydrological Applications

Bertrand Decharme, Christine Delire, Marie Minvielle, Jeanne Colin,
Jean-Pierre Vergnes, Antoinette Alias, David Saint-Martin, Roland Seferian,
Stephan Senesi, Aurore Voldoire

HAL Id: hal-02380963
https://hal.science/hal-02380963

Submitted on 4 Dec 2019

RESEARCH ARTICLE

Key Points:
- Land Surface Modeling for global climate and hydrological applications
- soil, snow, river, groundwater and floodwater processes

This article was corrected on 20 MAY 2019. See the end of the full text for details.

Recent Changes in the ISBA-CTRIP Land Surface System for Use in the CNRM-CM6 Climate Model and in Global Off-Line Hydrological Applications

Bertrand Decharme[1], Christine Delire[1], Marie Minvielle[1], Jeanne Colin[1], Jean-Pierre Vergnes[2], Antoinette Alias[1], David Saint-Martin[1], Roland Séférian[1], Stéphane Sénési[1], and Aurore Voldoire[1]

[1]CNRM UMR 3589, Météo-France/CNRS, Université fédérale de Toulouse, Toulouse, France, [2]BRGM French Geological Survey, Water Environment and Ecotechonologies Division, Orléans, France

Abstract In recent years, significant efforts have been made to upgrade physical processes in the ISBA-CTRIP land surface system for use in fully coupled climate studies using the new CNRM-CM6 climate model or in stand-alone mode for global hydrological applications. Here we provide a thorough description of the new and improved processes implemented between the CMIP5 and CMIP6 versions of the model and evaluate the hydrology and thermal behavior of the model at the global scale. The soil scheme explicitly solves the one-dimensional Fourier and Darcy laws throughout the soil, accounting for the dependency of hydraulic and thermal soil properties on soil organic carbon content. The snowpack is represented using a multilayer detailed internal-process snow scheme. A two-way dynamic flood scheme is added in which floodplains interact with the soil hydrology through reinfiltration of floodwater and with the overlying atmosphere through surface free-water evaporation. Finally, groundwater processes are represented via a two-dimensional diffusive unconfined aquifer scheme allowing upward capillarity rises into the superficial soil. This new system has been evaluated in off-line mode using two different atmospheric forcings and against a large set of satellite estimates and in situ observations. While this study is not without weaknesses, its results show a real advance in modeling the physical aspects of the land surface with the new ISBA-CTRIP version compared to the previous system. This increases our confidence that the model is able to represent the land surface physical processes accurately across the globe and in turn contribute to several important scientific and societal issues.

1. Introduction

In addition to global long-term observations, the study of the climate system requires global numerical models to analyze past, present, and future climate processes. Historically, these climate models are known as Ocean-Atmosphere-Global-Circulation Models, in which an atmospheric model is coupled to an oceanic model to analyze large-scale climatic equilibria. All too often, this terminology ignores both the Land Surface Models (LSMs) that provide realistic boundary conditions for the atmosphere in term of momentum, moisture, temperature, and energy (e.g., Pitman, 2003) and the River Routing Models (RRMs) that simulate river discharges into the ocean (Ducharne et al., 2003; Lohmann et al., 1998; Nijssen et al., 1997; Oki & Sud, 1998), allowing closure of the global water budget in climate models. Since the end of the last century, LSMs have evolved from the simple parameterizations included in atmospheric models (Manabe, 1969) to more realistic descriptions of the physical land surface processes linking the soil, snow, and vegetation (e.g., van den Hurk et al., 2011). Today, the study of these land surface processes plays an increasingly important role in the understanding of the climate system, its evolution, and its predictability. In addition, these physically based land surface systems are used in global hydrological applications in order to study the regional and global water cycle, predict streamflow, and inform water resource management.

The links between the climate and the land surface have been studied extensively, particularly through soil moisture (Douville, 2003; Douville et al., 2016; Koster et al., 2004, 2011; Seneviratne et al., 2010, 2013). Soil moisture mainly controls surface/atmosphere exchanges through its direct influence on surface temperature, soil evaporation, and plant transpiration. Its spatial redistribution, generally linked to topography (Beven & Kirkby, 1979), also controls the partitioning of precipitation between soil infiltration and runoff,

affecting in turn groundwater recharge, river discharge, and to a lesser extent river flooding. River stream-flow can affect the salinity and temperature of the ocean at the mouths of the largest rivers (Durand et al., 2011; Huang & Mehta, 2010; Jahfer et al., 2017; McGuire et al., 2016; Vinayachandran et al., 2015). Groundwater has a well-documented influence on the land water budget, especially on river discharges (Habets et al., 2008; Vergnes et al., 2012; Vergnes & Decharme, 2012). Through their slow response time, they sustain river base flow in humid climates during dry periods, while they receive river seepage in arid climates. Groundwater also acts as the lower boundary for the overlaying unsaturated soil and exchange water through downward percolation and upward capillarity rise (Maxwell et al., 2007, 2011; Miguez-Macho et al., 2007; Vergnes et al., 2014). Some observations also seem to indicate that the depth reached by plant roots is dependent on the water table depth (Fan, 2015), suggesting that groundwater may also affect rooting depth. These processes underline the influence of groundwater on the land surface evapotranspiration and possibly on climate, at least at a regional scale (Taylor et al., 2013; Wang et al., 2016). Finally, naturally inundated areas, such as inundated floodplains along rivers, have a strong influence on the annual cycle of river discharges, especially in tropical and high-latitude areas (Decharme et al., 2008, 2012; Yamazaki et al., 2011; Zhao et al., 2017). Flooded floodplains can affect the overlying atmosphere through their relatively high evapotranspiration, which enhances latent versus sensible heat exchange with the atmosphere (Krinner, 2003). Together with natural wetlands, they are one of the main contributors of natural methane emissions (Saunois et al., 2016), one of the major atmospheric greenhouse gases impacting climate evolution.

Feedbacks between the climate, hydrology, and snow cover are also crucial. From autumn to spring, the snow modifies the terrestrial albedo and surface roughness length, impacting the radiative and energy fluxes at the soil/atmosphere interface. The springtime snowmelt is the main contributor to the annual river discharges over all Arctic and many temperate basins. The snowpack also acts as an insulating layer at the surface, which prevents significant soil heat loss in winter. Through this process, the snow controls the temperature of the permafrost (soil that remains below 0 °C for two or more consecutive years) in boreal regions. The seasonal melt of the permafrost active layer controls land surface CO_2 and CH_4 emissions into the atmosphere (e.g., Schuur et al., 2015), as a large part of the terrestrial carbon stock is localized in permafrost regions. In light of this fact, the polar warming amplification (Holland & Bitz, 2003), together with the drastic decrease in springtime snow cover in Arctic regions over recent decades (Derksen & Brown, 2012), which is expected to continue (Brutel-Vuilmet et al., 2013), are good examples of interactions between snow processes and the climate.

To contribute to the Fifth Assessment Report (AR5) of the United Nations Intergovernmental Panel on Climate Change (IPCC), the Centre National de Recherches Météorologiques (CNRM; https://www.umr-cnrm.fr/) of Météo-France developed the CNRM-CM5 climate model (Voldoire et al., 2013; https://www.umr-cnrm.fr/spip.php?article126) in the 2000s. Its land surface component was composed of the Interaction Soil-Biosphere-Atmosphere (ISBA; https://www.umr-cnrm.fr/isbadoc/model.html) LSM developed at CNRM to calculate the time evolution of the energy and water budgets at the land surface (Noilhan & Planton, 1989), and the Total Runoff Integrating Pathways (TRIPs; http://hydro.iis.u-tokyo.ac.jp/~taikan/TRIPDATA/) RRM developed at the University of Tokyo (Oki & Sud, 1998) to simulate river discharges up to the ocean from the total runoff computed by ISBA. This ISBA-TRIP land surface system (Decharme & Douville, 2007) was embedded into the SURFEX numerical interface (Masson et al., 2013; available freely at https://www.umr-cnrm.fr/surfex/), designed first to facilitate its implementation in all atmospheric models of Météo-France and second to use the same code in off-line applications driven by atmospheric observations in order to avoid the systematic biases commonly found in atmospheric models. This off-line configuration was particularly relevant in addressing many large-scale hydrological studies over the last decade (Alkama et al., 2011; Casse et al., 2015; Cazenave et al., 2014; Decharme & Douville, 2006b; Douville et al., 2013; Emery et al., 2016; Llovel et al., 2011; Pedinotti et al., 2012; Szczypta et al., 2012). More recently, this land surface system has been largely upgraded to improve the representation of the land surface hydrologic and thermal processes for these large-scale hydrological applications, and also for use in the new CNRM-CM6 climate model and the new CNRM-ESM2 Earth system model (details available at http://www.umr-cnrm.fr/cmip6). These two climate models were developed at CNRM as a contribution to the IPCC Sixth Assessment Report (AR6) via participation in the sixth phase of the Coupled Model Intercomparison Project (CMIP6; Eyring et al., 2016).

The goal of this study is to present and thoroughly evaluate the main developments in the land surface physical processes made at CNRM between phases 5 and 6 of the IPCC Assessment Report. This more ambitious land surface system is composed of a new version of the ISBA LSM coupled to a new version of the TRIP RRM, entirely redeveloped at CNRM and renamed CTRIP (meaning *CNRM version of TRIP*). In this study, the new version of ISBA will be referred to as $ISBA_{DF}$ because it solves directly diffusive equations in both the soil and snow, while the old version, which used the *force-restore* method (Deardorff, 1977, 1978) to compute soil temperature and hydrology, will be referred to as $ISBA_{FR}$. The new $ISBA_{DF}$-CTRIP land surface system is then evaluated in off-line mode at the global scale over the 1979 to 2010 period against a wide range of long-term reanalyses, satellite estimates, and in situ observations. Both the old $ISBA_{FR}$-TRIP and the new $ISBA_{DF}$-CTRIP land surface systems are reviewed in section 2. The experimental design is given in section 3. Section 4 presents the evaluation of the simulated Northern Hemisphere snow and permafrost, while the global water budget is evaluated in section 5. A brief discussion and the main conclusions are given in section 6.

2. Review of Land Surface Systems

2.1. Brief Review of the Old $ISBA_{FR}$-TRIP Version

In the previous $ISBA_{FR}$-TRIP land surface system (Figure 1a) set up 10 years ago by Decharme and Douville (2007), $ISBA_{FR}$ was a relatively simple bucket-type soil scheme based on the force-restore method (Deardorff, 1977, 1978), which calculated the time evolution of the water and energy budgets at the land surface (Appendix A). The land surface energy budget was computed via a single soil-vegetation-snow composite approach (Noilhan & Planton, 1989). Soil temperatures were solved using four force-restore pseudo-layers, instead of the original two layers, in order to increase the soil thermal inertia for long-term climatic applications.

The land surface water budget included a one-layer vegetation rainfall interception scheme (Mahfouf et al., 1995) in which the canopy evaporates at a potential rate over the wet fraction of the foliage defined by Deardorff (1978); a simple Jarvis-type scheme for the plant transpiration (Jarvis, 1976) function of the leaf area index, root zone water stress, and meteorological constraints (solar radiation, air temperature, and saturation deficit); a simple one-layer snow scheme (Douville et al., 1995) in which the snow albedo decreases exponentially or linearly with time depending on whether the snow is melting or not; a two-layer soil freezing scheme (Boone et al., 2000) in which only the top soil can freeze; a three-layer force-restore soil moisture scheme (Boone et al., 1999) in which the subsurface runoff is computed as a linear gravitational drainage term when the deep soil moisture exceeds the water content at field capacity, corresponding to a hydraulic conductivity of 0.1 mm/day (Mahfouf & Noilhan, 1996); and an exponential profile of the saturated hydraulic conductivity with soil depth to empirically mimic larger water movements in the root zone due to soil organic matter and root-induced macroporosity compared to the more compacted deep soil that, inversely, limits downward moisture flow (Decharme et al., 2006).

This $ISBA_{FR}$ version also included a comprehensive subgrid hydrology to account for the heterogeneity of precipitation, topography, maximum soil infiltration capacity, and vegetation in each grid cell (Decharme & Douville, 2006a). The dripping from the canopy was computed via an exponential distribution of precipitation intensities over the fraction of the grid cell affected by rainfall. Spatial heterogeneities in rainfall intensity were also combined with a subgrid exponential distribution of soil maximum infiltration capacity to compute soil infiltration excess runoff (Horton mechanism) considering unfrozen and frozen empirical soil fractions. A simple subgrid topography-based TOPMODEL approach (Beven & Kirkby, 1979; Decharme et al., 2006) was used to simulate surface runoff over a saturated fraction of the grid cell (Dunne's soil saturation mechanism). Lastly, a tile approach was used to represent land cover and soil depth heterogeneities, and distinct energy and water budgets were computed for each tile. The relative grid cell fractional coverage of these tiles was used to determine the grid-box-averaged water and energy budgets.

Finally, the total runoff simulated by $ISBA_{FR}$ was converted into river discharges via TRIP using a global river channel network at 1° resolution, a simple linear stream river reservoir, and a constant streamflow velocity of 0.5 m/s. More details on this version can be found in Alkama et al. (2010), Decharme and Douville (2007), and Voldoire et al. (2013).
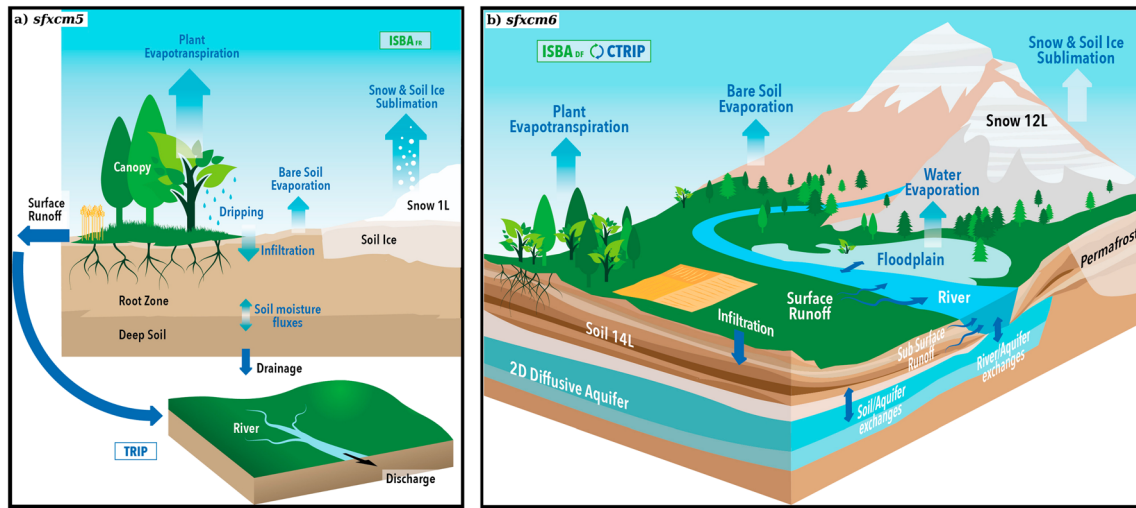
Figure 1. The old and new land surface systems embedded in the SURFEX modeling platform for global climate and hydrological applications. (a) Rejuvenation of the schematic view from Decharme (2007) of the old ISBA$_{FR}$-TRIP system (*sfxcm5*) used in CNRM-CM5. ISBA$_{FR}$ had one soil-vegetation-snow composite energy budget, one-layer simple snow scheme, one-layer rainfall vegetation interception scheme allowing canopy dripping and direct evaporation from wet leaves, Jarvis-type plant transpiration scheme, bare soil evaporation, soil ice and snow sublimation, three-layer soil hydrology (a surface layer included in the root zone, which is above a deep soil reservoir), two-layer superficial soil freezing scheme, a linear deep drainage flux, and a comprehensive set of subgrid hydrology to compute surface runoff. TRIP was used to simulate river discharges at 1° resolution using a simple linear stream river reservoir. (b) Schematic view of the new ISBA$_{DF}$-CTRIP two-way coupled system (*sfxcm6*) used in CNRM-CM6. This new system accounts for the same processes as previously but has two energy budgets (snow and snow-free part), 12-layer intermediate complexity snow scheme, CO_2 responsive based plant transpiration scheme, 14-layer explicit soil scheme where temperature, moisture, and soil ice are colocalized, subgrid lateral subsurface flows in the uppermost soil layers, floodplains dynamical scheme allowing direct evaporation, precipitation interception and soil reinfiltration, groundwater scheme using 2-D diffusive aquifers allowing exchanges with both the soil and the river, and variable streamflow velocity assuming a rectangular river cross-section over a channel network at 0.5° resolution.

2.2. The New ISBA$_{DF}$-CTRIP Version

The new ISBA$_{DF}$-CTRIP land surface system is more ambitious than the previous version (Figure 1b). ISBA$_{DF}$ explicitly solves the one-dimensional Fourier and Darcy laws throughout the soil (Boone et al., 2000; Decharme et al., 2011, 2013), accounting for the hydraulic and thermal properties of soil organic carbon (Decharme et al., 2016). The use of a multilayer snow model of intermediate complexity (Boone & Etchevers, 2001; Decharme et al., 2016) allows separate water and energy budgets to be simulated for the soil and the snowpack. A two-way coupling between ISBA$_{DF}$ and CTRIP is set up to account for, first, a dynamic river flooding scheme in which floodplains interact with the soil and the atmosphere through free-water evaporation, infiltration, and precipitation interception (Decharme et al., 2012) and second, a two-dimensional diffusive groundwater scheme to represent unconfined aquifers and upward capillarity fluxes into the superficial soil (Vergnes et al., 2012, 2014; Vergnes & Decharme, 2012).

2.2.1. Surface Energy Budget

The surface energy budget is computed using two independent energy budgets: one for the snowpack and one for a soil-vegetation-flood composite surface. The land surface temperature T_s (K) and the radiative properties at the surface-atmosphere interface, such as the skin temperature T_{skin} (K), albedo α_s, and emissivity ε_s, are a combination of both the snowpack and soil-vegetation-flood composite properties:

$$T_{skin} = \sqrt[4]{\frac{(1-p_{sn})\varepsilon_g T_{g_1}^4 + p_{sn}\varepsilon_{sn} T_{sn_1}^4}{(1-p_{sn})\varepsilon_g + p_{sn}\varepsilon_{sn}}} \tag{1a}$$

$$T_s = (1-p_{sn})T_{g_1} + p_{sn}T_{sn_1} \tag{1b}$$

$$\alpha_s = (1-p_{sn})\alpha_g + p_{sn}\alpha_{sn} \tag{1c}$$

$$\varepsilon_s = (1-p_{sn})\varepsilon_g + p_{sn}\varepsilon_{sn} \tag{1d}$$

where T_{g_1} (K) is the soil-vegetation-flood composite surface temperature; T_{sn_1} (K) is the snow surface temperature; α_g and ε_g are the soil-vegetation-flood composite albedo and emissivity; and p_{sn}, α_{sn}, and ε_{sn}

are the effective snow grid cell fraction, albedo, and emissivity. T_{g_1} evolves according to the snow-free net radiation using composite soil-vegetation-flood albedo and emissivity, snow-free turbulent heat fluxes, solar radiation not absorbed by the snowpack, the heat flux from the snow, the soil freezing/thawing, and the heat exchanged with the underlying soil layer (Appendix B). In the same way, the snow surface temperature evolves according to the solar and atmospheric radiation absorbed in the first thin snowpack layer, the snow sensible and latent heat fluxes, the heat diffusion with the underlying snow layer, and the energy due to phase change between water and ice (Boone & Etchevers, 2001).

2.2.2. Snowpack Processes

The snowpack is represented by a multilayer snow scheme of intermediate complexity developed by Boone and Etchevers (2001) and revised by Decharme et al. (2016). It uses 12 layers to represent snowpack processes. The snow mass reservoir is fed by snowfall and rainfall intercepted by snow and is emptied by snow sublimation, the snowmelt-runoff at the bottom of the pack, and a simple ice sheet runoff to avoid unrealistic snow accumulation over continental glaciers (Appendix C). This scheme simulates all the macroscopic physical properties of the snowpack in each layer, such as absorption of solar energy, heat content, compaction and density, snowmelt, water percolation, and water refreezing. The effective snow fraction of the grid cell, p_{sn}, is the average between the fractions of snow in the vegetated, p_{snv}, and nonvegetated, p_{sng}, parts of the grid cell:

$$p_{sn} = \left(1 - f_{veg}\right) p_{sn_g} + f_{veg} p_{sn_v} \tag{2a}$$

$$p_{sng} = \min\left(1, \frac{h_{sn}}{h_{sng}}\right) \tag{2b}$$

$$p_{snv} = \frac{h_{sn}}{h_{sn} + 2z_{0veg}} \tag{2c}$$

where f_{veg} represents the grid cell fraction of vegetation and z_{0veg} (m) is the vegetation roughness length, which varies according to each vegetation type (Table 1). h_{sng} (m) is a snow depth threshold set to 0.01 m and h_{sn} (m) the total snow depth.

The snow albedo and the absorption of incident shortwave solar radiation within the pack are solved over three spectral bands and account for snow age and the optical diameter of snow (computed via snow density). The first band [0.3–0.8] μm represents the ultraviolet and visible range, while the two other bands, [0.8–1.5] μm and [1.5–2.8] μm, represent two near-infrared ranges. The snow heat content allows the presence of dry and wet snow. The heat vertical diffusion is solved using the Fourier law, accounting for latent heat absorption or release due to phase changes. The snow compaction results from changes in snow viscosity and wind-induced densification of near-surface snow layers. Compaction stops when the snow density reaches its maximum value of 750 kg/m. When the temperature in a layer exceeds the freezing point (273.16 K), snowmelt occurs. The resulting liquid water flows down layer by layer using a series of bucket-type reservoirs. Local changes in liquid water content arise from snowmelt, water freezing, evaporation, and liquid flow. Finally, the snowmelt runoff rate is defined as the rate at which liquid water leaves the base of the snowpack.

2.2.3. Evapotranspiration

The total evapotranspiration is the sum of the direct evaporation of the water intercepted by the canopy, the evaporation or sublimation from the bare soil, the transpiration from plants, the sublimation from snow, and the direct evaporation of the water in the floodplains. As in ISBA$_{FR}$, the water intercepted by the canopy evaporates at a potential rate. Bare soil evaporation depends on surface soil moisture conditions (Mahfouf & Noilhan, 1991) and becomes potential when the superficial water content exceeds field capacity corresponding to a −0.33 bar soil matric potential.

The direct evaporation from floodwater depends on the flooded fraction of the grid cell, f_{flood}, provided to ISBA$_{DF}$ by the CTRIP river model. In addition, we impose a limit on the floodwater evaporation in the presence of dense high vegetation because forests are rarely completely submerged and water under a dense canopy does not evaporate at the potential rate. To limit the complexity of the numerical coupling between the two models, we also prevent direct evaporation from floodwater in the presence of snow, assuming that the floodwater is covered by snow. Evaporation is allowed to occur on an effective floodplain fraction, $p_{f_{eff}}$,

Table 1
The 12 sub-grid land tiles derived from the 1-km ECOCLIMAP-II database

Tiles	Land types	Δz_2	Δz_3	f_{veg}	n_i
1	Bare Soil & Desert	0.5–1.0	0.5	–	0.035
2	Rocks & Urban area	0.2	0.0	–	0.035
3	Permanent Snow & Ice	0.2	0.0	–	0.035
4	Temperate Broadleaf Deciduous Tropical Broadleaf Deciduous Temperate Broadleaf Evergreen Boreal Broadleaf Deciduous Shrub	1.5–4.0	0.0–2.0	0.95	0.075
5	Boreal Needleleaf Evergreen Temperate Needleleaf Evergreen Boreal Needleleaf Deciduous	1.5–3.0	0.5–1.0	0.95	0.100
6	Tropical Broadleaf Evergreen	3.0–8.0	0.0–1.0	1.0	0.100
7	C3 crops	1.0–1.5	0.5	*f(LAI)*	0.050
8	C4 crops	1.0–1.5	0.5	*f(LAI)*	0.050
9	Irrigated crops	1.5	0.5	*f(LAI)*	0.050
10	C3 Grassland Boreal Grassland (Tundra)	0.5–1.5	0.5	0.95	0.050
11	C4 grassland	0.5–1.5	0.5	0.95	0.075
12	Peat, bogs and Irrigated grass	1.0–3.0	0.0–0.5	0.95	0.075

Note. Some values or ranges are given for each tile: Δz_2 (m) the depth of the root, Δz_3 (m) the deep soil thickness under the roots for the *sfxcm5* version, f_{veg} the dimensionless grid cell vegetation fraction where $f(LAI) = 1 - e^{-0.6LAI}$, and the floodplain roughness coefficient, n_i.

computed as the average between the flooded snow-free unvegetated ground and the flooded snow-free vegetation (Decharme et al., 2012):

$$p_{f_{eff}} = \left(1 - f_{veg}\right)p_{f_g} + f_{veg}p_{f_v} \tag{3a}$$

$$p_{f_g} = \min\left[f_{flood}, 1 - p_{sn_g}\right] \tag{3b}$$

$$p_{f_v} = \min\left[f_{flood} \times \min\left(1, \frac{4}{LAI}\right), 1 - p_{sn_v}\right] \tag{3c}$$

where LAI (m/m) is the leaf area index, assuming that a LAI below 4 is representative of low vegetation (e.g., grassland, crops, and sparse forests) that does not limit floodwater evaporation. These fractions are also used to compute the soil-vegetation-flood composite surface temperature (Appendix B).

Unlike the simple Jarvis-type scheme used in ISBA$_{FR}$, plant transpiration in ISBA$_{DF}$ is now controlled by the stomatal conductance of leaves, which according to the Jacob (1994) formulation adapted to ISBA by Calvet et al. (1998) depends on carbon cycling in vegetation. Carbon assimilation and hence stomatal conductance and transpiration are limited when soil moisture content drops below field capacity but also when the atmospheric vapor pressure deficit exceeds a certain threshold (see Joetzjer et al., 2015, for details). Finally, the soil water used for transpiration is removed throughout the root zone according to a vertical root-density profile. This profile is the weighted linear combination of a power law profile inspired by Jackson et al. (1996) and a simple homogeneous profile (Canal et al., 2014; Garrigues et al., 2018). In tropical forests, the weight of the homogeneous part of the profile is set to 25% to ensure sufficient root density down to 3–4-m depth. For all other vegetation types, this weight is set to 5%.

2.2.4. Soil Temperature and Moisture

Soil temperature and moisture are calculated on the same vertical grid using 14 layers down to 12-m depth (Decharme et al., 2013). The depths of the 14 layers (0.01, 0.04, 0.1, 0.2, 0.4, 0.6, 0.8, 1.0, 1.5, 2.0, 3.0, 5.0, 8.0, and 12.0 m) have been chosen to minimize numerical errors in solving the finite-difference diffusion equations, especially in the first meter of the soil. The one-dimensional Fourier law is used to simulate temperature diffusion within the soil column as follows:

$$c_g(z)\frac{\partial T_g(z)}{\partial t} = \frac{\partial}{\partial z}\left[\lambda_g(z)\frac{\partial T_g(z)}{\partial z}\right] + \frac{L_f Q_{fz}(z)}{\Delta z} \tag{4}$$

where T_g (K) is the soil temperature, Δz (m) the thickness of each layer, $L_f (3.337 \times 10^5$ J/kg) the latent heat of fusion, Q_{fz} (kg $\cdot$ m$^{-2} \cdot$ s^{-1}) the soil water freezing/thawing fluxes in each layer, c_g (J $\cdot$ m$^{-3} \cdot$ K^{-1}) the soil heat capacity, and λ_g (W $\cdot$ m$^{-1} \cdot$ K^{-1}) the soil thermal conductivity.

The soil hydrology uses the mixed form of the Richards equation to describe the water-mass transfer within the soil via Darcy's law. The tendency in each soil layer is solved in terms of volumetric water content, w_g (m^3/m^3), and the hydraulic gradient in terms of water pressure head ψ (m), as follows:

$$\frac{\partial w_g(z)}{\partial t} = \frac{\partial}{\partial z}\left[(k(z)+\nu(z))\frac{\partial \psi(z)}{\partial z} + k(z)\right] + \frac{Q_{src}(z)-Q_{fz}(z)-Q_{sb}(z)}{\rho_w \Delta z} \tag{5}$$

where ρ_w (kg/m^3) is the density of liquid water, Q_{src} (kg $\cdot$ m$^{-2} \cdot$ s^{-1}) the soil-water source/sink term (infiltration minus soil evaporation and plant transpiration), Q_{sb} (kg $\cdot$ m$^{-2} \cdot$ s^{-1}) a lateral subsurface runoff computed using a subgrid topography based on TOPMODEL approach that occurs only in the uppermost soil layers (Decharme et al., 2013), k (m/s) the soil hydraulic conductivity, and ν (m/s) the isothermal vapor conductivity computed via a function of soil texture, water content, and temperature following Braud et al. (1993).

The relationship between soil moisture, soil matric potential, and hydraulic conductivity in each layer is determined using Brooks and Corey (1966) adjusted to account for soil ice according to Johnsson and Lundin (1991):

$$\psi = \psi_{sat}\left(\frac{w_g}{w_{sat}-w_{fz}}\right)^{-b} \tag{6a}$$

$$k = \xi_{fz} k_{sat}\left(\frac{w_g}{w_{sat}-w_{fz}}\right)^{2b+3} \tag{6b}$$

$$\xi_{fz} = 10^{-6w_{fz}/(w_g+w_{fz})} \tag{6c}$$

where w_{sat} (m^3/m^3) is the soil porosity, k_{sat} (m/s) the soil hydraulic conductivity at saturation, ψ_{sat} (m) the water pressure head at saturation, b the dimensionless shape parameter of the soil-water retention curve, w_{fz} (m^3/m^3) the soil ice volumetric water content, and ξ_{fz} a dimensionless impedance factor that acts to limit vertical soil water fluxes in the presence of soil ice.

The soil ice due to soil water phase changes is computed in each soil layer, accounting for the ice sublimation and vegetation insulation effect at the surface. The maximum temperature that allows freezing is related to the soil water pressure head according to the Clausius-Clapeyron relation for water phase equilibrium and using the Gibbs free energy method (Fuchs et al., 1978; Koren et al., 1999). This method allows us to determine the maximum liquid water that can freeze as a function of temperature. More details can be found in Boone et al. (2000) and Decharme et al. (2016).

The soil moisture profile is computed only over the rooting depth, from 0.2 to 8 m according to the vegetation type (Table 1), while the soil temperature is computed down to a depth of 12 m. Because the computation of soil thermal parameters requires the hydrologic characteristics of each soil layer, the soil moisture under the root zone is extrapolated at each deeper node, assuming a balance of gravity and capillary forces in Darcy's law (Decharme et al., 2013). In potential permafrost regions (see section 3.1), soil moisture is, however, computed down to 12-m depth like temperature to account for the strong effect of deep soil ice on soil thermal inertia.

2.2.5. Combination of Organic and Mineral Soil Hydraulic and Thermal Properties

Hydraulic and thermal properties of mineral and organic soils are very different (Boelter, 1969; Letts et al., 2000). Organic soils are generally relatively wet, with a shallow water table, due to a very high porosity, a weak hydraulic suction, and a sharp vertical hydraulic conductivity profile from high values at the surface to very low values at the subsurface. Their low thermal conductivity and relatively high heat capacity act as an insulator for soil temperature and prevent the soil from warming significantly during the summer. These thermal properties partly control the depth reached by the 0 °C isotherm, which defines the thickness of the active layer in summer over the permafrost area (Decharme et al., 2016; Lawrence & Slater,

2008; Paquin & Sushama, 2014). Consequently, following Lawrence and Slater (2008), the soil thermal and hydraulic properties described in section 2.2.4 (equations (4)–6) are computed in each layer as a weighted combination of standard mineral soil properties and pure Soil Organic Carbon (SOC) values using a SOC fraction.

This SOC fraction f_{soc} is determined using a soil carbon density profile ρ_{soc} (kg/m^3) over the entire soil grid empirically computed from the SOC content of two soil horizons (0–0.3 and 0.3 1 m) given by observations. As an example, the soil porosity in each layer is given by the following form

$$w_{sat} = (1-f_{soc})w_{sat,m} + f_{soc}w_{sat,peat} \tag{7a}$$

$$f_{soc} = \frac{\rho_{soc}}{(1-w_{sat,peat})\rho_{oc}} \tag{7b}$$

where ρ_{oc} (kg/m^3) is the pure organic carbon density equal to 1,300 kg/m^3 (Farouki, 1986), $w_{sat,m}$ (m^3/m^3) the porosity of the mineral soil, and $w_{sat,peat}$ the porosity of a typical peat soil profile calculated using Boelter (1969) and Letts et al. (2000) values of 0.930 for a fibric top soil to 0.845 for a sapric subsoil. More details and parameter values are given in Decharme et al. (2016).

The standard mineral soil hydraulic properties in each layer are related to soil textures (clay and sand) using the Noilhan and Lacarrere (1995) continuous relationships derived from the Clapp and Hornberger (1978) pedotransfer functions. Note that continuous relations from Cosby et al. (1984) can also be used as an option in ISBA$_{DF}$ (Decharme et al., 2011). The soil heat capacity in each layer is the weighted average of the heat capacities of the soil matrix, the water and the ice in which the standard mineral soil matrix heat capacity is taken from Farouki (1986) as the product between mineral soil density and specific heat capacity. The soil thermal conductivity is computed according to the Peters-Lidard et al. (1998) formulation, a complex combination of dry and saturated soil thermal conductivities, weighted by the Kersten number, which depends on the degree of saturation of the soil layer. In this formulation, standard mineral dry and solid thermal conductivities are related to mineral soil density, mineral soil porosity, quartz conductivity, and soil quartz content.

2.2.6. Subgrid Hydrology

In ISBA$_{FR}$, the good partitioning of precipitation between evapotranspiration and runoff was the result of subgrid processes related to heterogeneities in precipitation, soil infiltration capacity, topography, and vegetation (Decharme, 2007). With a few exceptions, the same set of subgrid parameterizations is used in ISBA$_{DF}$. The first modification is linked to the presence of floodplains that intercept precipitation and snowmelt on the flooded part of the grid cell as follows:

$$P_{fld} = f_{flood}(P_g + Q_{sm}) \tag{8}$$

where P_{fld} (kg $\cdot$ m^{-2} $\cdot$ s^{-1}) is the mass of water intercepted by the floodplains, P_g (kg $\cdot$ m^{-2} $\cdot$ s^{-1}) the sum of the rainfall not intercepted by the canopy and the dripping from the interception reservoir, and Q_{sm} (kg $\cdot$ m^{-2} $\cdot$ s^{-1}) the snowmelt. Second, because we assume that the flood occurs preferentially over the saturated fraction of the grid cell, f_{sat}, the Dunne surface runoff Q_D (kg $\cdot$ m^{-2} $\cdot$ s^{-1}) and total surface runoff Q_s (kg $\cdot$ m^{-2} $\cdot$ s^{-1}) are given by

$$Q_D = \max\left(0, f_{sat}-f_{flood}\right) \times (P_g + Q_{sm}) \tag{9a}$$

$$Q_s = Q_D + Q_H\left[1-\max\left(f_{sat}, f_{flood}\right)\right] \tag{9b}$$

where Q_H (kg $\cdot$ m^{-2} $\cdot$ s^{-1}) is the Horton surface runoff and f_{sat} is computed by adapting the previous TOPMODEL approach of ISBA$_{FR}$ to ISBA$_{DF}$ (Decharme et al., 2013). Third, due to the explicit simulation of the soil freezing/thawing with ISBA$_{DF}$, the Horton surface runoff is directly computed without the use of an empirical partitioning between frozen and unfrozen soil as follows:

$$Q_H = \frac{P_g}{1+\mu I_c/P_g} + \max(0, Q_{sm}-I_c) \tag{10}$$

where I_c (kg $\cdot$ m^{-2} $\cdot$ s^{-1}) is the soil maximum infiltration capacity function and μ the fraction of the grid-cell affected by rainfall. I_c is based on the Green and Ampt (1911) approach modified by Decharme and Douville (2006a) as follows:

$$I_c = \frac{\rho_w}{z_3} \sum_{i=1}^{3} \xi_{fz_i} k_{sat_i} \left[\frac{b_i \psi_{sat_i}}{\Delta z_i} \left(\frac{w_{g_i}}{w_{sat_i} - w_{fz_i}} - 1 \right) + 1 \right] \tag{11}$$

where z_3 is the depth of the third layer down to 0.1 m used to determine the maximum amount of water that infiltrates the soil.

Finally, as in ISBA$_{FR}$, the soil water infiltration is the difference between snowmelt plus throughfall rate and the surface runoff. However, ISBA$_{DF}$ also accounts for floodwater infiltration, I_{fld} (kg $\cdot$ m^{-2} $\cdot$ s^{-1}), which occurs if f_{flood} is superior to f_{sat} and depends on the maximum infiltration capacity of the soil. In other words, the floodwater cannot infiltrate the part of the grid cell where the soil is saturated. I_{fld} can thus be computed as follows from the potential mass of floodwater that could infiltrate the soil, M_{fld} (kg $\cdot$ m^{-2} $\cdot$ s^{-1}), provided by the CTRIP river model:

$$I_{fld} = \max\left(0, f_{flood} - f_{sat}\right) \times \min\left[I_c, \min\left(M_{fld}, \frac{\rho_w \Delta z_w}{\tau_{day}} \right) \right] \tag{12a}$$

$$M_{fld} = \frac{F_w}{A_{ctrip} \Delta t_{cpl}} \tag{12b}$$

where τ_{day} (s) is a time relaxation of 1 day, Δz_w (m) a water thickness of 1 m used to limit the flood water mass infiltration into the soil to 1,000 kg $\cdot$ m^{-2} $\cdot$ day^{-1} using a water density ρ_w of 1,000 kg/m^3, F_w (kg) the mass of water stored in the CTRIP floodplain reservoir, Δt_{cpl} (s) the coupling time step between ISBA$_{DF}$ and CTRIP, and A_{ctrip} (m^2) the area of a CTRIP grid cell.

2.2.7. Water Table Upward Capillary Fluxes

The water table depth provided to ISBA$_{DF}$ by the CTRIP river model acts as a lower boundary condition for the soil moisture column calculated in ISBA$_{DF}$. However, because upward capillary fluxes only take place over lowlands (flat valleys and alluvial plains), the water table depth computed by CTRIP cannot be considered uniform over the entire coarse grid cell of a climate model. In a region with steep topography, upward capillary fluxes from the aquifer occur only in the lowlands, generally near the river. A fraction allowing upward capillary fluxes that reflects the subgrid spatial variability of topography inside each CTRIP grid cell is also sent to ISBA$_{DF}$. The soil/groundwater exchange flux, Q_{sg} (kg $\cdot$ m^{-2} $\cdot$ s^{-1}), is computed using Darcy's law considering that the water pressure head of the water table is at saturation:

$$Q_{sg} = f_{wtd} \rho_w k_N \left(\frac{\psi_N - \psi_{sat}}{z_N - z_{wtd}} + 1 \right) + (1 - f_{wtd}) \rho_w k_N \tag{13}$$

where f_{wtd} is the fraction of the grid cell allowing upward capillary fluxes from the water table, k_N (m/s) and z_N (m) are the hydraulic conductivity and the depth of the last hydrological node N, and z_{wtd} (m) is the depth of the water table. This flux is added to the second term of the right-hand side of equation (5) for the last hydrological node N. More details can be found in Vergnes et al. (2014).

2.2.8. River Processes Including Flooding and Groundwater

Two prognostic equations are used to represent the floodplain (F_w), and the stream, S_w (kg), reservoirs as follows:

$$\frac{\partial F_w}{\partial t} = q_{F_{in}} - q_{F_{out}} + A_{ctrip}\left(P_{fld} - I_{fld} - E_{fld}\right) \tag{14a}$$

$$\frac{\partial S_w}{\partial t} = q_{in} + q_{riv} + A_{ctrip}Q_s + q_{F_{out}} - q_{F_{in}} - q_{dis} \tag{14b}$$

where q_{in} (kg/s) is the water inflow from the adjacent upstream grid cells, q_{dis} (kg/s) the river discharge to the downstream grid cell, $q_{F_{in}}$ (kg/s) and $q_{F_{out}}$ (kg/s) are the flood inflow and outflow, respectively (Decharme et al., 2012); P_{fld}, I_{fld}, and E_{fld} (kg $\cdot$ m^{-2} $\cdot$ s^{-1}) the precipitation interception by the floodplains, the reinfiltration and the direct free water surface evaporation estimated by ISBA$_{DF}$, respectively; and q_{riv} (kg/s) is the groundwater-river exchange flux (Vergnes et al., 2012).

Because ISBA$_{DF}$-CTRIP is used for climate or hydrological applications at a coarse resolution, the groundwater scheme only accounts for widespread unconfined aquifers reached by diffusive groundwater

movements. The groundwater dynamic is solved by a one-layer two-dimensional diffusive equation as follows:

$$\omega_{eff} \frac{\partial h_w}{\partial t} = \frac{1}{r^2 \cos(\varphi)} \left[\frac{\partial}{\partial \theta} \left(\frac{T_\theta}{\cos(\varphi)} \frac{\partial h_w}{\partial \theta} \right) + \frac{\partial}{\partial \varphi} \left(T_\varphi \cos(\varphi) \frac{\partial h_w}{\partial \varphi} \right) \right] + \frac{1}{\rho_w} \left[Q_{sb} + Q_{sg} + Q_{ice} - Q_{riv} \right] \qquad (15)$$

where h_w (m) is the prognostic piezometric head; ω_{eff} (m^3/m^3) the aquifer effective porosity; θ and φ the longitude and the latitude coordinates, respectively' T_θ and $T\varphi$ (m^2/s) the transmissivities along the longitude and the latitude axes, respectively; Q_{ice} (kg $\cdot$ m$^{-2} \cdot$ s^{-1}) the ice sheet runoff; and Q_{riv} (kg $\cdot$ m$^{-2} \cdot$ s^{-1}) the groundwater-river exchange flux expressed in mass by unit area. The depth of the water table, z_{wtd}, used in equation (13) is then simply the difference between the piezometric head and the river topography (Vergnes et al., 2014). Note that when z_{wtd} reaches 1,000-m depth, all transmissivities are set to 0 in order to limit unrealistic abyssal water table depth. Groundwater mass can be diagnosed as the product between the aquifer effective porosity, the water density, and the thickness between this limit of 1,000 m below the soil surface and the simulated piezometric head.

Finally, the river discharge is directly related to the stream flow velocity, v_s (m/s), solved via Manning's formula (Arora & Boer, 1999) assuming a rectangular river cross-section as follows:

$$q_{dis} = \frac{v_s}{L_{riv}} S_w \qquad (16a)$$

$$v_s = s_{riv}^{1/2} \frac{\kappa}{n_{riv}} \left(\frac{W_{riv} h_s}{W_{riv} + 2h_s} \right)^{2/3} \qquad (16b)$$

where L_{riv} (m) is the river stream length accounting for a meandering ratio of 1.4 (Oki & Sud, 1998), s_{riv} (m/m) the river bed slope, κ (m^3/s) a conversion constant equal to 1, n_{riv} the dimensionless Manning roughness coefficient for the river, and W_{riv} (m) the river width. This velocity varies according to the stream height h_s (m), computed as the stream water mass ratio to the river area, which is the product of the river stream length and the river width (Decharme et al., 2010). Both floodplain inflow and outflow fluxes in equation 14 are also computed using Manning's formula (Decharme et al., 2012).

2.2.9. Implementation of CTRIP and Coupling With ISBA

The previous TRIP version from Oki and Sud (1998) was coded in Fortran 77 with binary I/O format, which limited its performance, the development of new physical components, and its ability to be coupled with others models. Accordingly, it has been recoded in Fortran 90 using the netcdf I/O format (https://www.uni-data.ucar.edu/software/netcdf/), and the previous global river channel network at 1° resolution has been increased to 0.5° resolution and enhanced over Europe. SURFEX now includes a coupling interface (Voldoire et al., 2017) based on the OASIS3-MCT coupler (Valcke et al., 2015). All exchanges between ISBA$_{DF}$ and CTRIP now run through this interface: all runoff fluxes, the surface water budget (precipitation interception minus infiltration and evaporation) of floodplains computed by ISBA$_{DF}$ and the depth of the water table, the fraction of the grid cell allowing upward capillary fluxes from the water table, the flooded fraction of the grid cell, and the potential mass of flood water that could infiltrate the soil computed by CTRIP.

3. Land Surface Parameters

The goal of this study is to document the behavior of the new CMIP6 ISBA$_{DF}$-CTRIP system and to compare it to the old CMIP5 ISBA$_{FR}$-TRIP system. Therefore, we describe here the land surface parameters used by the two versions of the model.

3.1. Vegetation and Soil

The land cover properties are specified according to the 1-km resolution ECOCLIMAP-II database (Faroux et al., 2013). More than 500 land cover units are derived from the Corine Land Cover map for the year 2000 at 100-m resolution over Europe and from the Global Land Cover 2000 database elsewhere. Theses land cover units are aggregated to the model resolution into 12 subgrid land tiles (Table 1 and Figure 2a) in order to account for land cover heterogeneities in both ISBA versions.
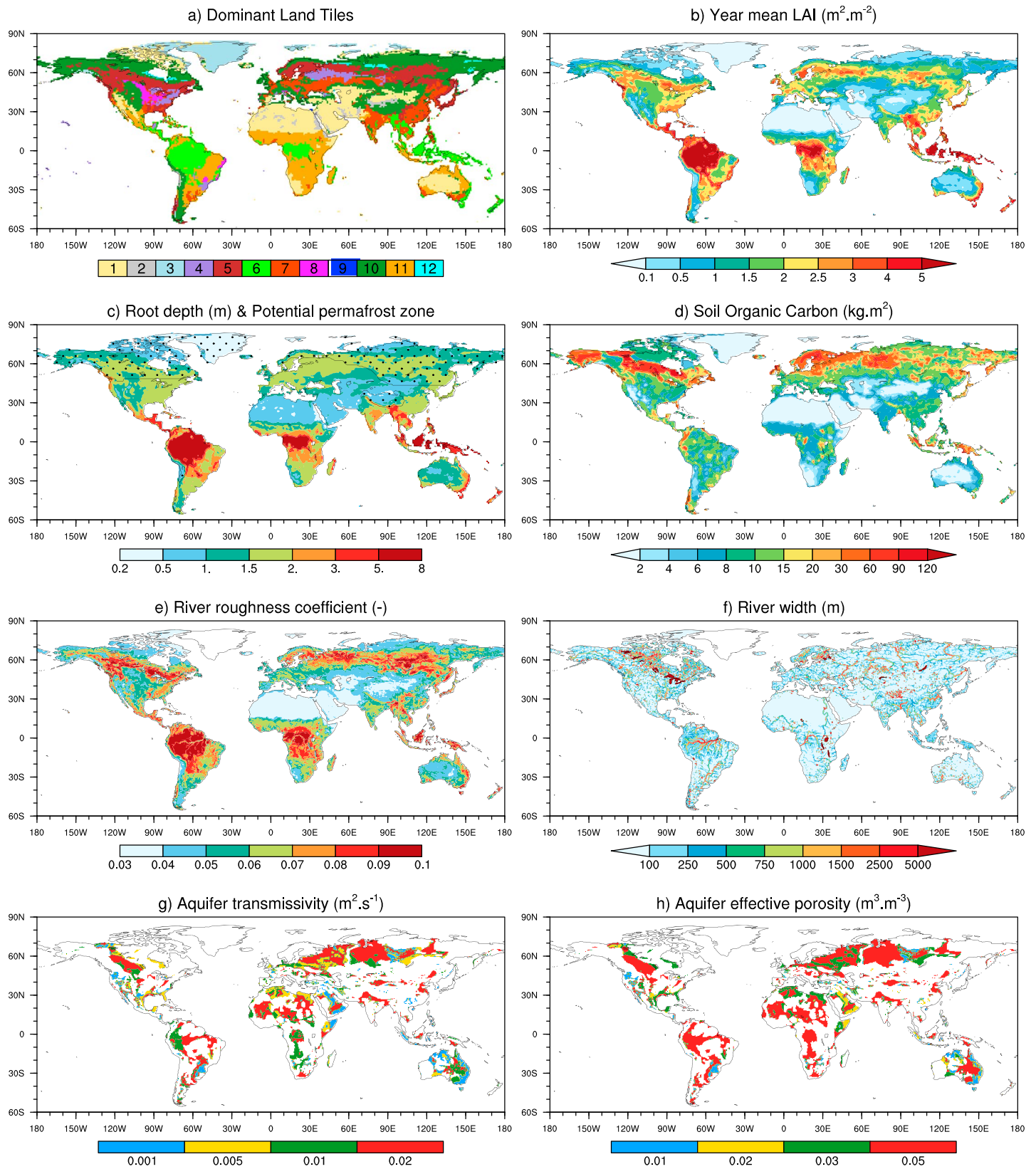
Figure 2. Global distribution of land surface parameters used in ISBA and CTRIP.

The average seasonal cycle of the LAI is imposed for each land cover unit at a 10-day time step. $ISBA_{DF}$ now includes a complete representation of carbon cycling in the vegetation, including photosynthesis, respiration, growth, and mortality. LAI can be calculated as the result of the carbon balance of the leaves or can be prescribed from climatological observations. We chose to prescribe LAIs in this study to facilitate the comparison with the old $ISBA_{FR}$ version. This annual cycle is computed using the collection 5 of the Moderate Resolution Imaging Spectroradiometer (MODIS) leaf area index product at 1-km spatial resolution combined with the Normalized Difference Vegetation Index product from the SPOT/Vegetation data set from 1 January 1999 to 31 December 2005 (Faroux et al., 2013). The annual mean values are show in Figure 2b. The depth of the roots (Figure 2c and Table 1) is specified for each land cover unit according to Canadell et al. (1996), while the thickness of the $ISBA_{FR}$ deep reservoir was arbitrary defined by Masson et al. (2003). The location of the potential permafrost regions (Figure 2c) where $ISBA_{DF}$ solves hydrology down to 12 m is determined manually based on the Circum-Artic Map of Permafrost and Ground Ice Conditions (CAMP-GIC; http://nsidc.org/data/ggd318) from Brown et al. (2002).

The snow-free land surface albedo is derived at a global scale for all land cover units at 1-km resolution from a 10-year analysis of the MODIS product (Carrer et al., 2014). Mean seasonal cycles at a 10-day time step for visible (0.3–0.7 μm) and near-infrared (0.7–5.0 μm) vegetation and vegetation-free albedos are then retrieved from the MODIS 2001 to 2010 period at 1-km resolution by using a Kalman Filter-based method. The total snow-free land surface albedo in a grid cell is computed via an arithmetic average between vegetation and vegetation-free albedos weighted by the fraction of vegetation. This fraction of vegetation in the grid cell is specified for each subgrid land tile (Table 1).

The soil textural properties, such as clay and sand, are given by the Harmonized World Soil Database (HWSD) at a 1-km resolution (FAO/IIASA/ISRIC/ISSCAS/JRC, 2012; http://webarchive.iiasa.ac.at/ Research/LUC/External-World-soil-database/HTML/). We also use the percentage of organic carbon f_{oc} (%) and the bulk density of the mineral matter ρ_m (kg/m^3) over two soil horizons (0–0.3 and 0.3–1 m) from HWSD to calculate the SOC (kg/m^2) content (Figure 2d) and the soil carbon density profile ρ_{soc} (kg/m^3; section 2.2.5) in each horizon as follows:

$$SOC = \rho_s \Delta z_s f_{oc}/100 \tag{17a}$$

$$\rho_s = 100 \left(\frac{f_{oc}/\alpha_{om}}{\rho_{om}} + \frac{100 - f_{oc}/\alpha_{om}}{\rho_m} \right)^{-1} \tag{17b}$$

where ρ_s (kg/m^3) is the total soil bulk density (Adams, 1973), α_{om} is the dimensionless van-Bemmelen value of 0.58 generally used to convert organic matter content to organic carbon content, ρ_{om} (kg/m^3) is the average bulk density of the organic matter set to 224 kg/m^3, and Δz_s (m) is the thickness of each HWSD soil horizon. Note that the SOC content has been set to 0 kg/m^2 over desert and glacier areas defined in the ECOCLIMAP-2 database.

3.2. Subgrid Topography

The topographic index used in both ISBA versions to determine the surface runoff via the TOPMODEL approach is specified from the HYDRO1K database (https://lta.cr.usgs.gov/HYDRO1K) at 1-km resolution. This distribution is calculated via a three-parameter gamma function derived from the mean, standard deviation, and skewness of the HYDRO1K actual distribution (Decharme et al., 2006, 2013).

CTRIP parameterizations require topographic information at a global scale and a high resolution. We use the Global Multi-resolution Terrain Elevation Data 2010 (GMTED2010; https://topotools.cr.usgs.gov/ gmted_viewer/) at a 7.5-arc-second (~250 m) spatial resolution (Danielson & Gesch, 2011) to derive (1) the river bed elevation needed to calculate the river elevation (Vergnes & Decharme, 2012); (2) the river bed slope needed by Manning's formula to compute the river flow velocity (Decharme et al., 2010); (3) f_{flood} the flooded grid cell fraction in the floodplains (Decharme et al., 2012) and $f_{wtd,}$ the grid cell fraction where upward capillary fluxes from the water table are allowed (Vergnes et al., 2014). The first step of the Vergnes et al. (2012) method is to compute these parameters at an intermediate resolution of 5 arcminutes (~10 km). In a second step we aggregate directly from 5 arcminutes to 0.5°. This method allows a better conservation of subgrid topographic properties from a very high to a low resolution.

3.3. River Geomorphological Parameters

The Manning formula and the Manning roughness coefficient are used to compute the flood flow in and out of the river. As proposed by Decharme et al. (2012), this coefficient for the floodplains, n_{fld}, is computed as the area average of the floodplain roughness coefficients n_i of each land type i present in the grid cell (Table 1):

$$n_{fld} = \sum_{i=1}^{19} \left(f_{land_i} \times n_i \right) \tag{18}$$

where f_{land} is the grid cell fraction of each land type. The Manning roughness coefficient for the river bed (Figure 2e) remains difficult to estimate at the global scale because it depends not only on poorly known mineral material in the channel bed but also on the surrounding vegetation. Decharme et al. (2012) used a simple linear function of the river stream order. Here we use a new method that offers better consistency between the roughness coefficients for the floodplain and river. The river roughness coefficient is calculated as a geometric average between the floodplain values and a standard value of 0.035 generally used for large rivers (Arora et al., 1999; Arora & Boer, 1999; Lucas-Picher et al., 2003; Yamazaki et al., 2011):

$$n_{riv} = 0.035^{1.0-\alpha_r} \times n_{fld}^{\alpha_r} \tag{19}$$

where α_r, is an empirical parameter that accounts for the fact that the roughness varies from low values in natural streams with deep pools, such as river mouths, to high values for small upstream rivers. This empirical parameter is computed using a simple linear relationship with the river stream order SO given by CTRIP in each grid cell of a given basin:

$$\alpha_r = \frac{1}{2} \left(\frac{SO_{\max} - SO}{SO_{\max} - SO_{\min}} + 1 \right) \tag{20}$$

where $SO_{\min}$ and $SO_{\max}$ are the minimum and maximum stream orders in each basin of the CTRIP network.

The river width (Figure 2f) is calculated using two steps. First, we use the following empirical relationship between the mean river width Ω_{riv} (m) and the mean annual discharges Q_{yr} (m^3/s) in each CTRIP grid cell:

$$\Omega_{riv} = \max \left(\Omega_{\min}, \alpha_W \times Q_{yr}^{\beta_W} \right) \tag{21}$$

where α_W and β_W are equal to 5.41 and 0.59, respectively, and $\Omega_{\min}$ (m) is the minimum river width in a grid cell set to 30 m. This relationship was developed by Vergnes et al. (2014) using a large set of 1,873 gauging stations across France with access to river width, river depth, and mean annual discharge measurements. The mean annual discharge in each CTRIP grid cell is estimated at the global scale using the GGHYDRO global runoff database (http://people.trentu.ca/~gcogley/glaciology/glglgghy.htm) from Cogley (2003). Second, we use a combination of two sources of satellite estimates: the Global Width Database for Large Rivers (GWD-LR; http://hydro.iis.u-tokyo.ac.jp/~yamadai/GWD-LR/) at 0.5° resolution (Yamazaki et al., 2014) and the Global Lakes and Wetland Database (GLWD; http://wp.geog.mcgill.ca/hydrolab/glwd/), which gives the lake fraction distribution at 0.5° resolution (Lehner & Döll, 2004). The final river width in CTRIP is then given by

$$W_{riv} = \max \left(\Omega_{riv}, W_{space} \right) \tag{22a}$$

$$W_{space} = \begin{cases} W_{GWD} & \forall W_{GWD} > 0 \\ \dfrac{f_{lake} A_{ctrip}}{L_r} & \forall W_{GWD} = 0 \end{cases} \tag{22a}$$

where f_{lake} is the GLWD lake fraction in each grid cell and W_{GWD} (m) the GWD-LR river width estimate. Finally, the river bankfull depth, h_{riv} (m), which controls the beginning of the river flood, is determined as follows, using an empirical relationship between observations of river width and maximum river height also proposed by Vergnes et al. (2014):

$$h_{riv} = \alpha_h \times W_{riv}^{\beta_h} \tag{23}$$

where α_h and β_h are equal to 1.4 and 0.28, respectively.

3.4. Aquifer Basin and Groundwater Parameters

Unconfined aquifers reached by diffusive groundwater movements are preferentially located in sedimentary basins with permeable porous and fractured rocks, and in alluvial plains characterized by gravel and sand materials with high permeability. Vergnes et al. (2012) developed a method to estimate the geometry of the aquifers and the groundwater parameters, such as transmissivity and effective porosity, using topographical, lithological, and geological information available over France.

A similar approach was developed at the global scale using available global data sets (Vergnes & Decharme, 2012). The global map of the groundwater resources of the world from the Worldwide Hydrogeological Mapping and Assessment Programme (WHYMAP; http://www.whymap.org) was used as the primary information for delineating groundwater basins. To refine this map, Antarctica and Greenland were removed, a slope criterion was applied to remove the mountainous cells, and the global map of lithology from Dürr et al. (2005) was used to refine the limits of the aquifers. This global lithological map is also used to attribute transmissivity (Figure 2g) and effective porosity (Figure 2h) values by type of lithology. Note that these groundwater parameters and the aquifer geometry specified by Vergnes et al. (2012) over France, while a more precise hydrogeological map from the U.S. Geological Survey (USGS; https://www.usgs.gov/products/maps/geologic-maps) is used to refine the geometry of the aquifers over the United States. As a result, the area covered by unconfined aquifers in CTRIP represents 43% of the land surface, excluding Antarctica and Greenland. More details can be found in Vergnes and Decharme (2012) and Vergnes et al. (2012).

4. Experimental Design

4.1. Atmospheric Forcing Products

Although several products exists, global offline evaluations of LSMs most often use only one atmospheric forcing, generally from one of two families of atmospheric reanalysis. The first family is related to the National Center of Environmental Prediction-National Center for Atmospheric Research (NCEP-NCAR) reanalysis and includes the 3-hourly Princeton Global Forcing (PGF; http://hydrology.princeton.edu/data.pgf.php) from Sheffield et al. (2006) and the 6-hourly CRU-NCEP forcing from Viovy (2018). The second is derived from the ECMWF ERA-40 or ERA-Interim reanalysis and includes the 3-hourly WFD or WFDEI forcing from Weedon et al. (2011, 2014, respectively) and a new 3-hourly forcing from the Earth2Observe (E2O; http://www.earth2observe.eu/) European project (Schellekens et al., 2017). In this study, we choose to perform the ISBA$_{DF}$-CTRIP evaluation using two of these atmospheric forcings in order to dissociate improvements due to changes in the land surface physics from uncertainties in the land surface response to one specific atmospheric forcing (Decharme & Douville, 2006b; Gelati et al., 2018; Szczypta et al., 2012).

First, we use the 3-hourly PGF version 1 data set at 1° resolution over the 1948 to 2010 period. This data set is based on the NCEP-NCAR reanalysis corrected for biases at diurnal, daily, and monthly timescales using a variety of observational data sets for air temperature, total radiative fluxes, or precipitation. The PGF precipitation forcing used in this paper is hybridized to match the monthly values from the gauge-based Global Precipitation Climatology Center (GPCC) Full Data Product V6 (Schneider et al., 2011, 2014). Second, we use the Tier-2 Water Resources Re-analysis (WRR2) forcing from the E2O project, available at 0.25° resolution and re-gridded to 1° resolution using conservative remapping. This data set is directly based on the 3-hourly ERA-Interim reanalysis (https://www.ecmwf.int/en/forecasts/datasets/reanalysis-datasets/era-interim) over the 1979–2014 period. In the E2O project, only the 2-m air temperature and humidity and the surface pressure have been corrected for differences between topography at 0.25° resolution and ERA-Interim topography at ~70-km resolution. Monthly precipitations have been hybridized with observations using the Multi-Source Weighted-Ensemble Precipitation (MSWEP; http://www.gloh2o.org) data set (Beck et al., 2017).

The MSWEP-based E2O precipitation rate is globally larger than GPCC-based PGF data (Figure 3). This difference is mainly located in northern high-latitude regions, which is certainly due to the wind catch ratio corrections on snowfall rate performed by the MSWEP product. The 2-m air humidity exhibits the largest difference between both forcing products. Air is drier with E2O than with PGF, and this is especially true over tropical regions. The 2-m air temperature is very similar in the two products, although the E2O eastern
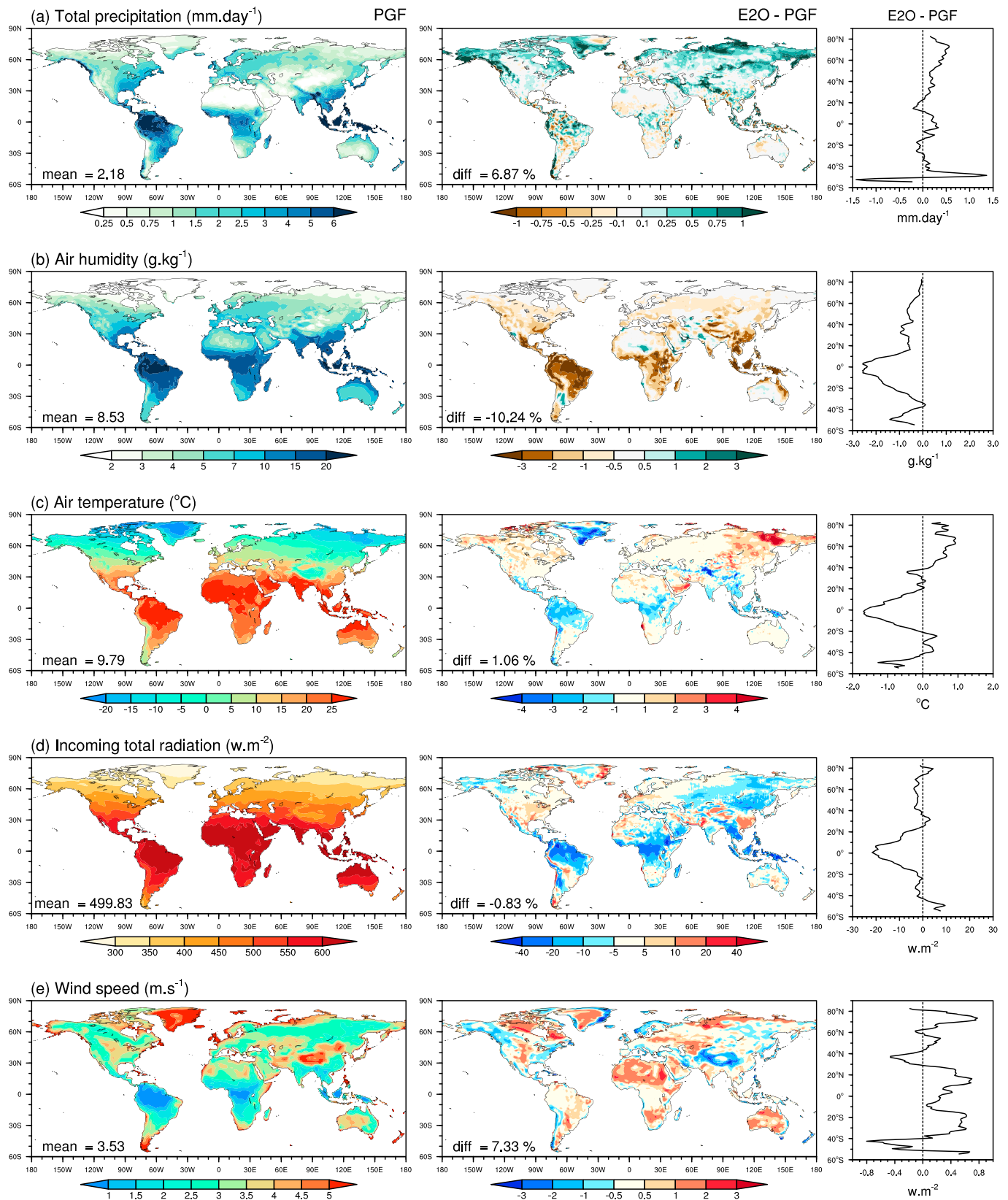
Figure 3. Global distributions of the annual means of NCEP-GPCC-based PGF meteorological data (left panels) and their differences with ERA/Interim-MSWEP-based E20 atmospheric forcing variables (center panels). Zonal averages of these differences are also shown in right panels.

Table 2
Simulations performed in this study

Name	Land surface processes	Atmospheric forcing (reanalysis/precipitation)
sfxcm5_pgf	Old cm5 physic: Force-restore 3-layer soil hydrology and 4-pseudo-layer	PGF (NCEP/GPCC)
sfxcm5_e2o	temperature; One-layer snow; Jarvis Transpiration0.5° CTRIP with	E2O (ERA-I/MSWEP)
	daily one-way coupling and variable velocity	
sfxcm6_pgf	New cm6 physics: Multi-layer soil (14-L) and snow (12-L);	PGF (NCEP/GPCC)
sfxcm6_e2o	Transpiration from photosynthesis; Floodplains; Groundwater	E2O (ERA-I/MSWEP)
	0.5° CTRIP with 3-hourlytwo-way coupling and variable velocity	
isbcm6_pgf	cm6 physic butNo Flood and No Groundwater (nfg)	PGF (NCEP/GPCC)
gwcm6_pgf	cm6 physic with Groundwater but No Flood (gnf)	

Note. ISBA and CTRIP embedded in SURFEXv8 (*sfx*) are used with the old land surface physics applied in CNRM-CM5 (*cm5*) and the new physics developed for CNRM-CM6 (*cm6*). Three intermediate simulations are also performed.

Siberian regions are warmer than with PGF, and inversely over the tropics. The total downward incoming radiations are not very different. E2O radiations are generally lower than PGF, except in some regions, like Europe and North America. Finally, wind speeds are quite different, with, in general, a larger intensity in the E2O forcing compared to PGF.

4.2. Experiments

With the help of the SURFEX numerical interface, both versions of ISBA are run at 1° resolution with a time step of 900 s, while CTRIP is run at 0.5° resolution with a time step of 1800s. We chose the 1° resolution for ISBA to be close to the CNRM-CM6 climate model spatial resolution run at a T127 reduced gaussian grid (~1.4° in both longitude and latitude). The evaluation is performed over the 1979–2010 period using several products related to snow cover, snow depth, permafrost characteristics including seasonal active layer depth, seasonal floodplain areas, groundwater water table depths, soil moisture, land evapotranspiration, river discharges, and variations in terrestrial water storage.

The previous ISBA$_{FR}$-TRIP version used in CNRM-CM5 will be referred to as *sfxcm5* throughout this paper (Figure 1a), while the new ISBA$_{DF}$-CTRIP version used in CNRM-CM6 will be called *sfxcm6* (Figure 1b). To facilitate the comparison between the new and old models, we use the new CTRIP version at 0.5° resolution with a daily one-way coupling and the variable flow velocity instead of the old TRIP at 1° resolution with a constant velocity. The hydrological impacts of using constant or variable streamflow velocities have been well documented in Decharme et al. (2010). With these two LSMs and the two atmospheric forcings, we perform four main simulations described in Table 2.

To equilibrate slow land surface reservoirs (snow over inland glacier, deep soil moisture and temperature, or aquifer piezometric head), a spin-up of 150 years was performed with the PGF forcing for *sfxcm5_pgf* and *sfxcm6_pgf* by cycling the model over the 1948 to 1957 period before running it up to 2010. For *sfxcm5_e2o* and *sfxcm6_e2o* E2O simulations, spin-ups start from their twin PGF simulations on 1 January 1959 and an additional spin-up period of 20 years is used to reach 1 January 1979 by cycling the model over the 1979 to 1983 forcing dates.

In addition, two simulations using the PGF forcing (Table 2) will be occasionally shown to expose model behaviors to successive physical changes. *isbcm6_pgf* uses the same physical core as *sfxcm6_pgf* but without the floodplain and groundwater schemes, while groundwater parameterization is added in *gwcm6_pgf*. Comparisons of these experiments with *sfxcm5_pgf* and *sfxcm6_pgf* will help us dissociate changes in ISBA physics (from ISBA$_{FR}$ to ISBA$_{DF}$) from the impacts of flooding processes and groundwater dynamics with an upward capillary rise.

5. Evaluation of Northern Hemisphere Snow and Permafrost

5.1. Snow Cover

We illustrate changes in snow physics by first comparing simulated and observed snow cover extents over the northern hemisphere. Observations come from weekly satellite estimates distributed by the National

Snow and Ice Data Center (NSIDC) at 25-km horizontal resolution over the 1966 to 2016 period (Brodzik & Armstrong, 2013). These observations have been remapped at 1° resolution and averaged at a monthly timescale as proposed by Peings et al. (2013). They are compared to the snow fraction simulated by *sfxcm5* (equation (A2)) and *sfxcm6* (equation (2b)). Climatological seasonal cycles in Figure 4 are computed over the 1979–2010 period, but only autumn (SON), winter (DJF), and spring (MAM) seasons are shown. Because simulations with both forcing are very similar, only spatial patterns of PGF experiments are presented, while all simulations are shown on zonal averages.

During autumn and winter, spatial patterns, pattern skill scores, and zonal averages highlight the strong improvements due to the new snow scheme. However, these improvements are as much due to the new snow fraction formulation (equation (2b)) as to the new snow physics. During spring, spatial patterns and zonal averages show that *sfxcm6* (with both forcings) underestimate the snow extent, especially between 50° and 70° north, pointing to an early snowmelt over the boreal forest. The $ISBA_{DF}$ explicit snow scheme does not take vegetation into account. For low vegetation, this assumption is reasonable because vegetation is covered by snow and plays a lesser role. But it is not valid for the boreal forest, where tall trees reduce the visible incident radiation reaching the snowpack, delaying the snowmelt compared to low or unvegetated areas. In addition, the specific snow fraction over tall vegetation is generally very low (equation (2c)), annihilating the soil insulation effect of the snowpack. Consequently, the soil-vegetation-flood composite surface temperature (Appendix B) rises rapidly over 0 °C, inducing an unrealistic snowmelt at the base of the snowpack. This weakness is not found with the *sfxcm5* snow scheme principally because the snow temperature, which is approximated by a weighted combination of the surface and the subsurface temperatures depending on the grid cell vegetation fraction, contributes to the distribution of the snowmelt over the entire spring season. Over mountainous regions (Himalayas, Alps, Rocky, etc.), the snow disappears too rapidly in both versions of the model. In these areas, the snowmelt timing is mostly correlated to the strong change in air temperature and incoming solar radiation with elevation (Lafaysse et al., 2011; Lundquist et al., 2004; Nijssen et al., 2001). This subgrid process is not yet represented in the model.

Interannual variability is also briefly studied in terms of the standard deviation of monthly detrended anomaly time series, σ_{ano} (Figure 4). These monthly anomalies are computed by subtracting the mean annual cycle from the observed or simulated detrended time series over the 1979 to 2010 period. The simulated interannual variability is generally underestimated but less so by *sfxcm6_pgf,* as shown by the global ratio of simulated to observed σ_{ano}. The new model has a better representation of regional patterns (better pattern skill scores). Regions with an observed low seasonal snow cover (USA, Europe, Southeast Siberia, and Himalaya) exhibit the largest interannual variability compared to regions subject to high snow cover. This contrast is better reproduced with *sfxcm6* than with *sfxcm5*. Finally, the comparison between observed and simulated zonal averages reveals that these results are similar whatever the atmospheric forcing.

5.2. Snow Depth

For an exhaustive evaluation of the simulated snowpack, we use a large set of snow depth in situ measurements. Several daily observations were gathered at 2,121 stations from the last century to the present. These stations are located in different countries of the Northern Hemisphere. Because many measurements are taken at synoptic stations following the World Meteorological Organization standards, many observations cover bare-ground open areas or clearings with regular grass cutting. More details of this data set can be found in Brun et al. (2013) and in the supporting information (section 2.2; https://doi.org/10.5194/essd-9-389-2017-supplement) of Schellekens et al. (2017). From this entire network, we have selected 1,271 stations from 1979 to 2010 using the criteria set by Brun et al. (2013): (1) the difference between the local and model elevation, here at 1° resolution, is less than 100 m to avoid temperature biases due to the low resolution of the forcing; (2) the number of days with a nonzero snow depth measurement over the entire period is greater than 100 days; (3) there are at least 8 days with snow per year. Biases in simulating the mean annual snow depth (Figure 5a), the mean daily duration of continuous snow (Figure 5b), and the mean last day of continuous snow on the ground (Figure 5c) for *sfxcm5* and *sfxcm6* are analyzed considering that a day with snow on the ground is defined as a day with snow depth higher than 1 cm. The corresponding global skill scores are given in Table 3 with additional variables such as interannual daily detrended anomalies, the mean first day of continuous snow, and the mean date of the annual snow depth maximum.
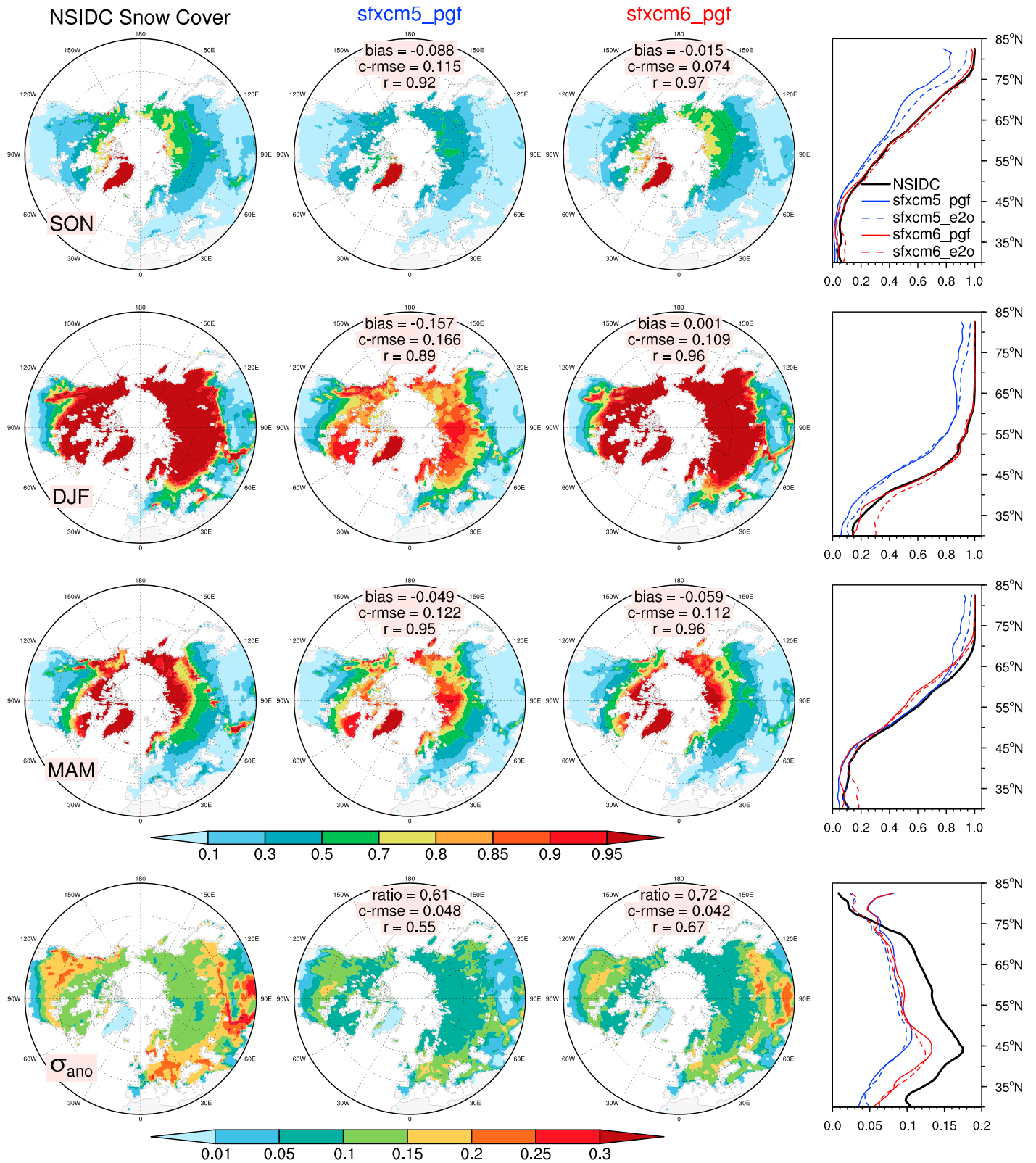
Figure 4. Northern Hemispheric distributions of mean seasonal snow cover extents observed (black) and simulated by the old *sfxcm5* (blue) and the new *sfxcm6* (red) model versions during autumn (SON), winter (DJF), and spring (MAM) over the 1979–2010 period, with pattern skill scores (mean bias, centered root-mean-square error, c-rmse, and correlation, r). Bottom panels present spatial distributions of standard deviations of monthly detrended anomaly time series (σ_{ano}) over the same period. Right column: associated zonal averages. All experiments are summarized in Table 2.
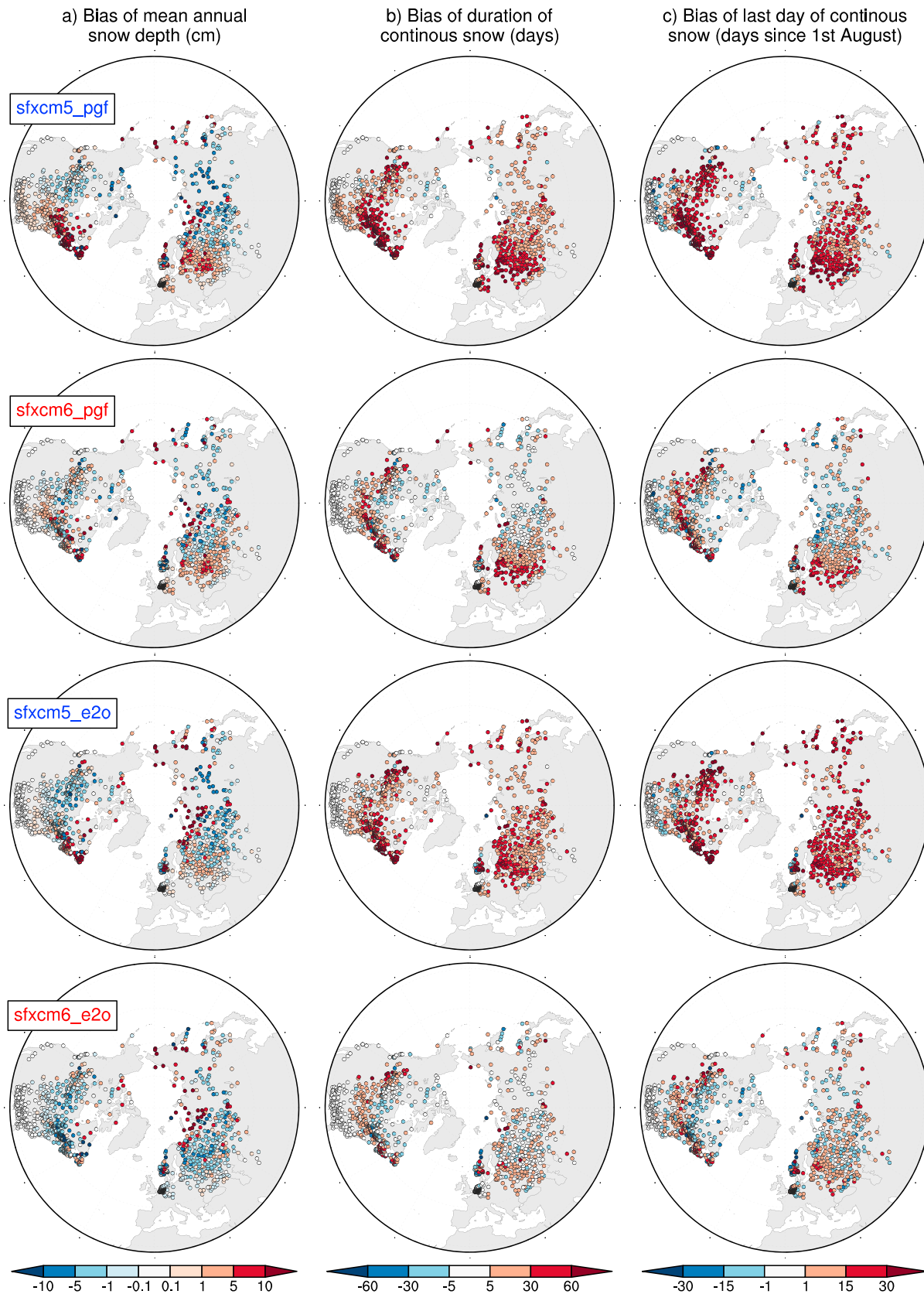
Figure 5. In situ comparison between observed and simulated snow depths over the 1979–2010 period. The relative global skill scores are given in Table 3.

Table 3
Observed versus simulated snow skill scores reached at the 1271 snow in situ station

Variables	Criteria	Experiments			
		sfxcm5_pgf	sfxcm6_pgf	sfxcm5_e2o	sfxcm6_e2o
Daily Snow Depth (cm)All Season	*bias*	1.51	**0.37**	0.45	−0.58
	c-rmse	13.1	10.6	11.0	**9.49**
	r	0.73	0.80	0.80	**0.84**
Daily Interannual Snow Depth Anomalies (cm)	*c-rmse*	8.51	7.87	6.66	**6.06**
	r	0.37	0.45	0.58	**0.65**
Annual Duration of Continuous Snow (days)	*bias*	26.03	10.40	19.14	**3.38**
	c-rmse	31.99	26.78	28.18	**22.03**
	r	0.93	0.94	0.95	**0.96**
First day of Continuous Snow (days)	*bias*	−14.51	−7.22	−8.07	**−2.66**
	c-rmse	30.18	27.05	22.736	**20.04**
	r	0.74	0.78	0.85	**0.86**
Date of Annual Maximum Snow Depth (days)	*bias*	6.17	−7.18	7.60	**−1.67**
	c-rmse	43.32	38.85	34.36	**32.45**
	r	0.43	0.40	**0.60**	0.59
Last day of Continuous Snow (days)	*bias*	14.86	5.32	15.20	**2.96**
	c-rmse	32.49	27.23	24.16	**20.61**
	r	0.78	0.81	0.87	**0.88**

Note. The *bias*, centered root mean square errors (*c-rmse*) and correlation (*r*) are shown.

Snow depth bias scores are not very different between *sfxcm5* and *sfxcm6*, even though the mean snow depth is lower with the new snow scheme because it simulates larger snow density, especially in spring. All other scores in Table 3 show that the mean annual snow depth is globally improved in *sfxcm6*. The snow season is also shorter, with the new scheme consistent with the lower snow depth (Figure 5). Skill scores for mean snow duration, mean last day of continuous snow, mean first day of continuous snow, and mean date of the annual snow depth maximum are significantly improved by the new snow scheme (Table 3).

These results indicate that the snow seasonal cycle is much better reproduced using *sfxcm6* compared to *sfxcm5*, in agreement with our former analysis over Northern Eurasia (Decharme et al. (2016). The most important effect appears in springtime, when snowmelt is faster with *sfxcm6*, albeit slightly too fast over the north of Canada and eastern Siberia. This faster snowmelt is beneficial here because most in situ measurements are from clearings with short grass or from vegetation-free areas.

Improvements in *sfxcm6* correlations and centered root-mean-square errors for all climatological variables, together with improvements in daily snow depth anomalies skill scores, indicate that the interannual variability is also well captured by the new model. Finally, Figure 5 and Table 3 confirm that simulations based on ERA-Interim forcing generally outperform those driven by PGF. As shown by Brun et al. (2013), the PGF forcing suffers from an inconsistency between the chronology of precipitation and temperature, affecting the snow depth simulation in winter.

5.3. Permafrost Boundaries and Active Layer Depth

In addition to its importance for the evolution of the climatic system, the simulation of permafrost characteristics is a good test of the model's ability to reproduce snow and soil processes over northern regions (Decharme et al., 2016; Paquin & Sushama, 2014). To evaluate the simulated permafrost in *sfxcm6* experiments, we first use the CAMP-GIC data (Brown et al., 2002) from the NSIDC, which estimates limits of continuous, discontinuous, sporadic, and isolated permafrost regions. The simulated permafrost margins (Figure 6) are represented by spatial patterns of the mean permafrost Active Layer Depth (ALD). This simulated ALD is computed as the maximum soil depth reached each year in summer by the 0 °C isotherm. This depth is estimated via a linear interpolation between the last positive temperature node going down from the surface and the first negative temperature node. Permafrost boundaries are globally well reproduced, by the model even if these limits extend slightly too far south in both western Siberia and eastern Canada. Permafrost margins over Tibetan Plateau are fairly well simulated. Over temperate mountains (Alps, Pyrenees, Appalachia, etc.), the model is not able to simulate permafrost soils due to the low resolution of
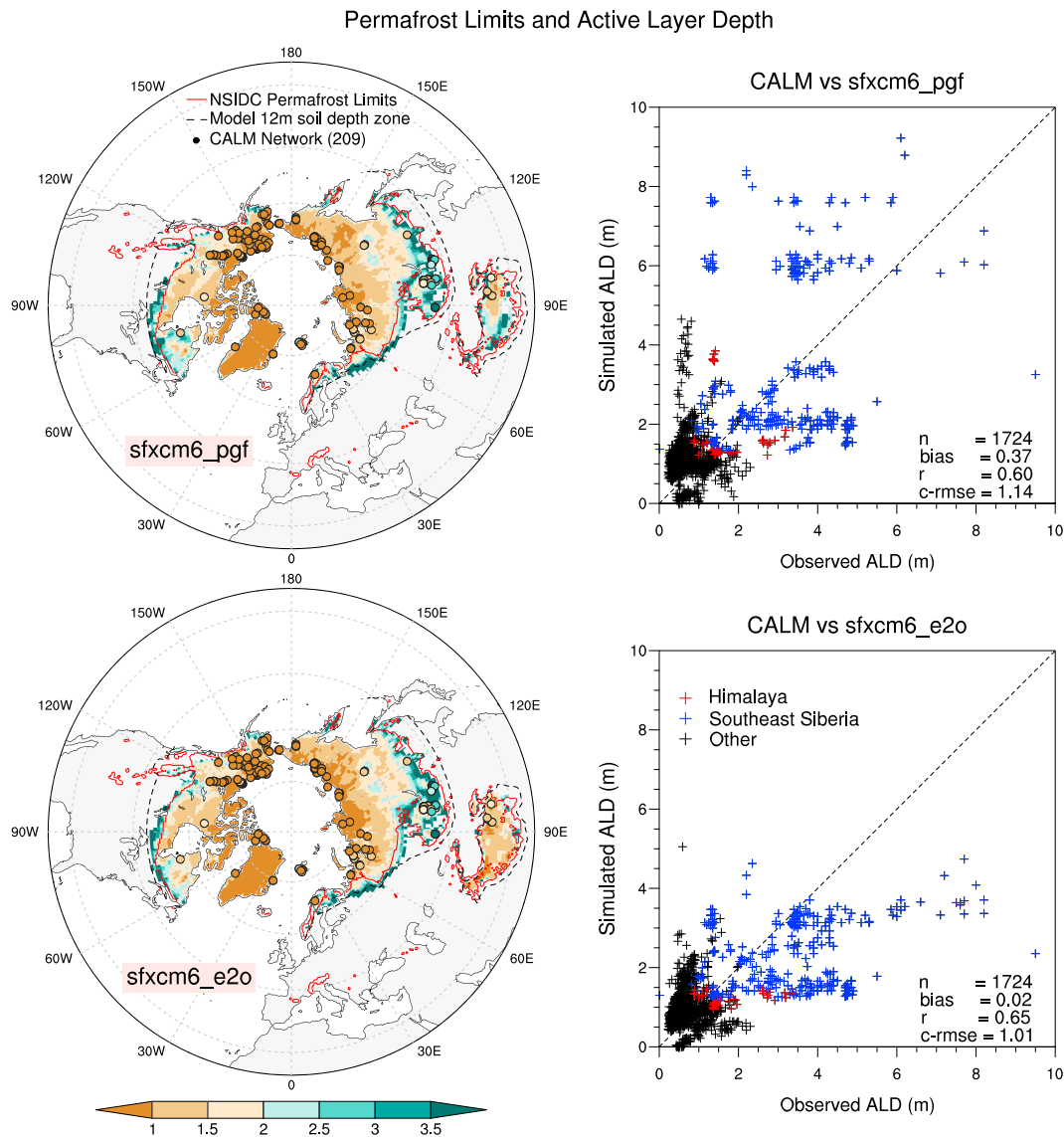
Figure 6. Comparison of observed and simulated northern hemispheric permafrost characteristics. In the left panels, red lines correspond to the NSIDC estimated limits of permafrost regions, dashed black lines to boundaries where the ISBA$_{DF}$ soil depth for hydrology is set to 12 m (cf. section 3 and Figure 2), patterns of the mean ALD simulated over the 1990–2010 period by the new model with each forcing, circles to ALD observations from the CALM network. Scatterplots on the right compare all simulated yearly ALD with CALM observations. Red crosses correspond to Himalayan stations, blue crosses to stations located in the southeast regions of Siberia (45–60°N), black crosses to stations over continuous permafrost. Skill scores over the 1,724 measurements are also given.

the atmospheric forcing. Spatial patterns in Figure 6 also show that the quality of the simulated permafrost boundaries does not depend on the limit where the ISBA$_{DF}$ hydrologic soil depth in *sfxcm6* is fixed to 12 m (black lines in Figure 6).

Second, we use the Circumpolar Active Layer Monitoring (CALM; http://www.gwu.edu/~calm/) network, which uses 239 in situ stations (Brown et al., 2000) to directly evaluate simulated ALD over the 1990 to 2010 period. CALM measures the end-of-season permafrost thaw depth each year, which is comparable to the simulated annual maximum ALD. After removing stations outside the domain or the studied period, 209 stations remain for evaluating the model. The period-mean of the observed ALD is represented by circles on the maps in Figure 6. This quantitative comparison shows that the ALD spatial distribution is well reproduced by the model no matter the atmospheric forcing. Scatterplots in Figure 6 directly compare the simulated and observed ALD at each station and for each year. The largest error is logically found in the southeast part of Siberia (45–60°N), where the low resolution of the atmospheric forcing does not allow the observed

ALD, mainly located over isolated or sporadic permafrost, to be represented accurately. Elsewhere, over the continuous permafrost region or over the Himalayan plateau, the simulated ALD reproduces in situ measurements well. The resulting skill scores given in each scatter plot lead to two main conclusions: (1) errors in simulating ALD are small, or at least reasonable, considering the low resolution of the model and with regard to other model results (Dankers et al., 2011; Ekici et al., 2014; Gouttevin et al., 2012; Guimberteau et al., 2018; Guo et al., 2017; Koven et al., 2009; Paquin & Sushama, 2014); (2) the quality of the ALD simulation is independent of the atmospheric forcing used even though the *sfxcm6_e2o* simulation with ERA-Interim-based E2O forcing exhibits slightly better scores than the PGF-driven simulation (*sfxcm6_pgf*).

6. Evaluation of the Global Water Budget

6.1. Major Land Surface Reservoirs

6.1.1. Floodplains

To evaluate floodplain inundation simulations in *sfxcm6*, we use satellite-derived inundation estimates over the 1993–2004 period from Prigent et al. (2007). This global data set is derived from a complementary suite of satellite observations that quantifies the monthly variations of the distribution of surface water extent at ~25-km resolution (Papa et al., 2010; Prigent et al., 2007). In this study, this data set is remapped at 0.5° resolution and corrected from lakes, bogs, fens, and mire areas of the GLWD database, as well as from monthly irrigated areas using the Monthly Irrigated and Rainfed Crop Areas around the year 2000 product (Portmann et al., 2010). Details on the correction method can be found in Decharme et al. (2012). Both the annual mean and detrended monthly anomalies of these corrected flooded floodplains estimates (hereafter $P_{07/\text{GM}}$) are compared to simulations (*sfxcm6_pgf* and *sfxcm6_e2o*) in Figure 7.

The global distribution of the *sfxcm6_pgf* simulated inundated area is reasonably reproduced (see pattern correlation score Figure 7a), although these simulated areas remain strongly underestimated, especially over western Siberia (Ob basin) and southern Asia. *sfxcm6_e2o* gives similar results (pattern correlation of 0.45) to *sfxcm6_pgf* (not shown). Globally, simulated inundated areas cover 0.25×10^6 km^2 for *sfxcm6_pgf* and 0.19×10^6 km^2 for *sfxcm6_e2o* against 1.11×10^6 km^2 from estimates.

The comparison over the Amazonian region exhibits the same weaknesses (Figure 7b), with simulated inundated areas covering 0.65×10^5 km^2 for *sfxcm6_pgf* and 0.59×10^5 km^2 for *sfxcm6_e2o* versus 2.44×10^5 km^2 from the estimate. The model logically simulates inundations only in those grid cells of the hydrological network that correspond to major streams. However, P07/GM estimates larger inundations even in the grid cells adjacent to major streams. This difference partly explains the generalized underestimation found in simulations of global floodplain inundation. Additional reasons are discussed at length in Decharme et al. (2012) and may be related to uncertainties in atmospheric forcing, the computational method of the topography-based subgrid functions used to define f_{flood}, the model physics (for example, the nonrepresentation of seasonal thermokarst lake over permafrost area), and/or satellite retrieval algorithms (Papa et al., 2010).

In terms of interannual variability, detrended monthly anomalies are reproduced slightly better over the Amazon region (Figure 7d) than globally (Figure 7c). The amplitude of these anomalies is generally underestimated by *sfxcm6*. The model is not able to reproduce negative anomalies during the 2000 to 2001 period (Figure 7d). Excluding this period, correlation skill scores increase from 0.26 to 0.49 for *sfxcm6_pgf* and from 0.31 to 0.42 for *sfxcm6_e2o*.

6.1.2. Groundwater

The direct evaluation of groundwater dynamics is a difficult task at the global scale because no gridded observations and/or global time series exist at a continental scale, although many in situ piezometric head measurements can be collected from some regions of the world (Fan et al., 2013; Vergnes et al., 2012). In addition, it is rather difficult to compare local observations of water table depth, noted hereafter as z_{wtd}, with a simulation at a resolution larger than 1 km because the model cannot reproduce the impact of the local topography or the fine-scale variations of the geology. So we chose to compare our model to the very fine resolution model used in Fan et al. (2013), denoted hereafter as *Fan2013*, providing simulated global equilibrium z_{wtd} estimates at 30 arc-second (~1 km) resolution. The *Fan2013* simulation has been validated against a vast network of in situ piezometric head measurements. This product is available at 0.25° resolution and has been aggregated to the CTRIP resolution of 0.5° using conservative remapping.
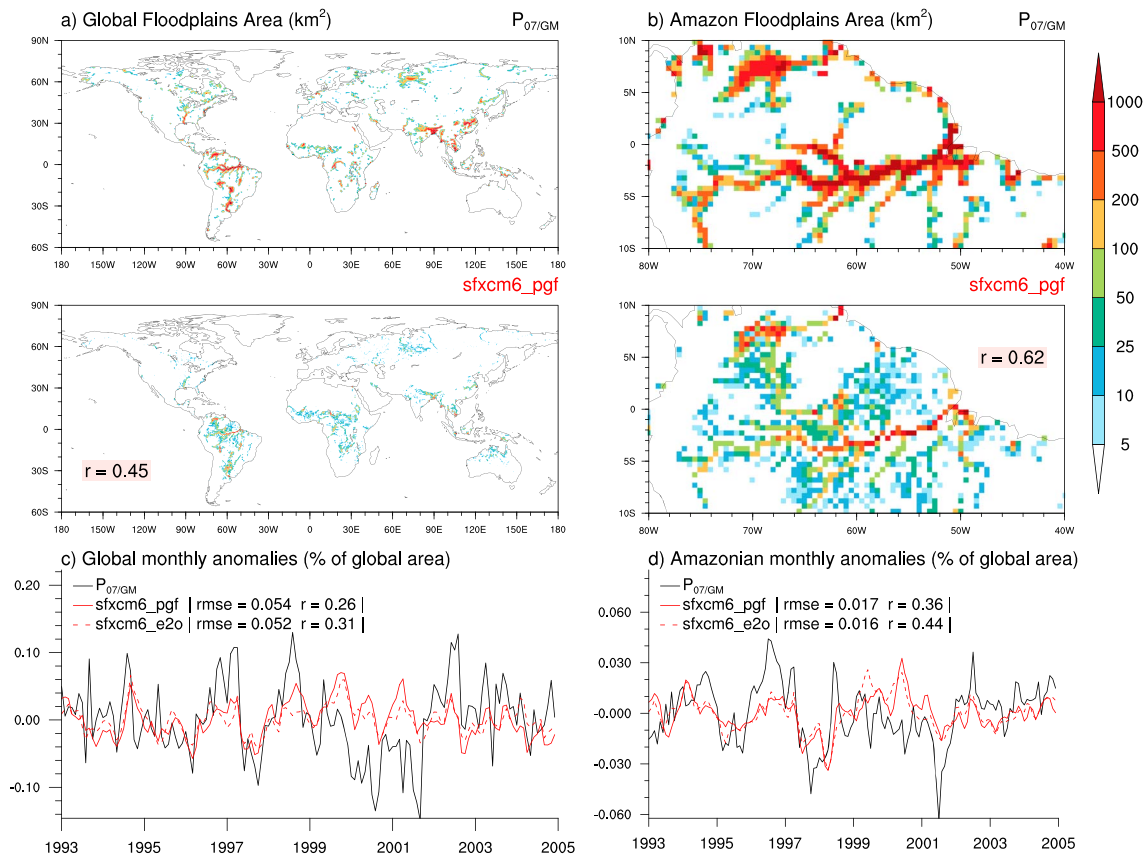
Figure 7. Comparison between satellite-estimated and simulated annual mean floodplains areas over (a) the globe and (b) the Amazonian region during the 1993–2004 period with corresponding pattern correlations. Monthly detrended anomaly time series averaged over (c) the globe and (d) the Amazonian region with their associated root-mean-square error (rmse) and correlation (r) skill scores.

Figure 8a presents the *Fan2013* global equilibrium z_{wtd} estimate restricted to CTRIP aquifer basins. Shallow z_{wtd} are generally located over the flattest and wettest regions of the world—for example, northern Canada, western Siberia, Amazonia, and Ganges valley. Inversely, deepest z_{wtd} take place in dry and/or hilly areas. The *sfxcm6_pgf* simulated annual mean z_{wtd} computed over 1979–2010 (Figure 8b) reasonably agrees with such estimates, at least over flat and humid regions (Figure 8c). Note that the *sfxcm6_e2o* simulation is not represented because it reproduces similar results (mean z_{wtd} of 31.1 m and pattern correlation of 0.43) to *sfxcm6_pgf*. Over regions with a complex orography, *sfxcm6* simulates a shallower annual mean z_{wtd} than *Fan2013* estimates. In fact, except in dry areas, the simulated annual mean z_{wtd} generally reaches no more than 3- or 4-m depth. This is coherent with *Fan2013*, which demonstrates, using piezometric head measurements, that it is common for natural z_{wtd} to be less than 5 m.

Our groundwater scheme represents only unconfined aquifers connected to the river where z_{wtd} is dynamically constrained by the river elevation. The simulated z_{wtd} is thus only related to the subgrid part of the grid cell with a topography similar to that of the river (Vergnes et al., 2014). In other words, CTRIP is built to represent only shallow z_{wtd} close to the river, while *Fan2013* accounts for all topographical structures in the grid cell due to its very fine native resolution. This fact also explains why a subgrid fraction of the grid cell, f_{wtd}, must be considered to account for the upward capillarity rise of the soil. The simulated annual mean f_{wtd} is logically at its maximum over the world's flattest areas (Figure 8d) where the differences between *Fan2013* and *sfxcm6* are lowest (Figure 8c). Over desert areas, *sfxcm6* simulates deeper z_{wtd} than *Fan2013* estimates due to differences in the model structure. The transmissivities of vertically homogeneous aquifers in CTRIP allow z_{wtd} to go down to several hundred meters, while the *Fan2013* transmissivities account for an exponential profile with a depth limiting z_{wtd} to roughly one hundred meters. Whatever this difference, z_{wtd} is so deep in these regions that its impact on both the surface hydrology and the atmosphere is null.
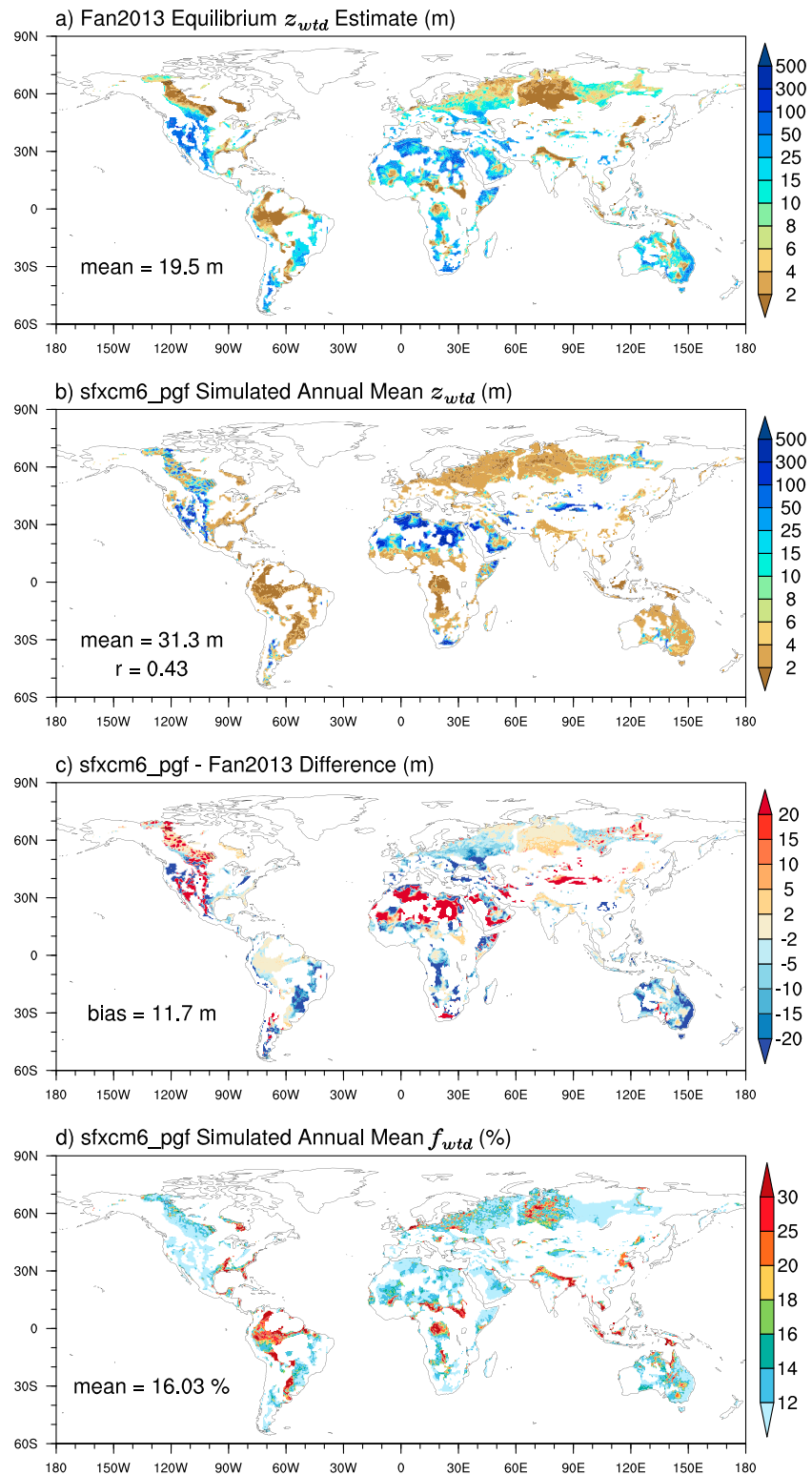
Figure 8. Comparison between (a) the equilibrium water table depth (z_{wtd}) estimated by Fan et al. (2013) and (b) the annual mean dynamic z_{wtd} simulated by *sfxcm6_pgf* during the 1979 to 2010 period. The global mean is given for each product and the spatial correlation, *r*, for the *sfxcm6_pgf* simulation. This figure also shows (c) the difference between both product with the associated bias and (d) the simulated annual mean subgrid fraction of the grid cell, allowing the water table to rise (f_{wtd}) with its global mean.
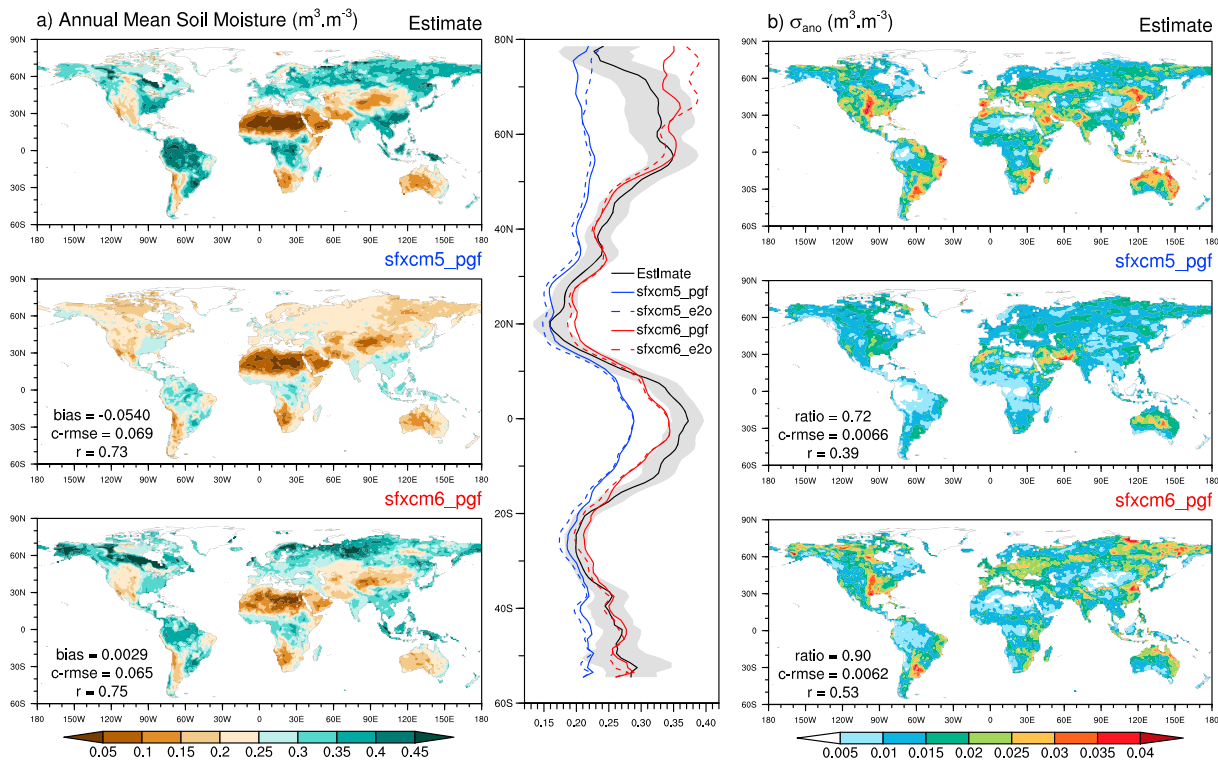
Figure 9. Comparison between (a) estimated and simulated annual mean soil moisture with their zonal average and (b) standard deviations of monthly detrended anomaly time series over the 1980–2010 period. The estimate comes from an arithmetic average of the GLEAM and ERA-I/Land products. Zonal averages of annual means for the *sfxcm5* (blue) and the *sfxcm6* (red) model versions are compared to the estimate (black) and the minimum and maximum values between GLEAM and ERA-I/Land products (gray shaded area). Pattern skill scores are the same as in Figure 4.

6.1.3. Soil Moisture

The evaluation of soil moisture at the global scale is not easy due to the lack of gridded observations, but some estimates can be used. Here we compare *sfxcm5* and *sfxcm6* simulations with available global data sets such as the Global Land Evaporation Amsterdam Model (GLEAM; https://www.gleam.eu/) root zone soil moisture and the ERA-Interim/Land (ERA-I/Land) total soil moisture reanalysis (https://www.ecmwf.int/en/forecasts/datasets/archive-datasets/reanalysis-datasets/era-interim-land). GLEAM data are available over the 1980–2016 period at a monthly frequency and at 0.5° spatial resolution. GLEAM estimates global root zone soil moisture and evapotranspiration from a simple land surface model based on satellite forcing and soil moisture assimilation (Martens et al., 2017). The depth of the root zone in GLEAM is a function of land cover type: 0.1 m for bare soil, 1 m for low vegetation, and 2.5 m for tall vegetation. The ERA-I/Land product covers 1979 to 2010 at ~80-km resolution using the H-TESSEL land surface model (Balsamo et al., 2009) of the ECMWF driven by the ERA-Interim atmospheric reanalysis including precipitation adjustments based on monthly observations (Balsamo et al., 2015). ERA-I/Land soil water content is available for four soil depths down to 2.89 m. Both GLEAM and ERA-I/Land products have been aggregated to 1° resolution using conservative remapping from their native resolution.

Figure 9a presents the annual means of soil moisture at the global scale and their zonal averages estimated by a linear combination (arithmetic average) of both GLEAM and ERA-I/Land products, and simulated by *sfxcm5* and *sfxcm6*. This comparison is made over the period from 1980 to 2010. The soil water content is greatly increased from *sfxcm5_pgf* to *sfxcm6_pgf*. This drastic increase in soil moisture leads to a better agreement with GLEAM and ERA-I/Land estimates as highlighted by pattern skill scores and zonal averages. The spatial patterns of soil moisture in E2O forced simulations are similar to those of the PGF simulations (not shown). The zonal averages underline the fact that soil moisture simulations are more sensitive to the model physics than to the atmospheric forcing. A slight difference appears over northern high latitudes (above 60°N) where experiments using E2O forcing simulate a larger soil moisture than simulations using PGF

data. This difference is due to the larger precipitation rate in MSWEP-based E2O precipitation compared to GPCC-based PGF precipitation (Figure 3).

The interannual variability estimated by the standard deviation of the monthly detrended anomaly time series $\sigma_{ano,}$ (Figure 9b) appears larger over low vegetation areas characterized by shallow root depths than over dense forests or unvegetated areas. While this contrast is not clear in the older version of the model, it is well captured by the new model, as highlighted by pattern skill scores. This result is also not sensitive to atmospheric forcing because pattern skill scores for *sfxcm6_e2o* (ratio = 0.71, c-rmse = 0.0063, and r = 0.48) are quasi similar to *sfxcm6_pgf* but also largely better than those of *sfxcm5_e2o* (ratio = 0.88, c-rmse = 0.0061, and r = 0.55).

The main reason for these differences, especially the *sfxcm6* increase in soil moisture compared to *sfxcm5* (Figure 9a), can be traced to changes in the ISBA physics from ISBA$_{FR}$ to ISBA$_{DF}$ as shown by the comparison between *sfxcm5_pgf* and the additional *isbcm6_pgf* simulations (Figure 10, top). The dominant effect is linked to the change in soil moisture equilibrium state induced by the soil parameterization from a simple three-layer bucket scheme to a diffusive explicit scheme. The bucket layers were restored toward a too-low ISBA$_{FR}$ field capacity corresponding to a hydraulic conductivity of 0.1 mm/day (Appendix A), while the diffusive scheme reaches its equilibrium dynamically around a larger water content near its field capacity, corresponding, for example, to a matric potential of around −0.33 bar for pure mineral soils and −0.1 bar for pure peat soils (section 2.2). Second, the mixing between mineral and organic soil properties increases soil porosity (equation (7b)) and limits hydraulic conductivity, leading to very wet soil conditions, especially in boreal regions where SOC is very dense (Figure 2d). In these regions, a plug effect in permafrost areas due to the deep soil freezing (equation (6c)) also contributes to maintaining very moist soils all year.

The comparison between *isbcm6_pgf* and *gwcm6_pgf* (Figure 10, middle) indicates that the impact of upward capillarity fluxes on soil moisture from groundwater into the root zone is not negligible in some aquifer basins. Even though it represents an average annual increase of only 0.76% in soil moisture globally, this increase reaches 1.5% when considering only the CTRIP aquifer basins. Finally, adding inundated floodplain infiltration has a limited impact on soil moisture globally but can be nonnegligible locally, as shown by the comparison between *sfxcm6_pgf* and *gwcm6_pgf* (Figure 10). This is the case over the Parana basin, West Africa, and especially along the Nile River. The quantity of water that could potentially flood the Nile Valley is very large but is currently limited by dams for electric power generation and intensive irrigation. Because the model does not represent these processes, it simulates strong river flood events, as in ancient times, and significant soil infiltration.

6.2. Major Land Surface Fluxes
6.2.1. Evapotranspiration

We attempt to evaluate evapotranspiration against available global estimations such as the Multi-Tree Ensemble (MTE) product (https://climatedataguide.ucar.edu/climate-data/fluxnet-mte-multi-tree-ensemble), the Penman-Monteith-Leuning (PML) product, and the GLEAM product. MTE gives an estimate of global evapotranspiration at 0.5° spatial resolution over the 1982–2008 period at a monthly frequency derived from satellite data and FLUXNET in situ observations using a machine-learning algorithm (Jung et al., 2010). PML is an observation-driven model that estimates the monthly global evapotranspiration and its components at 0.5° spatial resolution over the 1981–2012 period (Zhang, Pena Arancibia, et al., 2016; Zhang, Peña-Arancibia, et al., 2016). We interpolate MTE, PML, and GLEAM evapotranspiration at 1° resolution using conservative remapping. The combination of these three products helps us to assess uncertainties in global evaporation estimates similarly to the 1989–2005 merged synthesis product of the LandFlux-EVAL diagnostic multidata set (Mueller et al., 2013) but over a longer period (1982–2008).

The comparison between *sfxcm5*, *sfxcm6*, MTE, PML, and GLEAM evapotranspiration (Figure 11) does not allow us to discriminate between the old and new versions of the model, even though the skill scores for *sfxcm6* are slightly better than for *sfxcm5*. All model versions show an acceptable agreement with MTE, PML, and GLEAM, though a systematic underestimation appears over Amazonian and African tropical forests. Simulations with ERA-Interim-based E2O forcing exhibit a larger evapotranspiration than simulations driven by PGF, as shown by the zonal averages. This is particularly visible over Europe and Eastern USA. An E2O precipitation rate larger than PGF in northern high latitudes and drier air humidity conditions (Figure 3) everywhere are the main causes of these differences. Larger solar and atmospheric downward
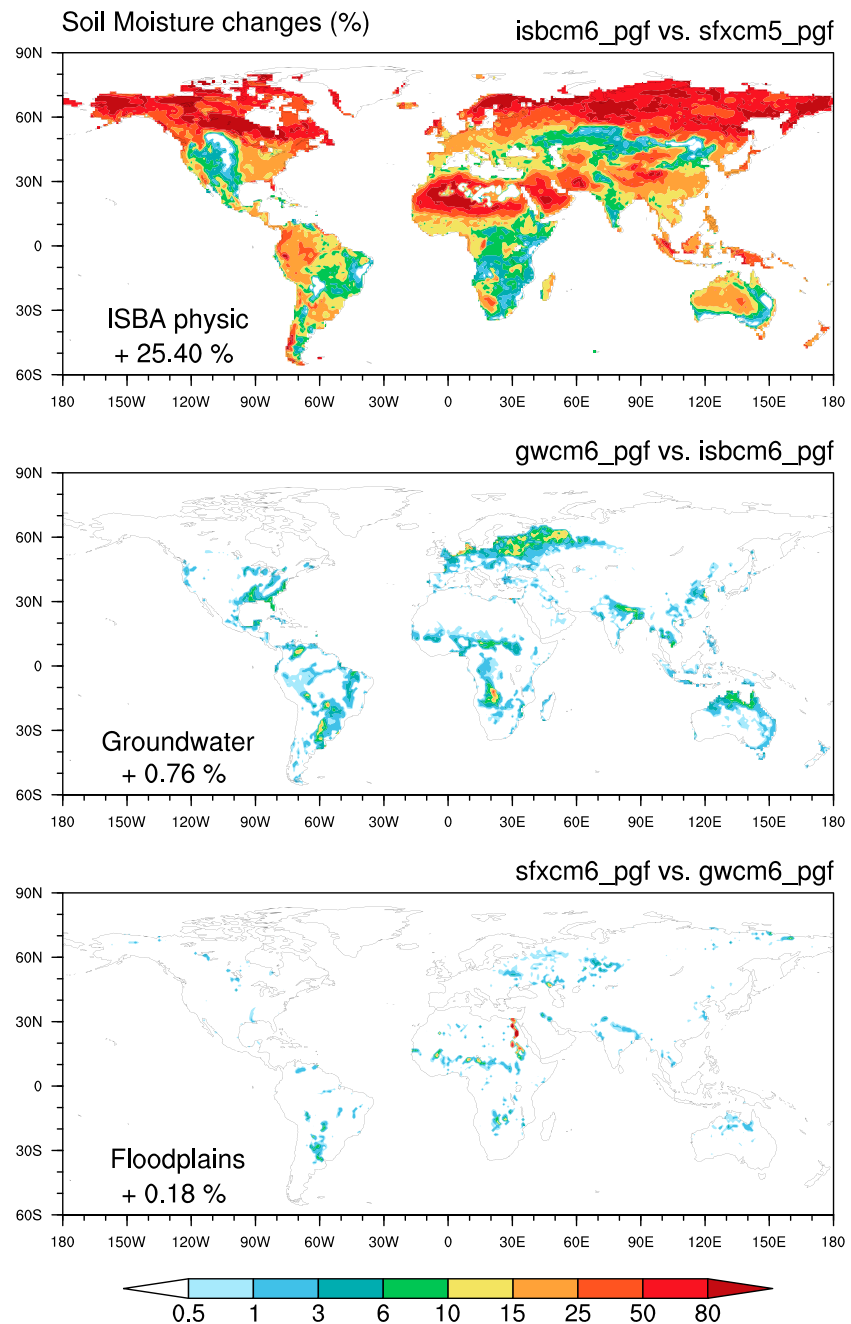
Figure 10. Annual mean impacts over the 1979–2010 period of the main physical changes on the simulated soil moisture expressed in %. ISBA physics (top panel) means all changes in soil/vegetation/snow from ISBA$_{FR}$ to ISBA$_{DF}$, Groundwater (center) and Floodplains (bottom) refer to effects of adding aquifer processes with upward capillarity fluxes and river flooding processes with free-water evaporation and soil reinfiltration, respectively. All experiments are summarized in Table 2.

radiations from the ERA-Interim reanalysis versus the PGF forcing over Europe and Western USA (Figure 3) also contribute to this larger E2O-induced evapotranspiration rate.

Figure 12 compares the observed and simulated mean seasonal cycles and detrended monthly anomalies time series over the northern high and middle latitudes and the tropics. Globally, all seasonal cycles are appreciably reproduced by all model versions despite the fact that, as observed in Figure 11, experiments based on E2O forcing simulate larger evapotranspiration rates than estimates, especially across the
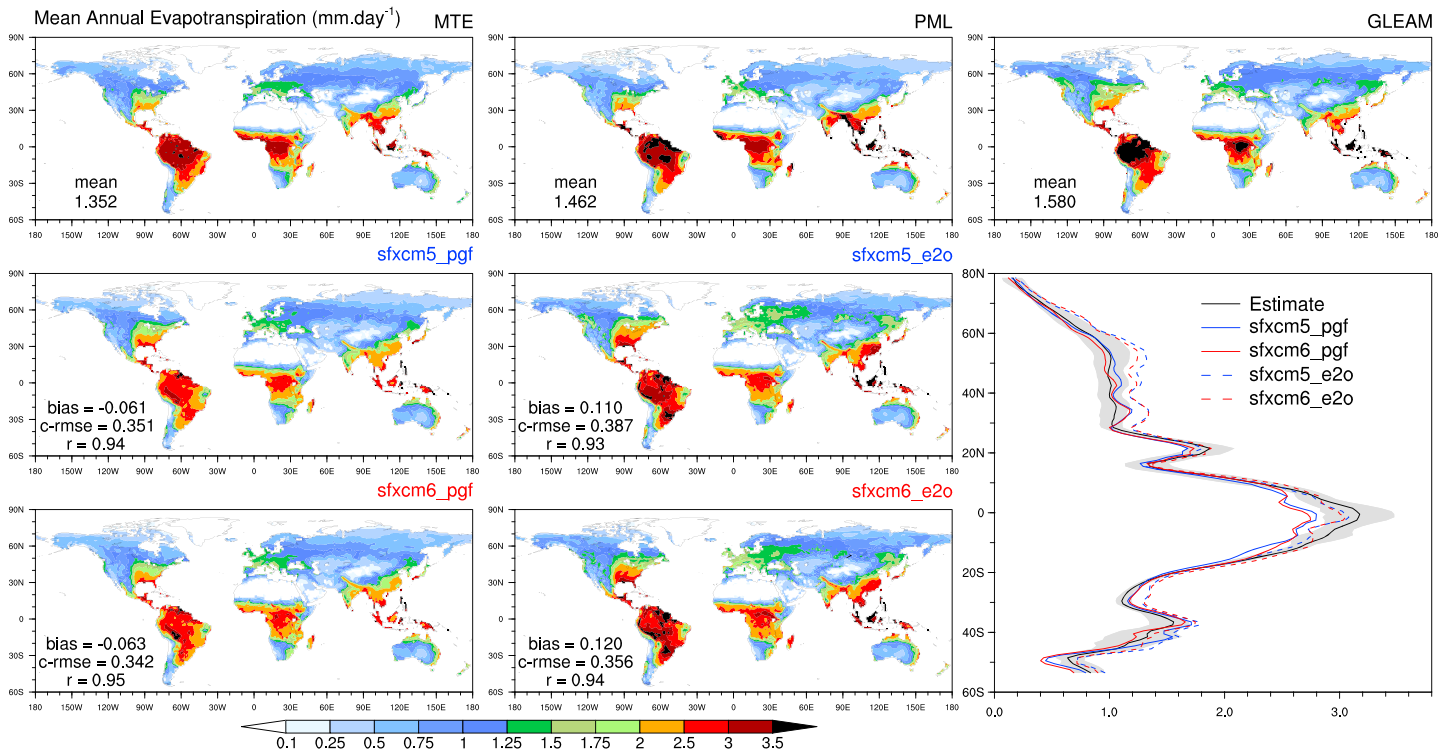
Figure 11. Comparison between observed and simulated annual mean evapotranspiration over the 1982–2008 period. Pattern skill scores are computed against the arithmetic average of the GLEAM, PML and MTE products. As in Figure 9, the gray shaded area around the zonal average of the MTE-PML-GLEAM combination estimate (black) corresponds to the minimum and maximum values between these products.

Northern Hemisphere. Inversely, evaporative fluxes simulated by PGF-based experiments are generally in the lower range of estimates. The interannual variability is also well reproduced, and monthly anomaly skill scores are clearly in favor of *sfxcm6* compared to *sfxcm5*, whatever the considered region. Over northern middle and high latitudes, monthly anomalies are significantly improved with *sfxcm6* compared to *sfxcm5*. In the tropics, the *sfxcm6* anomaly time series are always better correlated with estimates than *sfxcm5* and the root-mean-square errors are only slightly degraded due to the larger amplitudes of these anomalies.

Over northern high latitudes, the shape of the *sfxcm6* seasonal cycles is slightly improved compared to *sfxcm5*. The low evaporative rate during the winter season is better reproduced by *sfxcm6* compared to *sfxcm5* (Figure 12). From October to February, this rate is estimated at 0.019 mm/day by the combination of the MTE, the PML, and the GLEAM products. *sfxcm6_pgf* and *sfxcm6_e2o* reproduce a quasi-similar evaporation of about 0.023 and 0.061 mm/day, respectively, while *sfxcm5_pgf* and *sfxcm5_e2o* simulate a rate five times larger than estimates (0.1 and 0.13 mm/day, respectively). The cause is mainly linked to the very intensive snow sublimation simulated by *sfxcm5* (0.063 mm/day for *sfxcm5_pgf* and 0.075 mm/day for *sfxcm5_e2o*), while this rate becomes negligible with *sfxcm6*. During spring, *sfxcm6* simulates a lower evapotranspiration than *sfxcm5* for the same reasons (lower snow sublimation rates). During summer, this difference is reversed and the *sfxcm6* evaporative rate is larger than in *sfxcm5* due to wetter soil conditions (cf. section 5.1.3). Fewer differences between both model versions are found in northern midlatitudes, but the winter evaporation is also better reproduced by *sfxcm6* compared to *sfxcm5*. Over the tropics, *sfxcm6* evaporates at a slightly higher rate than *sfxcm5*.

This higher *sfxcm6* evaporative rate is equally due to the moistening effect of upward capillarity fluxes from groundwater into the soil and the direct evaporation of the floodplains (Figure 13). Groundwater effects on evapotranspiration are logically located in the regions where an increase in soil moisture was found in Figure 10: the tropics and to a lesser extent the southeastern USA, France, Benelux, and Eastern Europe. This increase is about 1.1% with the PGF forcing and is similar to the ~0.9% found by Vergnes et al. (2014)
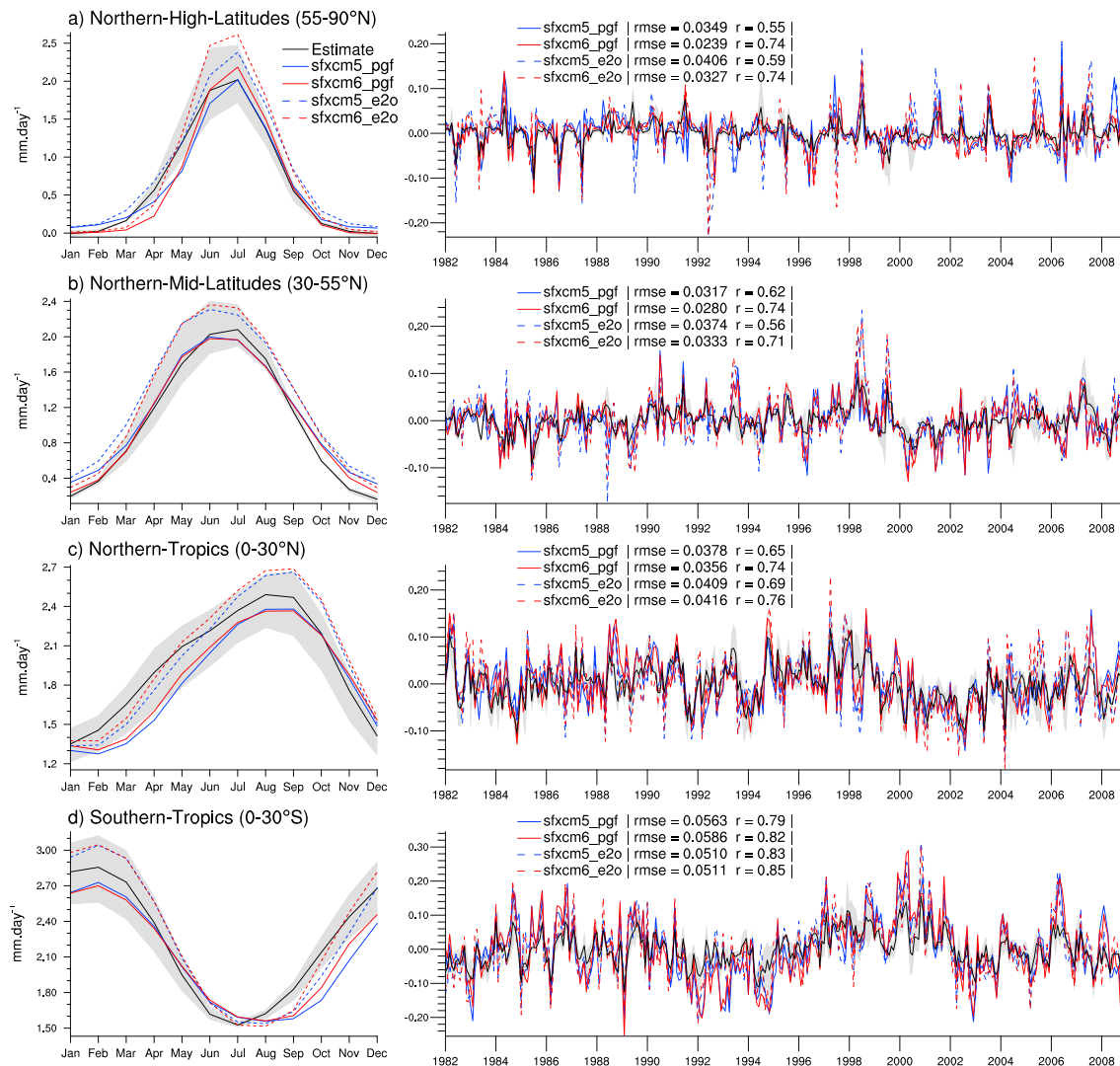
Figure 12. Comparison between observed and simulated monthly evapotranspiration over the 1982–2008 period. Mean seasonal cycles and detrended monthly anomalies time series averaged over the northern high and mid latitudes and the tropics are shown. In each panel, the black line corresponds to the MTE-PML-GLEAM combination estimate, and the gray shaded area to the minimum and maximum values between both products. The root mean square error (rmse) and the correlation (*r*) between observed and simulated anomalies are given.

over France. The floodplain effect is in the same range (~1.2% with PGF). It is also essentially located in the tropics and can be very strong locally in some parts of South America (e.g., the Amazon River and the Parana basins) and Africa (e.g., Sahel, Okavongo basin, and Nile River). In extratropical regions, floodplains play a role in the Ob basin and, to a lesser extent, in North America and Eastern Europe.

6.2.2. River Discharges

River discharges allow the water budget to be assessed over large areas and are an excellent validation test for land surface models, considering that the precipitation forcing is as perfect as possible. To perform such a comparison, we gathered a large set of daily discharge measurements at 20,164 stations from 1900 to present. These in situ measurements were provided primarily by the Global Runoff Data Centre (GRDC; http://www. bafg.de/GRDC/EN/Home/homepage_node.html), along with the USGS (http://waterdata.usgs.gov/nwis/ sw) over the United States, the HyBAm over the Amazon basin (http://www.ore-hybam.org), the French Hydro database (http://www.eaufrance.fr) over France, and the streamflow time series of the Parana river at Rosario from (Antico et al., 2018).

From this entire network, we selected 698 stations from 1979 to 2010 that meet four conditions: (1) only one station per TRIP grid cell; if several stations are located in the same grid cell, the one with a CTRIP drainage
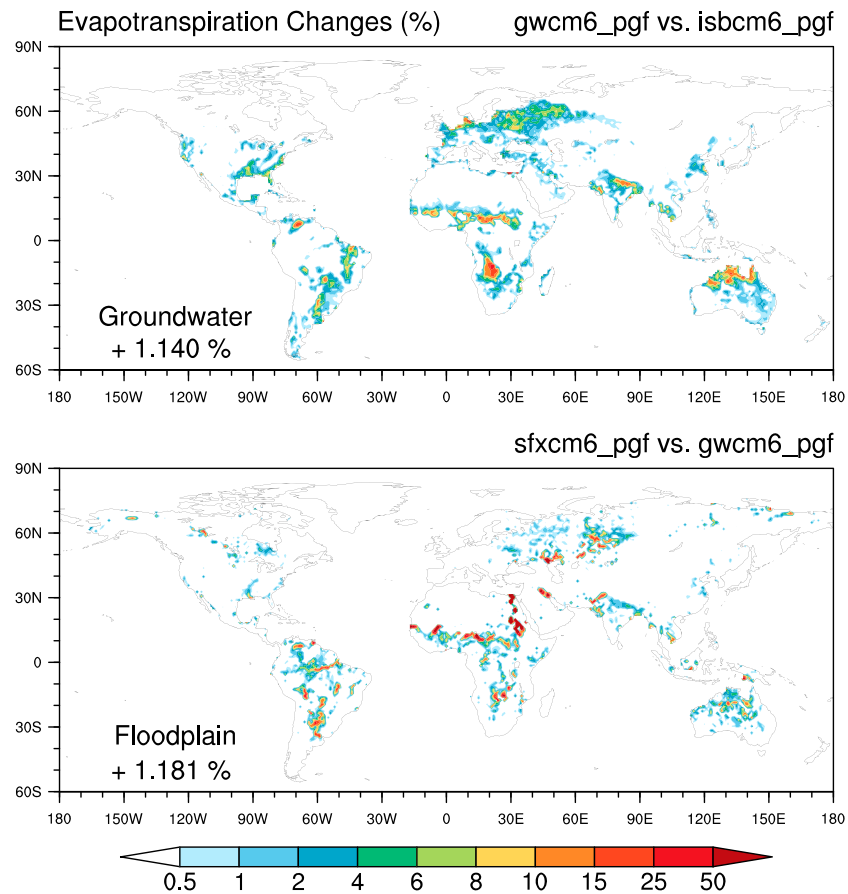
Figure 13. As in Figure 10, but for evapotranspiration and only for groundwater and floodplain effects.

area closest to the observed drainage area is kept; (2) observed upstream drainage areas must correspond to at least two atmospheric forcing grid cells at 1° (larger 24,000 km$^{2)}$; (3) stations where the error between observed and CTRIP drainage areas is larger than 15% are removed; and (4) daily measurements must cover at least 1,825 days (5 years) over the 1979–2010 period. To evaluate the simulated discharge, we use three skill scores widely used in hydrology: (1) the annual discharge ratio $R = \overline{Q_{sim}}/\overline{Q_{obs}}$ between the observed Q_{obs} and simulated Q_{sim} annual mean estimates the model's capacity to reproduce the mean annual streamflow water mass; (2) the daily Nash criterion, $N = 1 - \sum_{t=1}^{n}\left(Q_{sim,t} - Q_{obs,t}\right)^2 / \sum_{t=1}^{n}\left(Q_{obs,t} - \overline{Q_{obs}}\right)^2$, computed over all daily observations n, measures the ability of the model to capture the daily discharge dynamics (Nash & Sutcliffe, 1970); and (3) the root-mean-square error of the detrended daily discharge interannual anomalies, denoted hereafter as A.

The climatological seasonal cycles of daily discharges near the mouths of the world's largest river basins are shown in Figure 14 and their relative skill scores in Table 4. There are three boreal basins (Mackenzie, Ob, and Lena), three temperate basins (Mississippi and Danube), four tropical or subtropical basins (Amazon, Congo, Parana, and Orange), and three monsoon basins (Niger, Ganges, and Mekong).

Over boreal basins, the *sfxcm6* simulations reproduce the river base flow more accurately, leading to an increase in the simulated annual river discharge. The two main contributors of this base flow improvement are the new diffusive soil scheme (*isbcm6_pgf*) that explicitly simulates deep drainage without any soil moisture threshold limitation (equation (13)), and the new groundwater scheme (*gwcm6_pgf*) that restitutes the water stored during snowmelt to the river throughout the low flow season. This better simulated base flow is accompanied by a reduction in the largely overestimated summertime peak of discharge found in *sfxcm5_pgf*, *isbcm6_pgf*, and *gwcm6_pgf*. This reduction is mostly explained by the floodplain reservoir that induces a buffer effect on river discharge by storing a large part of the springtime snowmelt runoff, thereby
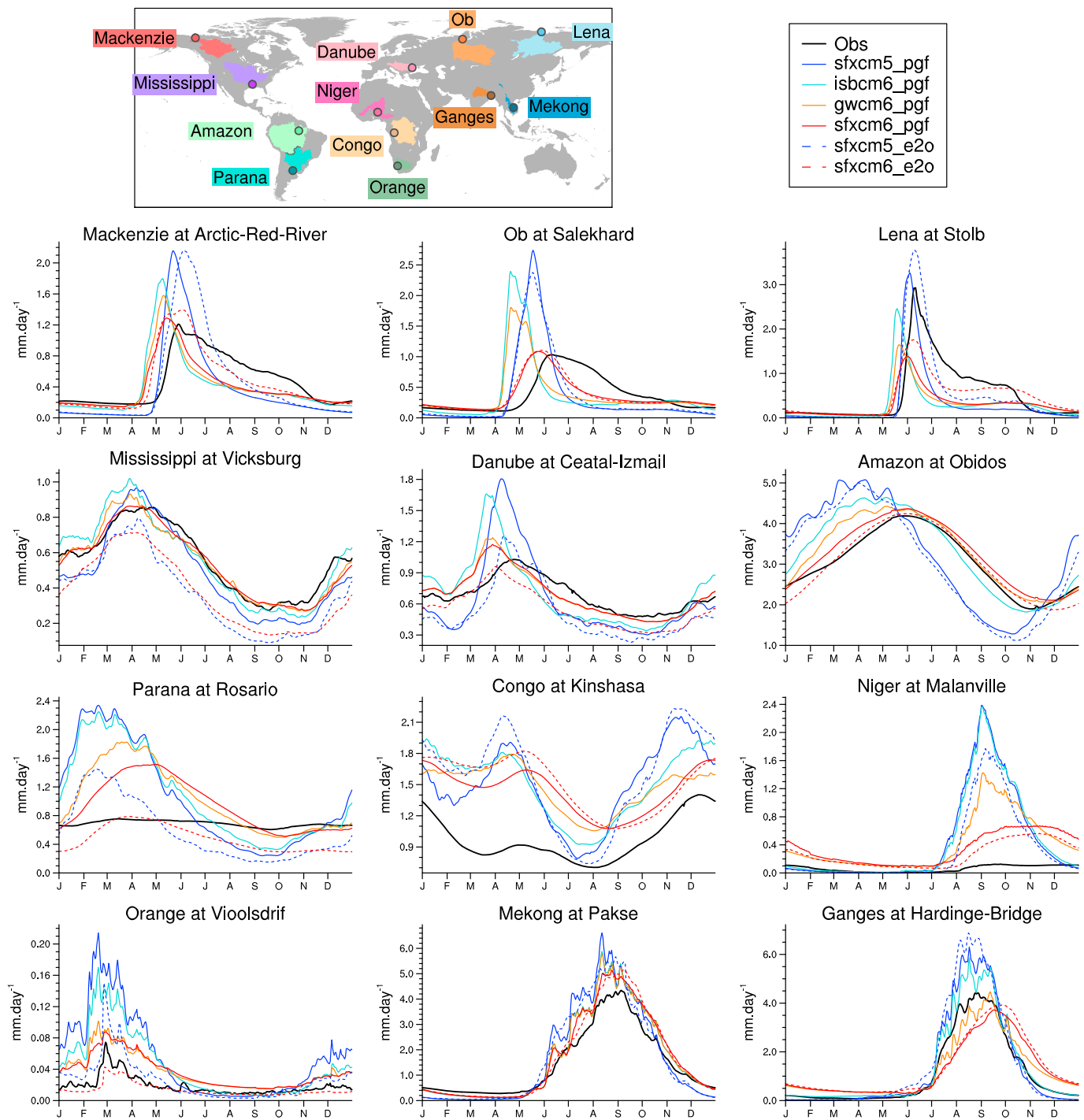
Figure 14. Comparison between the mean seasonal annual cycles (mm/day) of simulated and observed (black line) daily discharges near the outlet of the major basins of the world. The skill scores for each experiment are given in Table 4.

limiting the river streamflow velocity (Decharme et al., 2012). Over temperate basins, the same behavior can be observed with better simulations of the springtime peak of discharge and dry season base flow for *sfxcm6* compared to *sfxcm5*. The main drivers of these improvements are the same as in boreal basins (diffusive soil scheme, floodplains, and groundwater) with a dominant effect of groundwater contributing to delaying intense river discharges from the springtime rainy/snowmelt season to the dry season in summer and/or autumn. This result confirms the previous work of Vergnes et al. (2012) and Vergnes and Decharme (2012).

Table 4
River Discharge Skill Scores Simulated Near the Mouth of the Main Basins Shown in Figure 14 in Terms of Annual Ratio, Nash Criteria, and Daily Anomalies RSME (mm/day), Noted A-rmse

Basins	Criteria	Experiments					
		sfxcm5_pgf	isbcm6_pgf	gwcm6_pgf	sfxcm6_pgf	sfxcm5_e2o	sfxcm6_e2o
Mackenzie	*Ratio*	0.78	0.85	0.85	0.85	0.95	**0.97**
	Nash	−0.30	−0.74	−0.21	0.22	−0.14	**0.43**
	A-rmse	0.18	0.20	0.17	0.17	0.16	**0.14**
Ob	*Ratio*	0.91	**1.00**	**1.00**	0.94	0.96	0.96
	Nash	−3.35	−3.95	−2.09	**0.36**	−2.49	0.34
	A-rmse	0.37	0.39	0.31	**0.13**	0.31	**0.13**
Lena	*Ratio*	0.59	0.56	0.56	0.56	**0.89**	0.88
	Nash	0.26	−0.28	0.07	0.30	0.50	**0.64**
	A-rmse	0.32	0.36	0.31	0.27	0.32	**0.26**
Mississippi	*Ratio*	0.88	**1.01**	0.98	0.98	0.66	0.68
	Nash	0.59	0.56	0.69	**0.78**	0.31	0.39
	A-rmse	0.15	0.17	0.15	0.13	**0.12**	**0.12**
Danube	*Ratio*	0.93	1.03	**1.01**	**1.01**	0.74	0.80
	Nash	−1.04	−0.65	0.48	**0.57**	−0.13	0.37
	A-rmse	0.27	0.23	0.15	**0.13**	0.18	**0.13**
Amazon	*Ratio*	1.07	1.09	1.08	1.07	**1.00**	**1.00**
	Nash	−1.18	0.39	0.69	0.85	−0.94	**0.89**
	A-rmse	0.62	0.34	0.28	0.22	0.57	**0.21**
Parana	*Ratio*	1.53	1.56	1.48	1.38	**0.84**	0.70
	Nash	−48.32	−43.06	−21.76	−11.15	−14.50	**−3.82**
	A-rmse	0.49	0.49	0.32	0.20	0.31	**0.13**
Congo	*Ratio*	1.55	1.55	1.53	**1.49**	1.63	1.56
	Nash	−7.45	−6.05	−5.19	**−4.14**	−9.27	−5.97
	A-rmse	0.35	0.27	0.23	0.20	0.31	**0.17**
Niger	*Ratio*	7.53	7.53	6.83	5.53	5.56	**4.25**
	Nash	−264.88	−256.35	−118.80	−47.25	−148.24	**−25.56**
	A-rmse	0.27	0.29	0.20	0.07	0.22	**0.06**
Orange	*Ratio*	2.91	2.36	1.98	1.95	1.36	**0.74**
	Nash	−5.22	−2.74	−0.12	0.19	−0.62	**0.69**
	A-rmse	0.08	0.07	0.04	0.03	0.05	**0.02**
Mekong	*Ratio*	1.16	1.17	1.16	1.16	**1.15**	**1.15**
	Nash	0.17	0.45	0.47	0.67	0.51	**0.83**
	A-rmse	1.04	0.90	0.90	0.66	0.71	**0.35**
Ganges	*Ratio*	1.22	1.20	1.13	**1.11**	1.34	1.20
	Nash	0.40	0.50	**0.70**	0.67	0.55	0.63
	A-rmse	1.03	1.03	0.75	0.57	**0.56**	**0.56**

Over tropical, subtropical, and monsoon basins, discharge improvements are less obvious even though the Amazon, the Orange, and the Mekong rivers are strongly enhanced. River stream flows are generally less overestimated with *sfxcm6* compared to *sfxcm5* due to a larger evapotranspiration rate (Figure 12). The seasonal cycles are also more in phase with observations that can be equally related to the representation of floodplains and groundwater. However, over the Parana, although *sfxcm6* simulates a more reasonable river discharge than *sfxcm5*, the seasonal cycle remains too strong, which can be due to uncertainties in precipitation forcing and/or to the presence of dams. Over the Ganges River, the new model degrades the simulated seasonal cycle due to a groundwater-floodplain buffer effect, which is too strong. Nevertheless, *sfxcm6* Nash criteria remain larger than *sfxcm5*, especially because *sfxcm6* annual discharges and interannual variability are better reproduced. Over the Congo and the Niger basins, while *sfxcm6* seasonal cycles are closer to observations compared to *sfxcm5*, river stream flows remain strongly overestimated and limit Nash criteria. The Congo discharge may be too high due to uncertain precipitation but also to an underestimation of the tropical forest transpiration (Joetzjer et al., 2015), and of the direct evaporation of the canopy intercepted precipitation (Figure 8). For the Niger, the cause of the discharge overestimation is not simple to explore and should be multiplitous, as discussed in section 7.
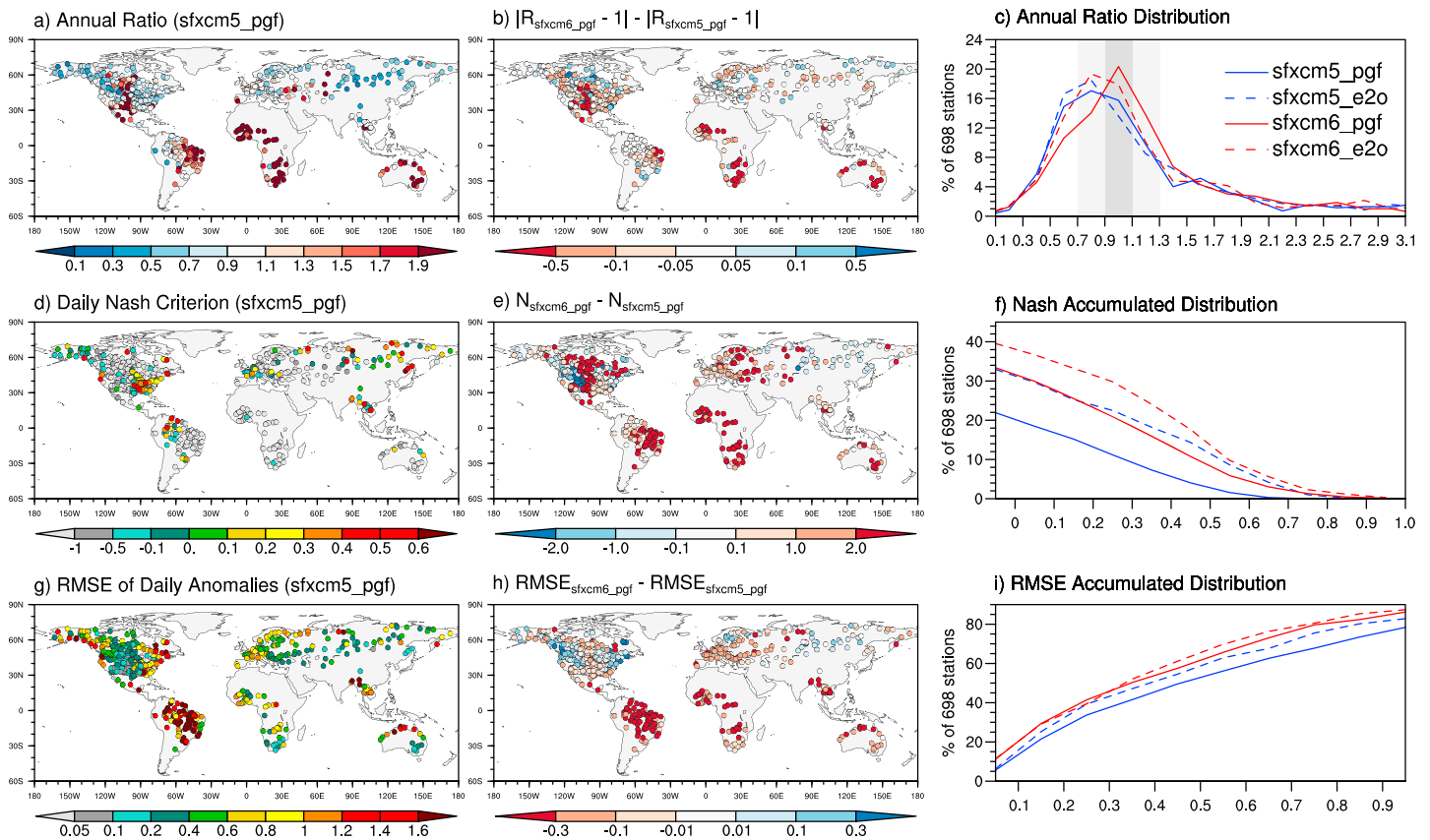
Figure 15. Comparison between observed and simulated daily river discharges over the 1979–2010 period. Left column: *sfxcm5_pgf* annual ratio (a), Nash criterion (d), and daily anomalies RSME (mm/day) (g). Middle column: difference with the *sfxcm6_pgf* annual ratio (b), Nash criterion (e), and daily anomalies RSME (h). Right column: distribution of annual ratio for each experiments (c), accumulated distributions of the Nash criteria (f), and daily anomalies RSME (i).

These results can be summarized in Figure 15 by the global comparison of the simulated discharge skill scores. The spatial distribution of the annual ratio difference $|R_{sfxcm6\_pgf} - 1| - |R_{sfxcm5\_pgf} - 1|$ in Figure 15b confirms that the new version limits the overestimation of river discharges over the tropics (30°S–30°N) and the underestimation elsewhere. Indeed, a negative value of this ratio difference means that the *sfxcm6_pgf* simulated discharge is closer to observations than the *sfxcm5_pgf*. This result is confirmed by the histogram of mean annual ratios in Figure 15c. Both *sfxcm6* distributions are more centered around the 0.9–1.1 annual ratio range. The spatial distribution of the difference in Nash criteria between *sfxcm5_pgf* and *sfxcm6_pgf* in Figure 15e confirms that the new version of the model improves the simulated daily discharge dynamics over the majority of the 698 gauging stations. These results are also confirmed by the cumulative distribution function of Nash criteria in Figure 15f, where *sfxcm6* Nash scores appear larger than *sfxcm5*. The river discharge interannual variability is generally improved by *sfxcm6_pgf*. The RMSE of the detrended daily anomalies (Figure 15h) is generally smaller with *sfxcm6_pgf* than with *sfxcm5_pgf*. These results are confirmed by the cumulative distributions of the daily interannual anomalies RMSE in Figure 15i.

These positive behaviors are observed whatever the atmospheric forcing, but simulations driven by the ERA-Interim-based E2O forcing perform generally better than using PGF data, except over temperate basins. In the Mississippi and Danube river basins; for instance, *sfxcm5_e2o* and *sfxcm6_e2o* exhibit a strong evapotranspiration rate (Figure 11), leading to an underestimation of the simulated discharge (Figure 14 and Table 4). Because many of the 698 gauging stations are located in northern temperate basins, improvements in annual ratio and daily Nash distributions are less clear when using E2O than PGF data (Figure 15). However, this larger evaporative rate also improves river discharge simulations in most tropical and monsoon basins, except in the Ganges river basin (Figure 14 and Table 4), where the improvement comes from the higher MSWEP-based E2O precipitation rate rather than the GPCC-based PGF rate. Over boreal

basins, a higher precipitation rate (Figure 3) together with a more accurate simulation of the snowpack (cf. section 4) induces generally better river discharge skill scores with the E2O forcing.

6.3. Terrestrial Water Storage Variations

All improvements in simulating floodplains, groundwater, soil moisture, evapotranspiration, and river discharge should appear in the simulation of Terrestrial Water Storage time variations (ΔTWS). Indeed, ΔTWS integrates all changes in continental water masses because it is defined from the hydrological water balance equation as the difference between input water flux (total precipitation) and output water flux (the sum of evapotranspiration and river discharges). The ΔTWS corresponds to variations of all reservoirs simulated by a land surface model. In *sfxcm5*, ΔTWS is the sum of variations in snowpack, canopy water, total soil moisture, and river water mass, while in *sfxcm6* floodplains and groundwater storage are added.

Only monthly ΔTWS are observed at the global scale via GRACE gravity products (Swenson, 2012). In this study we used three solutions of the RL05 GRACE release provided at 1° resolution by the Center for Space Research (CSR) at the University of Texas at Austin, the Jet Propulsion Laboratory (JPL), and the GeoForschungsZentrum (GFZ) at Potsdam. They estimate ΔTWS from 2002 to the present from a highly accurate map of the Earth's gravity field at a resolution of about 300 km using a Gaussian filter in order to remove noise and errors in the gravity field measurements (Landerer & Swenson, 2012; Swenson & Wahr, 2006). For comparison, as in the previous study (Alkama et al., 2010; Vergnes & Decharme, 2012), the simulated ΔTWS were also smoothed using a similar 300-km width Gaussian filter.

While all the simulated seasonal spatial patterns appear in good agreement with those estimated by GRACE, *sfxcm6* significantly improves the spatial skill score compared to *sfxcm5* (Figure 16). This improvement is clearly confirmed by the comparison of all seasonal zonal averages and their respective centered root-mean-square error skill scores. The causes of these improvements are studied in Figure 17 using seasonal cycles and detrended monthly anomalies averaged over northern high and middle latitudes, as well as over the tropics. As shown by the zonal averages (Figure 16), the most important impact of the new model can be seen over the tropics. The main contributors are the new diffusive soil scheme (*isbcm6_pgf*), followed by the groundwater scheme, (*gwcm6_pgf*), which successively enhances simulated seasonal cycles, monthly anomalies and their associated skill scores. These two processes increase the memory of the system and thus shift simulated ΔTWS toward estimates. The buffer effect of floodplains is more limited but also has a positive impact on simulated seasonal cycles. Over northern midlatitudes, the changes in the physics from ISBA$_{FR}$ to ISBA$_{DF}$ (*sfxcm5_pgf* versus *isbscm6_pgf*) have a mixed impact because they slightly degrade the simulation of the seasonal cycle as well as the skill scores of the actual time series (c-rmse and r). This weakness can be related to the too early springtime snowmelt discussed in section 4. However, changes in ISBA physics greatly improved the simulation of the ΔTWS interannual variability principally related to progress in simulating soil moisture monthly anomalies (Figure 9). While floodplains have a limited effect on simulated midlatitude ΔTWS, groundwater processes (*gwcm6_pgf*) have a positive impact on the simulated seasonal cycle and especially on the actual signal skill scores (c-rmse and r). This is also the case for simulated interannual variability (rmse$_{ano}$ and r$_{ano}$).

7. Discussion and Conclusions

The recent changes in the physics of the ISBA$_{DF}$-CTRIP land surface system for use in global hydrological applications and in the family of climate models developed at the CNRM represent a significant effort to update snow and soil physics, and to account for groundwater and floodplain processes. This new version represents a significant advance compared to the previous ISBA$_{FR}$-TRIP version (Decharme & Douville, 2007). The new system has been evaluated in off-line mode using a large set of observations or estimates, along with two different atmospheric forcings to avoid uncertainties in the land surface response to one specific atmospheric forcing. While it is not our goal to rank atmospheric forcings, it must be noted that simulations using ERA-Interim-based E2O forcing induce globally better results than the NCEP-NCAR-based PGF forcing in terms of snow, permafrost, and river discharge scores, as well as in the interannual variability of almost all studied variables. However, an excessively strong evaporative demand over the USA and Europe with E2O tends to degrade hydrological simulations, at least over the Mississippi and the Danube basins. This underlines the importance of performing the evaluation of land surface models using several atmospheric forcings.
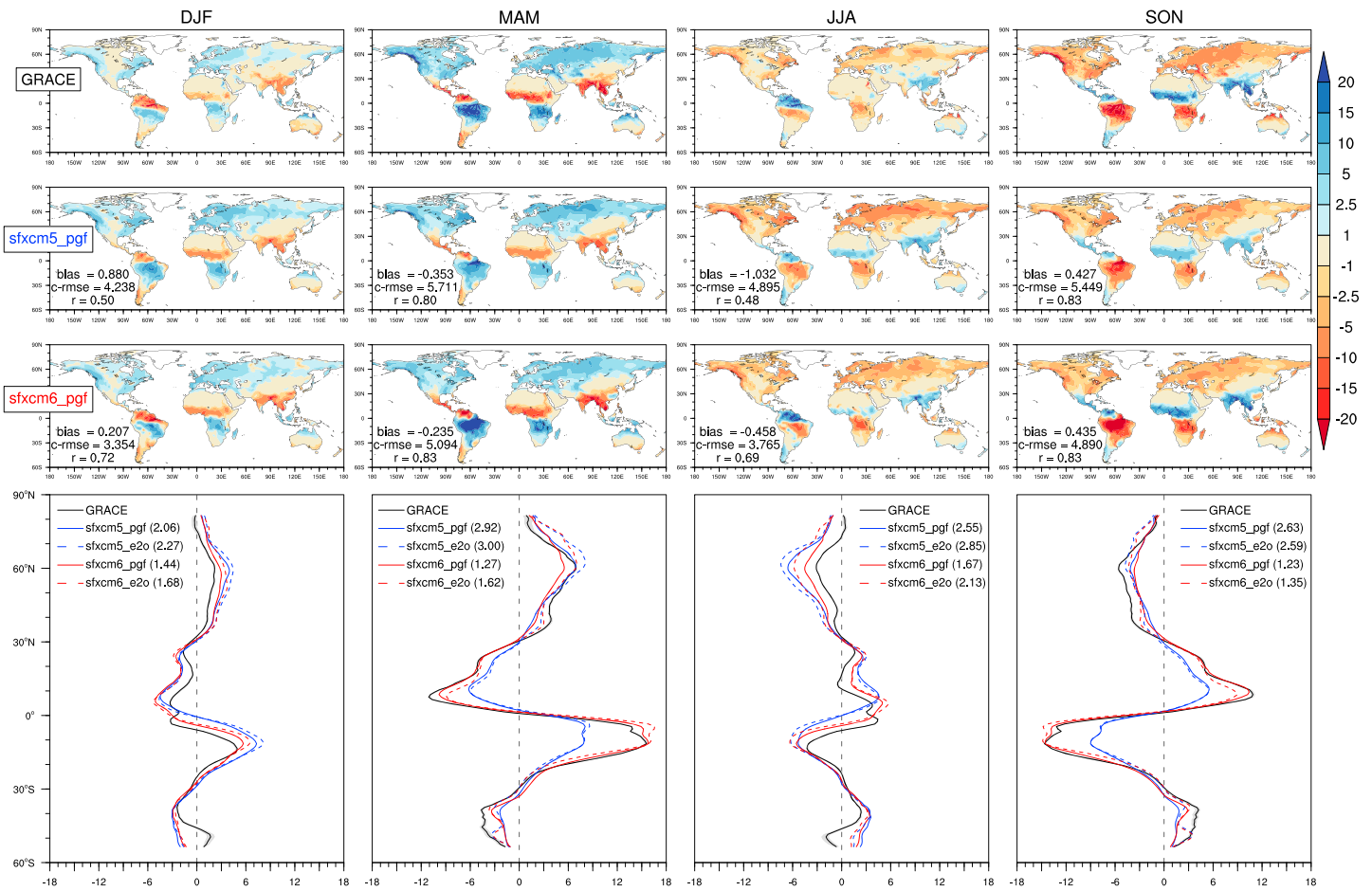
Figure 16. Seasonal ΔTWS estimated by GRACE from 2002 to 2010 and simulated by *sfxcm5_pgf* and *sfxcm6_pgf*. Top panels: spatial distribution. Bottom panels: zonal averages with the gray shaded area corresponding to the minimum and maximum values of the ensemble of three GRACE solutions (JPL, GFZ, and CSR).

In terms of Northern Hemisphere cold processes, the representation of the snowpack is clearly improved by the new ISBA$_{DF}$-CTRIP system, especially the snow cover extent and the snow depth, but also snow seasonality and interannual variability, which confirms our previous work over Northern Eurasia alone (Decharme et al., 2016). As discussed in Decharme et al. (2016), an adequate simulation of snow layering and snow compaction/densification is the main cause of the good simulation of winter snow, while snow albedo is an important driver of the springtime melting timing, at least over vegetation-free areas. This robust representation of snow together with a detailed representation of soil thermal processes leads to an accurate simulation of the extent of permafrost and the active layer depth. As discussed in many studies (Bonan & Shugart, 1989; Dankers et al., 2011; Decharme et al., 2016; Lawrence & Slater, 2008; Paquin & Sushama, 2014), it is of primary importance to account for soil organic carbon when computing soil hydraulic and thermal properties (section 2.2.5) to simulate the summer soil temperature profile at high latitudes, as well as the depth and the spatial distribution of the permafrost active layer. Finally, the major weakness of the new ISBA$_{DF}$-CTRIP system in terms of snow remains the too early springtime snowmelt above 50°N, where boreal forest is present. This implies a too early springtime peak of river discharge over all Arctic basins. As discussed in section 4.1, the main explanation is that ISBA$_{DF}$ does not solve an independent energy budget for vegetation able to interact with the snow and decrease the incident radiation reaching the snowpack, delaying the snowmelt later in the season. This problem will be resolved in the near future by the use of the new ISBA Multi Energy Budget scheme (Boone et al., 2017), which solves distinct energy budgets for the soil, the snow, and the vegetation representing the only way to simulate the snowpack beneath forests in a robust and physically consistent manner.
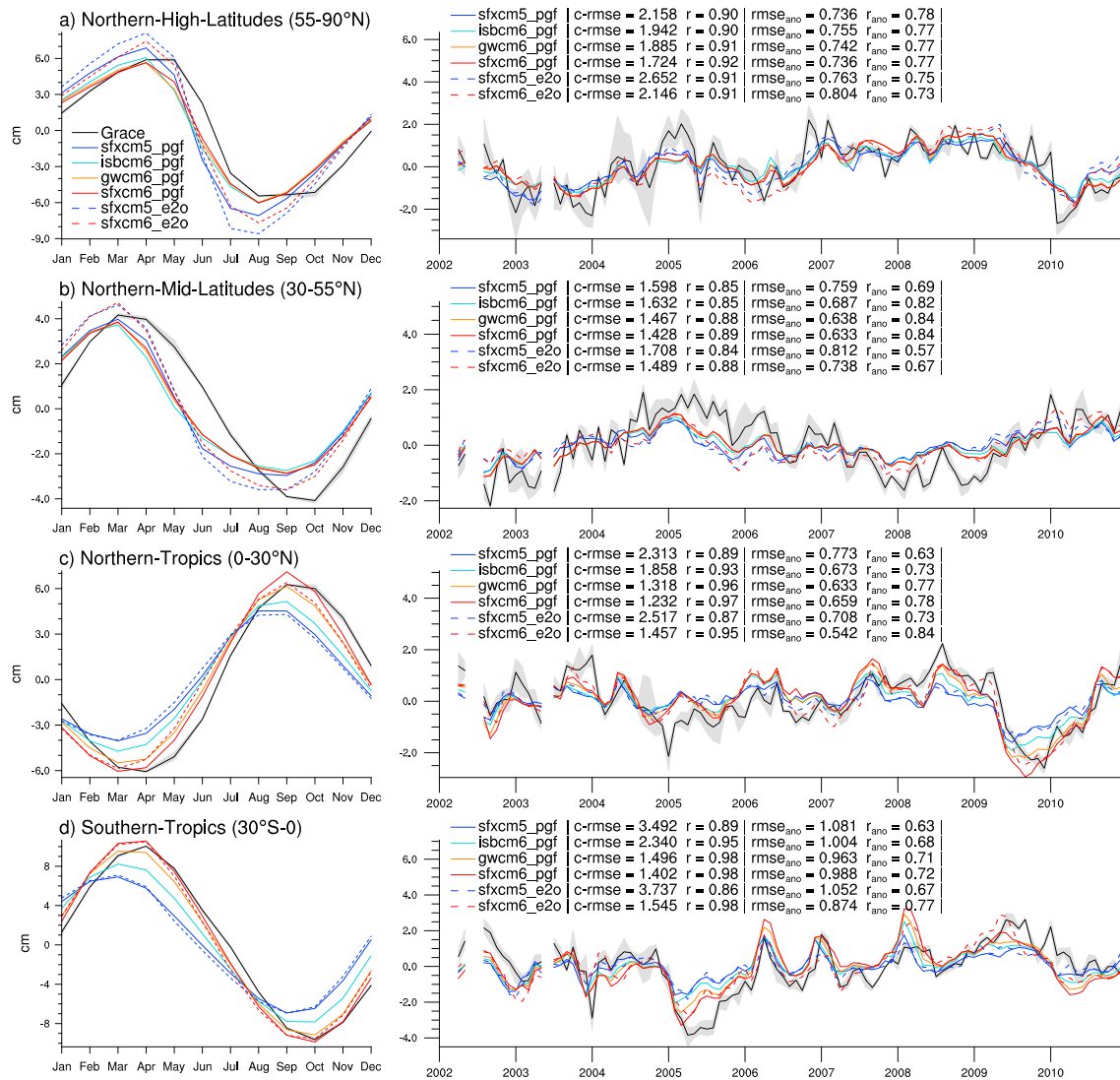
Figure 17. Observed and simulated monthly ΔTWS over the 2002–2010 period. Mean seasonal cycles (left column) and detrended monthly anomaly time series (right column) averaged over the northern high and mid latitudes and the tropics. Centered root-mean-square error (c-rmse in cm) and correlation (r) are computed for the actual TWS time series. Root-mean-square error ($rmse_{ano}$ in cm) and correlation are calculated for their monthly anomalies (r_{ano}).

In terms of the global water budget, the representation of the major land surface water reservoirs in the new ISBA$_{DF}$-CTRIP system is largely encouraging. Changes in ISBA physics from a simple bucket force-restore scheme to a multilayer diffusive soil accounting for the mixing between mineral and organic soil properties lead to a larger simulated soil moisture closer to the GLEAM and ERA-I/Land products. The global distribution of the simulated floodplains is consistent with the satellite estimate from Prigent et al. (2007), even though the simulated flooded areas appear largely underestimated. Satellite retrieval algorithms possibly overestimate the reality, but some model parameterizations are uncertain, such as the subgrid relationship between the flooded water mass and the floodplain grid cell fraction (Decharme et al., 2012). The model's performance in simulating river discharge and/or variations in terrestrial water storage indicates that the groundwater processes and the dynamics of water in the floodplains are well reproduced.

The global land surface evapotranspiration is globally well reproduced by all model versions used in this study, and the simulated evapotranspiration is much more sensitive to the atmospheric forcing than to the model physics due to the level of the atmospheric demand. However, the ISBA$_{DF}$-CTRIP system presents slightly better scores than the previous model, especially the interannual variability indicating

a better representation of the dynamics of land surface evaporative processes. Nevertheless, a general weakness appears over tropical forests with a large underestimated evapotranspiration leading to overestimated river discharge. The transpiration scheme should certainly be improved over these regions, as underlined by Joetzjer et al. (2015), but a possible underestimation of the direct evaporation from the canopy reservoir cannot be excluded. Finally, the impact of the new water reservoirs (floodplain and groundwater) on the land-surface evapotranspiration appears small but not negligible. It would be very interesting to study this impact on the simulated climate and its sensitivity to global warming in the near future.

The new ISBA$_{DF}$-CTRIP system significantly improves the simulated river discharges in the major river basins of the world and more generally enhances the simulated global variation in terrestrial water storage as estimated by GRACE. This result is particularly important because such simulations of river discharges and/or of variations in terrestrial water storage are especially relevant in evaluating changes in model physics. Indeed, they integrate all qualities and weaknesses of the simulated water budget over large regions. The improvement in simulated river discharge can be summarized by a better simulation of both the annual peak of discharge and the base flow during the dry season. The simulated mean seasonal cycle and the interannual variability of the terrestrial water storage variations is also significantly improved, especially in the tropics. The main drivers of these improvements are equally distributed between diffusive soil scheme, groundwater, and floodplains processes. Of course, imperfections remain and future ways to improve the hydrology of ISBA$_{DF}$-CTRIP can be addressed. Anthropogenic processes should be included because manmade irrigation and/or dams can alter the river flow and increase the continental evapotranspiration (Sacks et al., 2009). It appears to be very important to increase the CTRIP resolution to a few kilometers to better reproduce the groundwater dynamics and their exchanges with the root zone without subgrid considerations.

ISBA$_{DF}$-CTRIP still simulates a too early springtime peak of discharge over boreal and temperate basins (Figure 14), which may be due to the early snowmelt simulated by the new scheme (cf. section 5.1). The use of the ISBA Multi Energy Budget scheme appears to be the only way to suppress this weakness. Another weakness in boreal regions is that the infiltrated water simulated by ISBA$_{DF}$-CTRIP is stored mostly in the soil, as shown by the high soil moisture content over high latitudes in *sfxcm6* experiments (Figure 9), leading to a general underestimation of river discharges (Figures 14 and 15). It is well known that due to the deep permafrost freezing, the active layer can act as a very shallow perched aquifer that controls lateral soil-river water exchanges during springtime snowmelt and summertime rainy seasons (Koch et al., 2013; Walvoord & Kurylyk, 2016; Woo, 1986). The lateral subsurface runoff from the subgrid topography simulated in the top soil of ISBA$_{DF}$ (Decharme et al., 2013) appears to not be efficient enough over permafrost regions to represent this large transfer of water from the soil to the river. Improving this lateral flow to prevent overly wet soils during summer and to increase river discharge over boreal basins will be very important. Over mountainous regions, the river dynamics are drastically impacted by the quantity and timing of the snowmelt, which are mainly correlated to changes in air temperature and incoming solar radiation (Lundquist et al., 2004). So in order to simulate mountainous basins accurately, snowpack simulations must be performed over several elevation bands to account for the topography-induced large gradient in air temperature (Jia et al., 2006; Lafaysse et al., 2011; Nijssen et al., 2001).

West African river discharges, and especially the Niger basin, are poorly simulated by ISBA$_{DF}$-CTRIP (Figures 14 and 15). The Niger basin has a very complex hydrodynamic structure with many endorheic subbasins in the north that do not contribute to the river flow due to a weakly connected drainage network and aridity. In addition, a large inner delta favors an intensive evaporation loss and an important aquifer recharge leading to approximately 60% of the inflow lost in the delta (Casse et al., 2015). While our model seems able to simulate a large inundation in the inner delta (Figure 7) together with strong soil reinfiltration (Figure 10) and large direct reevaporation from floodwater (Figure 13), these processes are not represented with enough detail in ISBA$_{DF}$-CTRIP to allow a realistic simulation of the Niger basin. However, the main cause is certainly the nonrepresentation of endorheic subbasins in the north of the basin and/or the presence of deep aquifers that can be relatively uncoupled from the river network. Accounting for such processes could contribute to improve the simulation of river discharges and the water budget in these regions (Pedinotti et al., 2012).

Finally, this study increases our confidence that the new $ISBA_{DF}$-CTRIP land surface scheme is able to represent the natural physical processes consistently over all continents, and will therefore be an interesting tool in the near future to address several scientific issues using off-line or in-line applications. A robust representation of northern snow is necessary to bring our contribution to the understanding of the polar warming amplification in the Arctic. The model's performance in representing permafrost characteristics and the continental part of the hydrological cycle in boreal regions allows us to address the relative role of soil moisture conditions in carbon release by permafrost soils affected by Arctic warming compared to the increase in temperature alone (Chadburn et al., 2017; Knoblauch et al., 2018). The introduction of groundwater and floodplains in our large-scale off-line hydrological simulations will make it easier for us to contribute to scientific and societal efforts in the understanding of some processes impacted by global warming such as (1) the localization and quantification of the increase in drought (Naumann et al., 2018) and river flood risk (Alfieri et al., 2017) event frequency in the future and (2) the management of global water resources in the context of groundwater depletion (Dalin et al., 2017). In addition, the use of groundwater and floodplain processes in our climate model brings a significant new degree of freedom that permits a more realistic hydrological response to the present and future climate. Conversely, we will be able to study the impacts of these processes on the climate, its present mean state, its variability, its predictability, and its sensitivity to global warming.

Appendix A: $ISBA_{FR}$ Force-Restore Scheme in CNRM-CM5

The $ISBA_{FR}$ land surface energy budget is essentially based on a single soil-vegetation-snow composite approach using a two pseudolayer temperature scheme (Noilhan & Planton, 1989). The surface composite temperature T_1 (K) is restored toward a subsurface temperature T_2 (K), defined as its mean value over 1 day. Because a larger soil thermal inertia must be considered for climatic runs, two additional subsurface temperatures, T_3 and T_4, have been added as follows:

$$\left|\begin{array}{l} \frac{\partial T_1}{\partial t} = C_T\left(SW_{net} + LW_{net} - H - LE + L_f Q_{fz,1} - L_f Q_{sm}\right) - \frac{1}{s_1}G_2 \\[2mm] \frac{\partial T_2}{\partial t} = \frac{1}{s_2}(G_2 - G_3) + C_{soil}L_f Q_{fz,2} \\[2mm] \frac{\partial T_i}{\partial t} = \frac{1}{s_i}(G_i - G_{i+1}) \quad \forall i = 3, 4 \\[2mm] G_i = \frac{1}{(s_{i-1} + s_i)\tau_{day}}\frac{2\pi}{}(T_{i-1} - T_i) \end{array}\right. \tag{A1}$$

where G_i (K/s) is the force-restore thermal flux, τ_{day} (s) is a time relaxation of 1 day, s_i a dimensionless pulsation length set to 0.5, 1.5, 4.5, and 13.5 for each of the four pseudolayer, i. SW_{net} (W/m^2) and LW_{net} (W/m^2) are the shortwave and longwave net radiation at the surface, H (W/m^2) the sensible heat flux, LE (W/m^2) the latent heat flux, L_f (3.337 × 105 J/kg) the latent heat of fusion, Q_{fz_1} and Q_{fz_2} (kg · m^{-2} · s^{-1}) the surface and subsurface soil freezing/thawing fluxes, Q_{sm} (kg · m^{-2} · s^{-1}) the snowmelt, and C_T (K · m^{-2} · J^{-1}) the surface composite thermal inertia coefficient. This coefficient is parameterized as the harmonic mean of the soil C_{soil} (K · m^{-2} · J^{-1}), the vegetation and the snow thermal inertia coefficients weighted by the vegetation and the snow grid cell fractions (Douville et al., 1995; Noilhan & Planton, 1989). The snow fraction is defined as for $ISBA_{DF}$ (equation 3) except that the snow fraction covering the bare ground, p_{sn_g}, is computed as follows:

$$p_{sn_g} = \frac{W_{sn}}{W_{sn} + 10} \tag{A2}$$

where W_{sn} (kg/m^2) is the snow water equivalent reservoir.

The snowpack is represented by a simple one-layer snow scheme (Douville et al., 1995). The snow temperature is approximated as the sum of T_1 and T_2 weighted by the vegetation fraction of the grid cell to account for a larger snowmelt inertia in the presence of vegetation. The snowmelt occurs if this empirical snow temperature is superior to the freezing point. The snow density is considered as a prognostic variable that increases exponentially with time from a minimum value ρ_{snmin} of 100 kg/m^3 to a

maximum value ρ_{snmax} of 300 kg/m^3. In the same manner, the snow albedo is also treated as a prognostic variable because it significantly impacts the land surface radiative balance. It decreases exponentially or linearly with time, depending on whether the snow is melting or not, from its fresh snow value of 0.85 to its aged snow value of 0.5. Note that a minimum value is set to 0.8 over ice sheets to avoid unrealistically small snow albedo over Greenland and Antarctica. As for the new scheme, a simple ice sheet runoff is also removed from the snow reservoir to avoid unrealistic snow accumulation over continental glacier (Appendix C).

ISBA$_{FR}$ has a three-layer soil hydrology (Boone et al., 1999). The depth or thickness of the roots, Δz_2 (m), defines the root zone reservoir, w_2 (m^3.m^{-3}), that overlaps the surface pseudo reservoir, w_1 (m^3/m^3), having an uniform thickness, Δz_1 (m), of 0.01 m, whereas for some land cover types a deep soil thickness under the roots, Δz_3 (m), is added to simulate a deep-soil reservoir, w_3 (m^3/m^3), as shown in Table 1. Thus, the governing equation for soil moisture are given by

$$
\left|
\begin{aligned}
\frac{\partial w_1}{\partial t} &= \frac{C_1}{\rho_w \Delta z_1}(I_r - E_g - Q_{fz_1}) - \frac{C_2}{\tau_{day}}(w_1 - w_{eq}) \\
\frac{\partial w_2}{\partial t} &= \frac{1}{\rho_w \Delta z_2}(I_r - E_g - E_{tr} - Q_{fz_1} - Q_{fz_2}) - \frac{C_3}{\tau_{day}\Delta z_2}\max(0, w_2 - w_{fc}) + \frac{C_4}{\tau_{day}}(w_2 - w_3) \\
\frac{\partial w_3}{\partial t} &= \frac{\Delta z_2}{\Delta z_3}\left[\frac{C_3}{\tau_{day}\Delta z_2}\max(0, w_2 - w_{fc}) - \frac{C_4}{\tau_{day}}(w_2 - w_3)\right] - \frac{Q_{sb}}{\rho_w \Delta z_3}
\end{aligned}
\right.
\tag{A3}
$$

where w_{eq} (m^3/m^3) is an equilibrium volumetric water content at the balance between the gravity and capillarity forces computed as a function of soil texture, soil ice content, and volumetric water content of the rooting layer. C_1 is the dimensionless soil transfer coefficients for moisture between the surface and the atmosphere. The dimensionless force-restore transfer coefficient C_2 characterizes the velocity at which the top soil water profile is restored toward w_{eq}. C_4 is the dimensionless diffusion force-restore coefficient between the root zone and the deep soil. C_3 (m) is a drainage coefficient that can be analytically related to the soil saturated hydraulic conductivity (Mahfouf & Noilhan, 1996). It characterizes the velocity at which the deep-soil reservoir is restored toward the water content at field capacity, w_{fc} (m^3/m^3). The subsurface runoff, Q_{sb} (kg · m^{-2} · s^{-1}), at the base of the soil is then computed as follows:

$$
Q_{sb} = \frac{\rho_w C_3}{\tau_{day}}\max(0, w_3 - w_{fc})
\tag{A4}
$$

All the C_1, C_2, C_3, and C_4 coefficients are related to soil textural properties and moisture using the Noilhan and Lacarrere (1995) continuous relationships adapted to account for soil ice (Boone et al., 2000) and for an exponential profile of the saturated hydraulic conductivity with soil depth (Decharme et al., 2006). In equation (A3), E_g (kg · m^{-2} · s^{-1}) is the bare soil evaporation that depends on surface soil moisture conditions and becomes potential when the superficial water content exceeds the water content at field capacity (Mahfouf & Noilhan, 1991). E_{tr} (kg · m^{-2} · s^{-1}) is the Jarvis-type plant transpiration that stops when the water content in the root zone is below the wilting point corresponding to a matric potential of −15 bar. I_r (kg · m^{-2} · s^{-1}) is the soil infiltration rate computed as the difference between the through-fall rate and the surface runoff. The through-fall rate is the sum of the rainfall not intercepted by the canopy, the dripping from the interception reservoir and the snowmelt from the snow pack.

Finally, ISBA$_{FR}$ has only a two-layer soil freezing scheme (Boone et al., 2000) embedded in the previous three-layer soil hydrology in which the first soil ice reservoir, w_{fz1} (m^3/m^3), is included in the root zone soil ice reservoir, w_{fz2} (m^3/m^3), as follows:

$$
\frac{\partial w_{fz1}}{\partial t} = \frac{Q_{fz_1} - S_{fz}}{\rho_w \Delta z_1} \quad \text{and} \quad \frac{\partial w_{fz2}}{\partial t} = \frac{Q_{fz_2} + Q_{fz_1}}{\rho_w \Delta z_2}
\tag{A5}
$$

where S_{fz} (kg · m^{-2} · s^{-1}) is the bare soil ice sublimation. Note that the root zone freezing is limited to a maximum threshold defined as the maximum depth to which the effects of the subsurface temperature extend. This depth represents the soil penetration of the diurnal cycle of the temperature, which is generally ranked from 15- to 35-cm depth, depending on soil textures and moisture (Boone et al., 2000).

Appendix B: The CNRM-CM6's ISBA$_{DF}$ Composite Soil-Vegetation-Flood Surface Temperature

The composite soil-vegetation-flood surface temperature is computed considering soil freezing and the one-dimensional Fourier law (equation (10)) for heat transfer into the soil. As superior boundary conditions, it uses classical surface/atmosphere energy budget over the snow-free part of the grid cell and the energy leaving the snowpack elsewhere. So variation in this snow-free land surface temperature can be written as follows:

$$\frac{\partial T_{g_1}}{\partial t} = \frac{1}{C_s}\left[(1-p_{sn})(SW_{net} + LW_{net} - H - LE) + p_{sn}(G_{sn} + R_{sn})\right] - \frac{1}{c_{g_1}\Delta z_1}\left(\overline{\lambda}_1 \frac{T_{g_1} - T_{g_2}}{\Delta \widetilde{z}_1} + L_f Q_{fz_1}\right) \quad (B1)$$

where T_{g_2} (K) is the soil temperature of the second layer, Δz_1 (m) the thickness of the first layer, $\Delta\widetilde{z}_1$ (m) the thickness between the first and second consecutive layer midpoints or nodes, SW_{net} (W/m^2) and LW_{net} (W/m^2) the snow-free shortwave and longwave net radiation, H (W/m^2) the snow-free sensible heat flux, LE (W/m^2) the snow-free latent heat flux, G_{sn} (W/m^2) the heat flux between the snowpack and the soil, R_{sn} (W/m^2) the net radiations not absorbed by the snowpack, $\overline{\lambda}_1$ (W $\cdot$ m^{-1} $\cdot$ K^{-1}) the weighted harmonic mean of the soil thermal conductivity at the interface between the first and second soil nodes, c_{g_1} (J $\cdot$ m^{-3} $\cdot$ K^{-1}) the soil heat capacity in the first layer, and C_s (J $\cdot$ m^{-2} $\cdot$ K^{-1}) the composite soil-vegetation-flood heat capacity at the surface. Snow-free SW_{net} and LW_{net} uses also composite albedo and emissivity computed as follows using vegetation, snow, and effective flood fractions:

$$\alpha_g = \frac{\left(1 - p_{f_{eff}} - p_{sn}\right)\left[\left(1 - f_{veg}\right)\alpha_{vegfree} + f_{veg}\alpha_{veg}\right] + p_{f_{eff}}\alpha_f}{1 - p_{sn}} \quad (B2a)$$

$$\varepsilon_g = \frac{\left(1 - p_{f_{eff}} - p_{sn}\right)\left[\left(1 - f_{veg}\right)\varepsilon_{vegfree} + f_{veg}\varepsilon_{veg}\right] + p_{f_{eff}}\varepsilon_f}{1 - p_{sn}} \quad (B2b)$$

where α_{sn} is the snow albedo, α_{veg} and $\alpha_{vegfree}$ the vegetation and vegetation-free albedo respectively computed via the MODIS product (e.g., section 2.3), ε_{sn} is the snow emissivity set to 0.99, and ε_{veg} and $\varepsilon_{vegfree}$ the vegetation and vegetation-free emissivity set to 0.97 and 0.94, respectively.

The soil-vegetation-flood composite heat capacity over the snow-free fraction of the grid cell is computed as follows using grid cell vegetation and effective flood (equation 9) fractions:

$$C_s = \left(1 - f_{veg}\right)\left(1 - p_{f_g}\right)\Delta z_1 c_{g_1} + f_{veg}\left(1 - p_{f_v}\right)C_v + p_{f_{eff}}C_f \quad (B3)$$

where C_v (J $\cdot$ m^{-2} $\cdot$ K^{-1}) is the total heat capacity of the vegetation, and C_f (J $\cdot$ m^{-2} $\cdot$ K^{-1}) is the heat capacity of the flood. C_v is defined as the sum of the specific vegetation heat capacity with the heat capacity of the water retained by the foliage:

$$C_v = c_v + c_w W_r \quad (B4)$$

where c_v (J $\cdot$ m^{-2} $\cdot$ K^{-1}) is the vegetation-specific heat capacity set by default to 10,000 and 20,000 J $\cdot$ m^{-2} $\cdot$ K^{-1} for low and tall vegetation respectively, W_r (m) the amount of water stored on the canopy, and $c_w = 4{,}218$ J $\cdot$ kg^{-1} $\cdot$ K^{-1} the heat capacity of water. C_f depends on water thermal properties and is approximated via the method of Deardorff (1978) as follows:

$$C_f = \sqrt{\frac{\lambda_w \rho_w c_w \tau_{day}}{4\pi}} \quad \left(\approx 128600 \text{ J.m}^{-2}.\text{K}^{-1}\right) \quad (B5)$$

where $\lambda_w = 0.57$ W $\cdot$ m^{-1} $\cdot$ K^{-1} is the water thermal conductivity.

Appendix C: ISBA Ice Sheet Runoff

To limit unrealistic snow accumulation over continental glaciers, a simple ice sheet runoff is parametrized as the flow of snow in excess compared to a snow mass equivalent to a significant height of aged snow. So a

virtual excess-snow reservoir, W_{ex} (kg/m^2), is solved at each model time step in which an ice sheet runoff can be diagnosed as follows via a time relaxation, τ_{yr} (s), of 1 year:

$$\frac{\partial W_{ex}}{\partial t} = \mathrm{H}R_{sn} - \frac{W_{ex}}{\tau_{yr}} \quad \text{with} \quad H = \begin{cases} 0 & \forall W_{sn} \leq h_{ice}\rho_{snmax} \\ 1 & \forall W_{sn} > h_{ice}\rho_{snmax} \end{cases} \tag{C1}$$

where H is the Heaviside function, W_{sn} (kg/m^2) the total snow water equivalent, h_{ice} (m) the snow height threshold set by default to 30 m of aged snow, and ρ_{snmax} (kg/m^3) the maximum density of snow. The ice sheet runoff is thus given by

$$Q_{ice} = \frac{W_{ex}}{\tau_{yr}} \tag{C2}$$

This could be crudely considered as the amount of water that would ultimately return to the ocean from iceberg discharge. Note that in the CNRM-CM6 climate model, h_{ice} is set to 1,000 m in order to better approximate ice sheet thermodynamics.

References

Adams, W. A. (1973). The effect of organic matter on the bulk and true densities of some uncultivated podzolic soils. *Journal of Soil Science*, *24*(1), 10–17. https://doi.org/10.1111/j.1365-2389.1973.tb00737.x

Alfieri, L., Bisselink, B., Dottori, F., Naumann, G., de Roo, A., Salamon, P., et al. (2017). Global projections of river flood risk in a warmer world. *Earth's Future*, *5*, 171–182. https://doi.org/10.1002/2016EF000485

Alkama, R., Decharme, B., Douville, H., Becker, M., Cazenave, A., Sheffield, J., et al. (2010). Global evaluation of the ISBA-TRIP continental hydrological system. Part I: Comparison to GRACE terrestrial water storage estimates and in situ river discharges. *Journal of Hydrometeorology*, *11*(3), 583–600. https://doi.org/10.1175/2010JHM1211.1

Alkama, R., Decharme, B., Douville, H., & Ribes, A. (2011). Trends in global and basin-scale runoff over the late twentieth century: Methodological issues and sources of uncertainty. *Journal of Climate*, *24*(12), 3000–3014. https://doi.org/10.1175/2010JCLI3921.1

Antico, A., Aguiar, R. O., & Amsler, M. L. (2018). Hydrometric data rescue in the Paraná River Basin. *Water Resources Research*, *54*, 1368–1381. https://doi.org/10.1002/2017WR020897

Arora, V. K., & Boer, G. J. (1999). A variable velocity flow routing algorithm for GCMs. *Journal of Geophysical Research*, *104*(D24), 30,965–30,979. https://doi.org/10.1029/1999JD900905

Arora, V. K., Chiew, F. H. S., & Grayson, R. B. (1999). A river flow routing scheme for general circulation models. *Journal of Geophysical Research*, *104*(D12), 14,347–14,357. https://doi.org/10.1029/1999JD900200

Balsamo, G., Albergel, C., Beljaars, A., Boussetta, S., Brun, E., Cloke, H., et al. (2015). ERA-Interim/Land: A global land surface reanalysis data set. *Hydrology and Earth System Sciences*, *19*(1), 389–407. https://doi.org/10.5194/hess-19-389-2015

Balsamo, G., Beljaars, A., Scipal, K., Viterbo, P., van den Hurk, B., Hirschi, M., & Betts, A. K. (2009). A revised hydrology for the ECMWF model: Verification from field site to terrestrial water storage and impact in the integrated forecast system. *Journal of Hydrometeorology*, *10*(3), 623–643. https://doi.org/10.1175/2008JHM1068.1

Beck, H. E., Vergopolan, N., Pan, M., Levizzani, V., van Dijk, A. I. J. M., Weedon, G. P., et al. (2017). Global-scale evaluation of 22 precipitation datasets using gauge observations and hydrological modeling. *Hydrology and Earth System Sciences*, *21*(12), 6201–6217. https://doi.org/10.5194/hess-21-6201-2017

Beven, K. J., & Kirkby, M. J. (1979). A physically based, variable contributing area model of basin hydrology. *Hydrological Sciences Bulletin*, *24*(1), 43–69. https://doi.org/10.1080/02626667909491834

Boelter, D. H. (1969). Physical properties of peats as related to degree of decomposition. *Soil Science Society of America Journal*, *33*(4), 606–609. https://doi.org/10.2136/sssaj1969.03615995003300040033x

Bonan, G. B., & Shugart, H. H. (1989). Environmental Factors and Ecological Processes in Boreal Forests. *Annual Review of Ecology and Systematics*, *20*(1), 1–28. https://doi.org/10.1146/annurev.es.20.110189.000245

Boone, A., Calvet, J.-C., & Noilhan, J. (1999). Inclusion of a third soil layer in aland surface scheme using the force–restore method. *Journal of Applied Meteorology*, *38*(11), 1611–1630. https://doi.org/10.1175/1520-0450(1999)038<1611:IOATSL>2.0.CO;2

Boone, A., & Etchevers, P. (2001). An intercomparison of three snow schemes of varying complexity coupled to the same land surface model: Local-scale evaluation at an Alpine site. *Journal of Hydrometeorology*, *2*(4), 374–394. https://doi.org/10.1175/1525-7541(2001)002<0374:AIOTSS>2.0.CO;2

Boone, A., Masson, V., Meyers, T., & Noilhan, J. (2000). The influence of the inclusion of soil freezing on simulations by a soil–vegetation–atmosphere transfer scheme. *Journal of Applied Meteorology*, *39*(9), 1544–1569. https://doi.org/10.1175/1520-0450(2000)039<1544:TIOTIO>2.0.CO;2

Boone, A., Samuelsson, P., Gollvik, S., Napoly, A., Jarlan, L., Brun, E., & Decharme, B. (2017). The interactions between soil-biosphere-atmosphere landsurface model with a multi-energy balance (ISBA-MEB) option in SURFEXv8-Part 1:Model description. *Geoscientific Model Development*, *10*(2). https://doi.org/10.5194/gmd-10-843-2017

Braud, I., Noilhan, J., Bessemoulin, P., Mascart, P., Haverkamp, R., & Vauclin, M. (1993). Bare-ground surface heat and water exchanges under dry conditions: Observations and parameterization. *Boundary-Layer Meteorology*, *66*(1-2), 173–200. https://doi.org/10.1007/BF00705465

Brodzik, M. J., &Armstrong, R. (2013). Northern Hemisphere EASE-Grid 2.0 weekly snow cover and sea ice extent, version 4. Boulder, Colorado USA. NASA National Snow and IceData Center Distributed Active Archive Center. https://doi.org/10.5067/P7O0HGJLYUQU

Brooks, R.-H., & Corey, A.-T. (1966). Properties of porous media affecting fluid flow. *Journal of the Irrigation and Drainage Division*, *92*(2), 61–90.

Brown, J., Ferrians, O., Heginbottom, J. A., &Melnikov, E. (2002). Circum-Arctic map of permafrost and ground-ice conditions, Version 2. Retrieved January 11, 2017, from http://nsidc.org/data/ggd318

Brown, J., Hinkel, K. M., & Nelson, F. E. (2000). The Circumpolar Active Layer Monitoring (CALM) program: Research designs and initial results 1. *Polar Geography*, *24*(3), 165–258.

Brun, E., Vionnet, V., Boone, A., Decharme, B., Peings, Y., Valette, R., et al. (2013). Simulation of northern Eurasian local snow depth, mass, and density using a detailed snowpack model and meteorological reanalyses. *Journal of Hydrometeorology*, *14*(1), 203–219. https://doi.org/10.1175/JHM-D-12-012.1

Brutel-Vuilmet, C., Ménégoz, M., & Krinner, G. (2013). An analysis of present and future seasonal Northern Hemisphere land snow cover simulated by CMIP5 coupled climate models. *The Cryosphere*, *7*(1), 67–80. https://doi.org/10.5194/tc-7-67-2013

Calvet, J.-C., Noilhan, J., Roujean, J. L., Bessemoulin, P., Cabelguenne, M., Olioso, A., & Wigneron, J. P. (1998). An interactive vegetation SVAT model tested against data from six contrasting sites. *Agricultural and Forest Meteorology*, *92*(2), 73–95. https://doi.org/10.1016/S0168-1923(98)00091-4

Canadell, J., Jackson, R. B., Ehleringer, J. B., Mooney, H. A., Sala, O. E., & Schulze, E. D. (1996). Maximum rooting depth of vegetation types at the global scale. *Oecologia*, *108*(4), 583–595. https://doi.org/10.1007/BF00329030

Canal, N., Calvet, J.-C., Decharme, B., Carrer, D., Lafont, S., & Pigeon, G. (2014). Evaluation of root water uptake in the ISBA-A-gs land surface model using agricultural yield statistics over France. *Hydrology and Earth System Sciences*, *18*(12), 4979–4999. https://doi.org/10.5194/hess-18-4979-2014

Carrer, D., Meurey, C., Ceamanos, X., Roujean, J. L., Calvet, J.-C., & Liu, S. (2014). Dynamic mapping of snow-free vegetation and bare soil albedos at global 1km scale from 10-year analysis of MODIS satellite products. *Remote Sensing of Environment*, *140*, 420–432. https://doi.org/10.1016/j.rse.2013.08.041

Casse, C., Gosset, M., Peugeot, C., Pedinotti, V., Boone, A., Tanimoun, B. A., & Decharme, B. (2015). Potential of satellite rainfall products to predict Niger River flood events in Niamey. *Atmospheric Research*, *163*, 162–176. https://doi.org/10.1016/j.atmosres.2015.01.010

Cazenave, A., Dieng, H.-B., Meyssignac, B., Von Schuckmann, K., Decharme, B., & Berthier, E. (2014). The rate of sea-level rise. *Nature Climate Change*, *4*(5), 358–361. https://doi.org/10.1038/nclimate2159

Chadburn, S. E., Burke, E. J., Cox, P. M., Friedlingstein, P., Hugelius, G., & Westermann, S. (2017). An observation-based constraint on permafrost loss as a function of global warming. *Nature Climate Change*, *7*, 340–344. https://doi.org/10.1038/nclimate3262

Clapp, R. B., & Hornberger, G. M. (1978). Empirical equations for some soil hydraulic properties. *Water Resources Research*, *14*(4), 601–604. https://doi.org/10.1029/WR014i004p00601

Cogley, J. G. (2003). GGHYDRO—Global hydrographic data, release 2.3.1 Trent Technical Note 2003-1. Retrieved from http://people.trentu.ca/~gcogley/glaciology/gghrls231.pdf

Cosby, B. J., Hornberger, G. M., Clapp, R. B., & Ginn, T. R. (1984). A statistical exploration of the relationships of soil moisture characteristics to the physical properties of soils. *Water Resources Research*, *20*(6), 682–690. https://doi.org/10.1029/WR020i006p00682

Dalin, C., Wada, Y., Kastner, T., & Puma, M. J. (2017). Groundwater depletion embedded in international food trade. *Nature*, *543*, 700–704. https://doi.org/10.1038/nature21403

Danielson, J.-J., &Gesch, D.-B. (2011). Global multi-resolution terrain elevation data 2010 (GMTED2010). U.S. Geological Survey Open-File Report 2011–1073, 26. Retrieved from https://pubs.usgs.gov/of/2011/1073/pdf/of2011-1073.pdf

Dankers, R., Burke, E. J., & Price, J. (2011). Simulation of permafrost and seasonal thaw depth in the JULES land surface scheme. *The Cryosphere*, *5*(3), 773–790. https://doi.org/10.5194/tc-5-773-2011

Deardorff, J. W. (1977). A parameterization of ground-surface moisture content for use in atmospheric prediction models. *Journal of Applied Meteorology*, *16*(11), 1182–1185. https://doi.org/10.1175/1520-0450(1977)016<1182:APOGSM>2.0.CO;2

Deardorff, J. W. (1978). Efficient prediction of ground surface temperature and moisture, with inclusion of a layer of vegetation. *Journal of Geophysical Research*, *83*(C4), 1889–1903. https://doi.org/10.1029/JC083iC04p01889

Decharme, B. (2007). Influence of runoff parameterization on continental hydrology: Comparison between the Noah and the ISBA land surface models. *Journal of Geophysical Research*, *112*, D19108. https://doi.org/10.1029/2007JD008463

Decharme, B., Alkama, R., Douville, H., Becker, M., & Cazenave, A. (2010). Global evaluation of the ISBA-TRIP continental hydrological system. Part II: Uncertainties in river routing simulation related to flow velocity and groundwater storage. *Journal of Hydrometeorology*, *11*(3), 601–617. https://doi.org/10.1175/2010JHM1212.1

Decharme, B., Alkama, R., Papa, F., Faroux, S., Douville, H., & Prigent, C. (2012). Global off-line evaluation of the ISBA-TRIP flood model. *Climate Dynamics*, *38*(7–8), 1389–1412. https://doi.org/10.1007/s00382-011-1054-9

Decharme, B., Boone, A., Delire, C., & Noilhan, J. (2011). Local evaluation of the interaction between Soil Biosphere Atmosphere soil multilayer diffusion scheme using four pedotransfer functions. *Journal of Geophysical Research*, *116*, D20126. https://doi.org/10.1029/2011JD016002

Decharme, B., Brun, E., Boone, A., Delire, C., Le Moigne, P., & Morin, S. (2016). Impacts of snow and organic soils parameterization on northern Eurasian soil temperature profiles simulated by the ISBA land surface model. *The Cryosphere*, *10*(2), 853–877. https://doi.org/10.5194/tc-10-853-2016

Decharme, B., & Douville, H. (2006a). Introduction of a sub-grid hydrology in the ISBA land surface model. *Climate Dynamics*, *26*(1), 65–78. https://doi.org/10.1007/s00382-005-0059-7

Decharme, B., & Douville, H. (2006b). Uncertainties in the GSWP-2 precipitation forcing and their impacts on regional and global hydrological simulations. *Climate Dynamics*, *27*(7–8), 695–713. https://doi.org/10.1007/s00382-006-0160-6

Decharme, B., & Douville, H. (2007). Global validation of the ISBA sub-grid hydrology. *Climate Dynamics*, *29*(1), 21–37. https://doi.org/10.1007/s00382-006-0216-7

Decharme, B., Douville, H., Boone, A., Habets, F., & Noilhan, J. (2006). Impact of an exponential profile of saturated hydraulic conductivity within the ISBA LSM: Simulations over the Rhône Basin. *Journal of Hydrometeorology*, *7*(1), 61–80. https://doi.org/10.1175/JHM469.1

Decharme, B., Douville, H., Prigent, C., Papa, F., & Aires, F. (2008). A new river flooding scheme for global climate applications: Off-line evaluation over South America. *Journal of Geophysical Research*, *113*, D11110. https://doi.org/10.1029/2007JD009376

Decharme, B., Martin, E., & Faroux, S. (2013). Reconciling soil thermal and hydrological lower boundary conditions in land surface models. *Journal of Geophysical Research: Atmospheres*, *118*, 7819–7834. https://doi.org/10.1002/jgrd.50631

Derksen, C., & Brown, R. (2012). Spring snow cover extent reductions in the 2008-2012 period exceeding climate model projections. *Geophysical Research Letters*, *39*, L19504. https://doi.org/10.1029/2012GL053387

Douville, H. (2003). Assessing the influence of soil moisture on seasonal climate variability with AGCMs. *Journal of Hydrometeorology*, *4*(6), 1044–1066. https://doi.org/10.1175/1525-7541(2003)004<1044:ATIOSM>2.0.CO;2

Douville, H., Colin, J., Krug, E., Cattiaux, J., & Thao, S. (2016). Midlatitude daily summer temperatures reshaped by soil moisture under climate change. *Geophysical Research Letters*, *43*, 812–818. https://doi.org/10.1002/2015GL066222

Douville, H., Ribes, A., Decharme, B., Alkama, R., & Sheffield, J. (2013). Anthropogenic influence on multidecadal changes in reconstructed global evapotranspiration. *Nature Climate Change*, *3*(1), 59–62. https://doi.org/10.1038/nclimate1632

Douville, H., Royer, J. F., & Mahfouf, J.-F. (1995). A new snow parameterization for the Météo-France climate model: Part I. Validation in stand-alone experiments. *Climate Dynamics*, *12*(1), 21–35. https://doi.org/10.1007/BF00208760

Ducharne, A., Golaz, C., Leblois, E., Laval, K., Polcher, J., Ledoux, E., & De Marsily, G. (2003). Development of a high resolution runoff routing model, calibration and application to assess runoff from the LMD GCM. *Journal of Hydrology*, *280*(1–4), 207–228. https://doi.org/10.1016/S0022-1694(03)00230-0

Durand, F., Papa, F., Rahman, A., & Bala, S. K. (2011). Impact of Ganges-Brahmaputra interannual discharge variations on Bay of Bengal salinity and temperature during 1992-1999 period. *Journal of Earth System Science*, *120*(5), 859–872. https://doi.org/10.1007/s12040-011-0118-x

Dürr, H. H., Meybeck, M., & Dürr, S. H. (2005). Lithologic composition of the Earth's continental surfaces derived from a new digital map emphasizing riverine material transfer. *Global Biogeochemical Cycles*, *19*, GB4S10. https://doi.org/10.1029/2005GB002515

Ekici, A., Beer, C., Hagemann, S., Boike, J., Langer, M., & Hauck, C. (2014). Simulating high-latitude permafrost regions by the JSBACH terrestrial ecosystem model. *Geoscientific Model Development*, *7*(2), 631–647. https://doi.org/10.5194/gmd-7-631-2014

Emery, C. M., Biancamaria, S., Boone, A., Garambois, P.-A., Ricci, S., Rochoux, M. C., & Decharme, B. (2016). Temporal variance-based sensitivity analysis of the river-routing component of the large-scale hydrological model ISBA-TRIP: Application on the Amazon Basin. *Journal of Hydrometeorology*, *17*(12), 3007–3027. https://doi.org/10.1175/JHM-D-16-0050.1

Eyring, V., Bony, S., Meehl, G. A., Senior, C. A., Stevens, B., Stouffer, R. J., & Taylor, K. E. (2016). Overview of the Coupled Model Intercomparison Project Phase 6 (CMIP6) experimental design and organization. *Geoscientific Model Development*, *9*(5), 1937–1958. https://doi.org/10.5194/gmd-9-1937-2016

Fan, Y. (2015). Groundwater in the Earth's critical zone: Relevance to large-scale patterns and processes. *Water Resources Research*, *51*, 3052–3069. https://doi.org/10.1002/2015WR017037

Fan, Y., Li, H., & Miguez-Macho, G. (2013). Global patterns of groundwater table depth. *Science*, *339*(6122), 940–943. https://doi.org/10.1126/science.1229881

FAO/IIASA/ISRIC/ISSCAS/JRC. (2012). Harmonized World Soil Database (version 1.2). FAO, Rome, Italy and IIASA, Laxenburg, Austria.

Farouki, O. T. (1986). Thermal properties of soils. Series on Rock and Soil Mechanics, 11(Trans Tech), 136 pp.

Faroux, S., Kaptué Tchuenté, A. T., Roujean, J.-L., Masson, V., Martin, E., & Le Moigne, P. (2013). ECOCLIMAP-II/Europe: A twofold database of ecosystems and surface parameters at 1 km resolution based on satellite information for use in land surface, meteorological and climate models. *Geoscientific Model Development*, *6*(2), 563–582. https://doi.org/10.5194/gmd-6-563-2013

Fuchs, M., Campbell, G. S., & Papendick, R. I. (1978). An analysis of sensible and latent heat flow in a partially frozen unsaturated soil. *Soil Science Society of America Journal*, *42*(3), 379. https://doi.org/10.2136/sssaj1978.03615995004200030001x

Garrigues, S., A. Boone, Decharme, B., Olioso, A., Albergel, C., Calvet, J. C., et al. (2018). Impacts of the soil water transfer parameterization on the simulation of evapotranspiration over a 14-year Mediterranean crop succession. *Journal of Hydrometeorology*, *19*(1), 3–25. https://doi.org/10.1175/JHM-D-17-0058.1

Gelati, E., Decharme, B., Calvet, J.-C., Minvielle, M., Polcher, J., Fairbairn, D., & Weedon, G. P. (2018). Hydrological assessment of atmospheric forcing uncertainty in the Euro-Mediterranean area using a land surface model. *Hydrology and Earth System Sciences*, *22*(4), 2091–2115. https://doi.org/10.5194/hess-22-2091-2018

Gouttevin, I., Krinner, G., Ciais, P., Polcher, J., & Legout, C. (2012). Multi-scale validation of a new soil freezing scheme for a land-surface model with physically-based hydrology. *The Cryosphere*, *6*(2), 407–430. https://doi.org/10.5194/tc-6-407-2012

Green, W. H., & Ampt, G. A. (1911). Studies on soil phyics. *The Journal of Agricultural Science*, *4*(01), 1–24. https://doi.org/10.1017/S0021859600001441

Guimberteau, M., Zhu, D., Maignan, F., Huang, Y., Yue, C., Dantec-Nédélec, S., et al. (2018). ORCHIDEE-MICT (v8.4.1), a land surface model for the high latitudes: Model description and validation. *Geoscientific Model Development*, *11*(1), 121–163. https://doi.org/10.5194/gmd-11-121-2018

Guo, D., Wang, H., & Wang, A. (2017). Sensitivity of historical simulation of the permafrost to different atmospheric forcing data sets from 1979 to 2009. *Journal of Geophysical Research: Atmospheres*, *122*, 12,269–12,284. https://doi.org/10.1002/2017JD027477

Habets, F., Boone, A., Champeaux, J. L., Etchevers, P., Franchistéguy, L., Leblois, E., et al. (2008). The SAFRAN-ISBA-MODCOU hydrometeorological model applied over France. *Journal of Geophysical Research*, *113*, D06113. https://doi.org/10.1029/2007JD008548

Holland, M. M., & Bitz, C. M. (2003). Polar amplification of climate change in coupled models. *Climate Dynamics*, *21*(3–4), 221–232. https://doi.org/10.1007/s00382-003-0332-6

Huang, B., & Mehta, V. M. (2010). Influences of freshwater from major rivers on global ocean circulation and temperatures. *Advances in Atmospheric Sciences*, *27*(3), 455–468. https://doi.org/10.1007/s00376-009-9022-6

Jackson, R. B., Canadell, J., Ehleringer, J. R., Mooney, H. A., Sala, O. E., & Schulze, E. D. (1996). A global analysis of root distributions for terrestrial biomes. *Oecologia*, *108*(3), 389–411. https://doi.org/10.1007/BF00333714

Jacob, C. M. J. (1994). *Direct impact of atmospheric CO enrichment on regional transpiration*. Wageningen, The Netherlands. Retrieved from: Agricultural University. https://library.wur.nl/WebQuery/wda/599197

Jahfer, S., Vinayachandran, P. N., & Nanjundiah, R. S. (2017). Long-term impact of Amazon river runoff on Northern Hemispheric climate. *Scientific Reports*, *7*(1), 10989. https://doi.org/10.1038/s41598-017-10750-y

Jarvis, P. G. (1976). The interpretation of the variations in leaf water potential and stomatal conductance found in canopies in the field. *Philosophical Transactions of the Royal Society, B: Biological Sciences*, *273*(927), 593–610. https://doi.org/10.1098/rstb.1976.0035

Jia, Y., Wang, H., Zhou, Z., Qiu, Y., Luo, X., Wang, J., et al. (2006). Development of the WEP-L distributed hydrological model and dynamic assessment of water resources in the Yellow River basin. *Journal of Hydrology*, *331*(3–4), 606–629. https://doi.org/10.1016/J.JHYDROL.2006.06.006

Joetzjer, E., Delire, C., Douville, H., Ciais, P., Decharme, B., Carrer, D., et al. (2015). Improving the ISBA(CC) land surface model simulation of water and carbon fluxes and stocks over the Amazon forest. *Geoscientific Model Development*, *8*(6), 1709–1727. https://doi.org/10.5194/gmd-8-1709-2015

Johnsson, H., & Lundin, L.-C. (1991). Surface runoff and soil water percolation as affected by snow and soil frost. *Journal of Hydrology*, *122*(1–4), 141–159. https://doi.org/10.1016/0022-1694(91)90177-J

Jung, M., Reichstein, M., Ciais, P., Seneviratne, S. I., Sheffield, J., Goulden, M. L., et al. (2010). Recent decline in the global land evapotranspiration trend due to limited moisture supply. *Nature*, *467*(7318), 951–954. https://doi.org/10.1038/nature09396

Knoblauch, C., Beer, C., Liebner, S., Grigoriev, M. N., & Pfeiffer, E. M. (2018). Methane production as key to the greenhouse gas budget of thawing permafrost. *Nature Climate Change*, *8*, 309–312. https://doi.org/10.1038/s41558-018-0095-z

Koch, J. C., Ewing, S. A., Striegl, R., & McKnight, D. M. (2013). Rapid runoff via shallow throughflow and deeper preferential flow in a boreal catchment underlain by frozen silt (Alaska, USA). *Hydrogeology Journal*, *21*(1), 93–106. https://doi.org/10.1007/s10040-012-0934-3

Koren, V., Schaake, J., Mitchell, K., Duan, Q.-Y., Chen, F., & Baker, J. M. (1999). A parameterization of snowpack and frozen ground intended for NCEP weather and climate models. *Journal of Geophysical Research*, *104*(D16), 19,569–19,585. https://doi.org/10.1029/1999JD900232

Koster, R. D., Dirmeyer, P. A., Guo, Z., Bonan, G., Chan, E., Cox, P., et al., & GLACE Team (2004). Regions of strong coupling between soil moisture and precipitation. *Science (New York, N.Y.)*, *305*(5687), 1138–1140. https://doi.org/10.1126/science.1100217

Koster, R. D., Mahanama, S. P. P., Yamada, T. J., Balsamo, G., Berg, A. A., Boisserie, M., et al. (2011). The second phase of the global land–atmosphere coupling experiment: Soil moisture contributions to subseasonal forecast skill. *Journal of Hydrometeorology*, *12*(5), 805–822. https://doi.org/10.1175/2011JHM1365.1

Koven, C., Friedlingstein, P., Ciais, P., Khvorostyanov, D., Krinner, G., & Tarnocai, C. (2009). On the formation of high-latitude soil carbon stocks: Effects of cryoturbation and insulation by organic matter in a land surface model. *Geophysical Research Letters*, *36*, L21501. https://doi.org/10.1029/2009GL040150

Krinner, G. (2003). Impact of lakes and wetlands on boreal climate. *Journal of Geophysical Research*, *108*(D16), 4520. https://doi.org/10.1029/2002JD002597

Lafaysse, M., Hingray, B., Etchevers, P., Martin, E., & Obled, C. (2011). Influence of spatial discretization, underground water storage and glacier melt on a physically-based hydrological model of the Upper Durance River basin. *Journal of Hydrology*, *403*(1), 116–129. https://doi.org/10.1016/j.jhydrol.2011.03.046

Landerer, F. W., & Swenson, S. C. (2012). Accuracy of scaled GRACE terrestrial water storage estimates. *Water Resources Research*, *48*, W04531. https://doi.org/10.1029/2011WR011453

Lawrence, D. M., & Slater, A. G. (2008). Incorporating organic soil into a global climate model. *Climate Dynamics*, *30*(2-3), 145–160. https://doi.org/10.1007/s00382-007-0278-1

Lehner, B., & Döll, P. (2004). Development and validation of a global database of lakes, reservoirs and wetlands. *Journal of Hydrology*, *296*(1-4), 1–22. https://doi.org/10.1016/j.jhydrol.2004.03.028

Letts, M. G., Comer, N. T., Roulet, N. T., Skarupa, M. R., & Verseghy, D. L. (2000). Parametrization of peatland hydraulic properties for the Canadian land surface scheme. *Atmosphere-Ocean*, *38*(1), 141–160. https://doi.org/10.1080/07055900.2000.9649643

Llovel, W., Becker, M., Cazenave, A., Jevrejeva, S., Alkama, R., Decharme, B., et al. (2011). Terrestrial waters and sea level variations on interannual time scale. *Global and Planetary Change*, *75*(1–2), 76–82. https://doi.org/10.1016/j.gloplacha.2010.10.008

Lohmann, D., Raschke, E., Nijssen, B., & Lettenmaier, D. P. (1998). Hydrologie à l'échelle régionale: I. Formulation du modèle VIC-2L couplé à un modèle du transfert de l'eau. *Hydrological Sciences Journal*, *43*(1), 131–141. https://doi.org/10.1080/02626669809492107

Lucas-Picher, P., Arora, V. K., Caya, D., & Laprise, R. (2003). Implementation of a large-scale variable velocity river flow routing algorithm in the Canadian Regional Climate Model (CRCM). *Atmosphere-Ocean*, *41*(2), 139–153. https://doi.org/10.3137/ao.410203

Lundquist, J. D., Cayan, D. R., Dettinger, M. D., Lundquist, J. D., Cayan, D. R., & Dettinger, M. D. (2004). Spring onset in the Sierra Nevada: When is snowmelt independent of elevation? *Journal of Hydrometeorology*, *5*(2), 327–342. https://doi.org/10.1175/1525-7541(2004)005<0327:SOITSN>2.0.CO;2

Mahfouf, J.-F., Manzi, A. O., Noilhan, J., Giordani, H., & Deque, M. (1995). The land surface scheme ISBA within the Meteo-France climate model ARPEGE. Part I: Implementation and preliminary results. *Journal of Climate*, *8*(8), 2039–2057. https://doi.org/10.1175/1520-0442(1995)008<2039:TLSSIW>2.0.CO;2

Mahfouf, J.-F., & Noilhan, J. (1991). Comparative study of various formulations of evaporation from bare soil using in situ data. *Journal of Applied Meteorology*, *9*, 351–362.

Mahfouf, J.-F., & Noilhan, J. (1996). Inclusion of gravitational drainage in a land surface scheme based on the force-restore method. *Journal of Applied Meteorology*, *35*, 987–992.

Manabe, S. (1969). Climate and the ocean circulation. *Monthly Weather Review*, *97*(11), 739–774. https://doi.org/10.1175/1520-0493(1969)097<0739:CATOC>2.3.CO;2

Martens, B., Miralles, D. G., Lievens, H., van der Schalie, R., de Jeu, R. A. M., Fernández-Prieto, D., et al. (2017). GLEAM v3: Satellite-based land evaporation and root-zone soil moisture. *Geoscientific Model Development*, *10*(5), 1903–1925. https://doi.org/10.5194/gmd-10-1903-2017

Masson, V., Champeaux, J. L., Chauvin, F., Meriguet, C., & Lacaze, R. (2003). A global database of land surface parameters at 1-km resolution in meteorological and climate models. *Journal of Climate*, *16*(9), 1261–1282. https://doi.org/10.1175/1520-0442-16.9.1261

Masson, V., le Moigne, P., Martin, E., Faroux, S., Alias, A., Alkama, R., et al. (2013). The SURFEXv7.2 land and ocean surface platform for coupled or offline simulation of earth surface variables and fluxes. *Geoscientific Model Development*, *6*(4), 929–960. https://doi.org/10.5194/gmd-6-929-2013

Maxwell, R. M., Chow, F. K., & Kollet, S. J. (2007). The groundwater-land-surface-atmosphere connection: Soil moisture effects on the atmospheric boundary layer in fully-coupled simulations. *Advances in Water Resources*, *30*(12), 2447–2466. https://doi.org/10.1016/j.advwatres.2007.05.018

Maxwell, R. M., Lundquist, J. K., Mirocha, J. D., Smith, S. G., Woodward, C. S., & Tompson, A. F. B. (2011). Development of a coupled groundwater–atmosphere model. *Monthly Weather Review*, *139*(1), 96–116. https://doi.org/10.1175/2010MWR3392.1

McGuire, A. D., Koven, C., Lawrence, D. M., Clein, J. S., Xia, J., Beer, C., et al. (2016). Variability in the sensitivity among model simulations of permafrost and carbon dynamics in the permafrost region between 1960 and 2009. *Global Biogeochemical Cycles*, *30*, 1015–1037. https://doi.org/10.1002/2016GB005405

Miguez-Macho, G., Fan, Y., Weaver, C. P., Walko, R., & Robock, A. (2007). Incorporating water table dynamics in climate modeling: 2. Formulation, validation, and soil moisture simulation. *Journal of Geophysical Research*, *112*, D13108. https://doi.org/10.1029/2006JD008112

Mueller, B., Hirschi, M., Jimenez, C., Ciais, P., Dirmeyer, P. A., Dolman, A. J., et al. (2013). Benchmark products for land evapotranspiration: LandFlux-EVAL multi-data set synthesis. *Hydrology and Earth System Sciences*, *17*, 3707–3720. https://doi.org/10.5194/hess-17-3707-2013

Nash, J. E., & Sutcliffe, J. V. (1970). River flow forecasting through conceptual models. Part I—A discussion of principles. *Journal of Hydrology*, *10*(3), 282–290. https://doi.org/10.1016/0022-1694(70)90255-6

Naumann, G., Alfieri, L., Wyser, K., Mentaschi, L., Betts, R. A., Carrao, H., et al. (2018). Global Changes in Drought Conditions Under Different Levels of Warming. *Geophysical Research Letters*, *45*, 3285–3296. https://doi.org/10.1002/2017GL076521

Nijssen, B., Lettenmaier, D. P., Liang, X., Wetzel, S. W., & Wood, E. F. (1997). Streamflow simulation for continental-scale river basins. *Water Resources Research*, *33*(4), 711–724. https://doi.org/10.1029/96WR03517

Nijssen, B., Schnur, R., Lettenmaier, D. P., Nijssen, B., Schnur, R., & Lettenmaier, D. P. (2001). Global retrospective estimation of soil moisture using the variable infiltration capacity land surface model, 1980–93. *Journal of Climate*, *14*(8), 1790–1808. https://doi.org/10.1175/1520-0442(2001)014<1790:GREOSM>2.0.CO;2

Noilhan, J., & Lacarrere, P. (1995). GCM grid-scale evaporation from mesoscale modeling. *Journal of Climate*, *8*(2), 206–223. https://doi.org/10.1175/1520-0442(1995)008<0206:GGSEFM>2.0.CO;2

Noilhan, J., & Planton, S. (1989). A simple parameterization of land surface processes for meteorological models. *Monthly Weather Review*, *117*(3), 536–549. https://doi.org/10.1175/1520-0493(1989)117<0536:ASPOLS>2.0.CO;2

Oki, T., & Sud, Y. C. (1998). Design of Total Runoff Integrating Pathways (TRIP)—A global river channel network. *Earth Interactions*, *2*(1), 1–1. https://doi.org/10.1175/1087-3562(1998)002<0001:DoTRIP>2.0.CO;2

Papa, F., Prigent, C., Aires, F., Jimenez, C., Rossow, W. B., & Matthews, E. (2010). Interannual variability of surface water extent at the global scale, 1993–2004. *Journal of Geophysical Research*, *115*, D12111. https://doi.org/10.1029/2009JD012674

Paquin, J. P., & Sushama, L. (2014). On the Arctic near-surface permafrost and climate sensitivities to soil and snow model formulations in climate models. *Climate Dynamics*, *44*(1-2), 203–228. https://doi.org/10.1007/s00382-014-2185-6

Pedinotti, V., Boone, A., Decharme, B., Crétaux, J. F., Mognard, N., Panthou, G., et al. (2012). Evaluation of the ISBA-TRIP continental hydrologic system over the Niger basin using in situ and satellite derived datasets. *Hydrology and Earth System Sciences*, *16*(6), 1745–1773. https://doi.org/10.5194/hess-16-1745-2012

Peings, Y., Brun, E., Mauvais, V., & Douville, H. (2013). How stationary is the relationship between Siberian snow and Arctic Oscillation over the 20th century? *Geophysical Research Letters*, *40*, 183–188. https://doi.org/10.1029/2012GL054083

Peters-Lidard, C. D., Blackburn, E., Liang, X., & Wood, E. F. (1998). The effect of soil thermal conductivity parameterization on surface energy fluxes and temperatures. *Journal of the Atmospheric Sciences*, *55*(7), 1209–1224. https://doi.org/10.1175/1520-0469(1998)055<1209:TEOSTC>2.0.CO;2

Pitman, A. J. (2003). The evolution of, and revolution in, land surface schemes designed for climate models. *International Journal of Climatology*, *23*(5), 479–510. https://doi.org/10.1002/joc.893

Portmann, F. T., Siebert, S., & Döll, P. (2010). MIRCA2000-global monthly irrigated and rainfed crop areas around the year 2000: A new high-resolution data set for agricultural and hydrological modeling. *Global Biogeochemical Cycles*, *24*, GB1011. https://doi.org/10.1029/2008GB003435

Prigent, C., Papa, F., Aires, F., Rossow, W. B., & Matthews, E. (2007). Global inundation dynamics inferred from multiple satellite observations, 1993–2000. *Journal of Geophysical Research*, *112*, D12107. https://doi.org/10.1029/2006JD007847

Sacks, W. J., Cook, B. I., Buenning, N., Levis, S., & Helkowski, J. H. (2009). Effectsof global irrigation on the near-surface climate. *Climate Dynamics*, *33*(2-3), 159–175. https://doi.org/10.1007/s00382-008-0445-z

Saunois, M., Bousquet, P., Poulter, B., Peregon, A., Ciais, P., Canadell, J. G., et al. (2016). The global methane budget 2000-2012. *Earth System Science Data*, *8*(2), 697–751. https://doi.org/10.5194/essd-8-697-2016

Schellekens, J., Dutra, E., Martínez-de la Torre, A., Balsamo, G., van Dijk, A., Sperna Weiland, F., et al. (2017). A global water resources ensemble of hydrological models: The eartH2Observe Tier-1 dataset. *Earth System Science Data*, *9*(2), 389–413. https://doi.org/10.5194/essd-9-389-2017

Schneider, U., Becker, A., Finger, P., Meyer-Christoffer, A., Rudolf, B., &Ziese, M. (2011). GPCC full data reanalysis version 6.0 at 1.0°: Monthly land-surface precipitation from rain-gauges built on GTS-based and historic data. https://doi.org/10.5676/DWD_GPCC/FD_M_V6_100

Schneider, U., Becker, A., Finger, P., Meyer-Christoffer, A., Ziese, M., & Rudolf, B. (2014). GPCC's new land surface precipitation climatology based on quality-controlled in situ data and its role in quantifying the global water cycle. *Theoretical and Applied Climatology*, *115*(1–2), 15–40. https://doi.org/10.1007/s00704-013-0860-x

Schuur, E. A. G., McGuire, A. D., Schädel, C., Grosse, G., Harden, J. W., Hayes, D. J., et al. (2015). Climate change and the permafrost carbon feedback. *Nature*, *520*(7546), 171–179. https://doi.org/10.1038/nature14338

Seneviratne, S. I., Corti, T., Davin, E. L., Hirschi, M., Jaeger, E. B., Lehner, I., et al. (2010). Investigating soil moisture-climate interactions in a changing climate: A review. *Earth-Science Reviews*, *99*(3–4), 125–161. https://doi.org/10.1016/j.earscirev.2010.02.004

Seneviratne, S. I., Wilhelm, M., Stanelle, T., van den Hurk, B., Hagemann, S., Berg, A., et al. (2013). Impact of soil moisture-climate feedbacks on CMIP5 projections: First results from the GLACE-CMIP5 experiment. *Geophysical Research Letters*, *40*, 5212–5217. https://doi.org/10.1002/grl.50956

Sheffield, J., Goteti, G., & Wood, E. F. (2006). Development of a 50-year high-resolution global dataset of meteorological forcings for land surface modeling. *Journal of Climate*, *19*(13), 3088–3111. https://doi.org/10.1175/JCLI3790.1

Swenson, S., & Wahr, J. (2006). Post-processing removal of correlated errors in GRACE data. *Geophysical Research Letters*, *33*, L08402. https://doi.org/10.1029/2005GL025285

Swenson, S. C. (2012). GRACE monthly land water mass grids NETCDF RELEASE 5.0. Ver. 5.0. PO.DAAC, CA, USA. Dataset accessed [2018-07-01] at https://doi.org/10.5067/TELND-NC005.

Szczypta, C., Decharme, B., Carrer, D., Calvet, J. C., Lafont, S., Somot, S., et al. (2012). Impact of precipitation and land biophysical variables on the simulated discharge of European and Mediterranean rivers. *Hydrology and Earth System Sciences*, *16*(9), 3351–3370. https://doi.org/10.5194/hess-16-3351-2012

Taylor, R. G., Scanlon, B., Döll, P., Rodell, M., van Beek, R., Wada, Y., et al. (2013). Ground water and climate change. *Nature Climate Change*, *3*(4), 322–329. https://doi.org/10.1038/nclimate1744

Valcke, S., Craig, T., & Coquart, L. (2015). OASIS3-MCT user guide. OASIS3-MCT_3.0. Tech. Rep. TR/CMGC/15/38, Cerfacs, France. Retrieved from. http://www.cerfacs.fr/oa4web/oasis3-mct_3.0/oasis3mct_UserGuide.pdf

van den Hurk, B., Best, M., Dirmeyer, P., Pitman, A., Polcher, J., & Santanello, J. (2011). Acceleration of land surface model development over a decade of glass. *Bulletin of the American Meteorological Society*, *92*(12), 1593–1600. https://doi.org/10.1175/BAMS-D-11-00007.1

Vergnes, J.-P., & Decharme, B. (2012). A simple groundwater scheme in the TRIP river routing model: Global off-line evaluation against GRACE terrestrial water storage estimates and observed river discharges. *Hydrology and Earth System Sciences*, *16*(10), 3889–3908. https://doi.org/10.5194/hess-16-3889-2012

Vergnes, J.-P., Decharme, B., Alkama, R., Martin, E., Habets, F., & Douville, H. (2012). A simple groundwater scheme for hydrological and climate applications: Description and offline evaluation over France. *Journal of Hydrometeorology*, *13*(4), 1149–1171. https://doi.org/10.1175/JHM-D-11-0149.1

Vergnes, J.-P., Decharme, B., & Habets, F. (2014). Introduction of groundwater capillary rises using subgrid spatial variability of topography into the ISBA land surface model. *Journal of Geophysical Research: Atmospheres*, *119*, 11,065–11,086. https://doi.org/10.1002/2014JD021573

Vinayachandran, P. N., Jahfer, S., & Nanjundiah, R. S. (2015). Impact of river runoff into the ocean on Indian summer monsoon. *Environmental Research Letters*, *10*(5). https://doi.org/10.1088/1748-9326/10/5/054008

Viovy, N. (2018). *CRUNCEP version 7—Atmospheric forcing data for the Community Land Model*. Boulder, CO: Research Data Archive at the National Center for Atmospheric Research, Computational and Information Systems Laboratory. Retrieved from http://rda.ucar.edu/datasets/ds314.3/

Voldoire, A., Decharme, B., Pianezze, J., Lebeaupin Brossier, C., Sevault, F., Seyfried, L., et al. (2017). SURFEX v8.0 interface with OASIS3-MCT to couple atmosphere with hydrology, ocean, waves and sea-ice models, from coastal to global scales. *Geoscientific Model Development*, *10*(11), 4207–4227. https://doi.org/10.5194/gmd-10-4207-2017

Voldoire, A., Sanchez-Gomez, E., Salas y Mélia, D., Decharme, B., Cassou, C., Sénési, S., et al. (2013). The CNRM-CM5.1 global climate model: Description and basic evaluation. *Climate Dynamics*, *40*(9–10), 2091–2121. https://doi.org/10.1007/s00382-011-1259-y

Walvoord, M. A., & Kurylyk, B. L. (2016). Hydrologic impacts of thawing permafrost—A review. *Vadose Zone Journal*, *15*(6). https://doi.org/10.2136/vzj2016.01.0010

Wang, W., Rinke, A., Moore, J. C., Ji, D., Cui, X., Peng, S., et al. (2016). Evaluation of air-soil temperature relationships simulated by land surface models during winter across the permafrost region. *The Cryosphere*, *10*(4), 1721–1737. https://doi.org/10.5194/tc-10-1721-2016

Weedon, G. P., Balsamo, G., Bellouin, N., Gomes, S., Best, M. J., & Viterbo, P. (2014). Data methodology applied to ERA-Interim reanalysis data. *Water Resources Research*, *50*, 7505–7514. https://doi.org/10.1002/2014WR015638

Weedon, G. P., Gomes, S., Viterbo, P., Shuttleworth, W. J., Blyth, E., Österle, H., et al. (2011). Creation of the WATCH forcing data and its use to assess global and regional reference crop evaporation over land during the twentieth century. *Journal of Hydrometeorology*, *12*(5), 823–848. https://doi.org/10.1175/2011JHM1369.1

Woo, M. (1986). Permafrost hydrology in North America. *Atmosphere-Ocean*, *24*(3), 201–234. https://doi.org/10.1080/07055900.1986.9649248

Yamazaki, D., Kanae, S., Kim, H., & Oki, T. (2011). A physically based description of floodplain inundation dynamics in a global river routing model. *Water Resources Research*, *47*, W04501. https://doi.org/10.1029/2010WR009726

Yamazaki, D., O'Loughlin, F., Trigg, M. A., Miller, Z. F., Pavelsky, T. M., & Bates, P. D. (2014). Development of the global width database for large rivers. *Water Resources Research*, *50*, 3467–3480. https://doi.org/10.1002/2013WR014664

Zhang, Y., Pena Arancibia, J., McVicar, T., Chiew, F., Vaze, J., Zheng, H., &Wang, Y. P. (2016). Monthly global observation-driven Penman-Monteith-Leuning (PML) evapotranspiration and components. v2. Retrieved January 23, 2019, from https://doi.org/10.4225/08/5719A5C48DB85

Zhang, Y., Peña-Arancibia, J. L., McVicar, T. R., Chiew, F. H. S., Vaze, J., Liu, C., et al. (2016). Multi-decadal trends in global terrestrial evapotranspiration and its components. *Scientific Reports*, *6*(1), 19124. https://doi.org/10.1038/srep19124

Zhao, F., Veldkamp, T. I. E., Frieler, K., Schewe, J., Ostberg, S., Willner, S., et al. (2017). The critical role of the routing scheme in simulating peak river discharge in global hydrological models. *Environmental Research Letters*, *12*(7). https://doi.org/10.1088/1748-9326/aa7250

Erratum

Due to a typesetting error, several units were incorrectly given in the originally published version of the article. Additionally, µ was not defined in Equation (10), and "CNRM-ESM2" was misspelled in the final sentence on page 2. These errors have been corrected, and this may be considered the authoritative version of record.